TRANSIENT ULTRASONIC FIELDS OF EFFICIENT BROADBAND PIEZOELECTRIC TRANSDUCERS

BY

NILS SPONHEIM

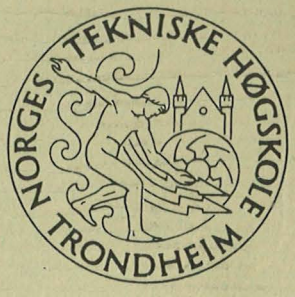

UNIVERSITETET I TRONDHEIM
NORGES TEKNISKE HØGSKOLE

INSTITUTT FOR FYSIKALSK ELEKTRONIKK

TRANSIENT ULTRASONIC FIELDS OF EFFICIENT BROADBAND PIEZOELECTRIC TRANSDUCERS

BY

NILS SPONHEIM

A thesis submitted to The Norwegian Institute of Technology in partial fulfilment of the requirements for the degree of Dr. ing.

august 1985

NTH-Trykk
Trondheim 1985

ABSTRACT

This work is devoted to the modelling and design of ultrasonic transducers for cardiographic echo imaging and doppler velocity measurements. The model for transient wave propagation is based on the spatial impulse response method. The model is used to study the focusing of planar and spherical discs, and of annular arrays. The required number of array elements and the optimum focal length are found. The transmission line model is used to model the transducers. A design with one quarter wave matching layer and a light backing is found to meet the requirements for both echo imaging and doppler velocity measurements. The theoretical results are verified experimentally. A single element and a two element transducer are made and the measured diffraction patterns are in good agreement with the theory.

ACKNOWLEDGEMENTS

I am in great debt to Kjell Arne Ingebrigtsen for his full support throughout the three years of this work. His skillful and kind guidance has meant a lot to me both professionally and personally. He has read the manuscript to this report and made suggestions for improvement.

Helge Engan has contributed by explaining measurement techniques and vibrations in bulk wave transducers.

Bjørn Angelsen has been the project leader for the mechanical scanned transducer project.

Andreas Tonning has been the supervisor for my Dr.ing. degree.

Helge Løkås, Stein Dørum, Rolf Skjevik and Kolbjørn Lindgjerdet have helped with the transducer fabrication.

Barbara Reitan and Ann-Maj Helgetun have done the typing and corrected many language errors.

Inger Reistad Rygh has prepared the drawings.

The work has been financed by grants from the Norwegian Institute of Technology (NTH) and from Vingmed A.S. The Norwegian Institute of Technology Foundation has also supported the work.

TABLE OF CONTENTS PAGE

ABSTRACT I
ACKNOWLEDGEMENTS II
1. INTRODUCTION 1
2. THEORY OF TRANSIENT FIELDS 4
2.1. The spatial impulse response method 4
2.2. Dispersion and losses 6
2.3. The echo response 12
3. TRANSDUCER MODELLING AND CALCULATIONS 18
3.1. The calculation model 18
3.2. Transducer losses 26
3.3. Increase of bandwidth 30
4. CALCULATIONS OF TRANSIENT DIFFRACTION PATTERNS 37
4.1. Methods for calculations of the spatial impulse response 37
4.1.1. Planar circular aperture 40
4.1.2. Focused circular aperture 47
4.1.3. The general aperture 51
4.1.4. Annular arrays 52
4.2. Calculated results 55
4.2.1. The focused circular disc 56
4.2.2. The planar disc and the natural focus .. 69
4.2.3. Annular arrays and dynamic focusing 76
4.2.4. A focused annular array 86
5. TRANSDUCER DESIGN AND MEASUREMENTS 94
5.1. Transducer design 94
5.2. Transducer measurements 99
5.2.1. The single element transducer 100
5.2.2. The two-element transducer 104
6. MEASUREMENTS OF THE TRANSIENT DIFFRACTION PATTERNS ... 110
6.1. The single element transducer 110
6.2. The two-element transducer 118
7. CALCULATIONS AND MEASUREMENTS OF THE ECHO RESPONSE ... 132
8. CONCLUSIONS 142
LIST OF REFERENCES 144

1. INTRODUCTION

Transient field propagation from ultrasonic pistons is the subject of this thesis. The purpose is to develop tools to simulate and design transducers for both cardiographic echo imaging and doppler velocity measurements.

Ultrasonic pulse echo systems are widely used in medical examinations. Best known is the prenatal examination, but also the heart, the liver and other organs are examined using ultrasound.

An important parameter in an imaging system is the resolution of the image. In an ultrasonic imaging system it is most often the transducer that represents the limitation. The capability of the transducer to generate short pulses limits the depth resolution. The diffraction from the aperture limits the lateral resolution.

The doppler velocity measurements have become very important in cardiological examination. The flow velocity of the blood is calculated from the frequency shift in the backscattered wave from the blood. A most critical parameter here is the sensitivity of the system.

It is often desirable to combine imaging and velocity measurements in one and the same system. This requires a transducer with high sensitivity as well as a large bandwidth to produce short pulses.

For the depth resolution to be better than one millimeter, it is necessary to use a frequency of at least 3 MHz. On the other hand the losses in biological tissue are approximately proportional with frequency. Thus, the sensitivity decreases as the frequency increases, and the choice of frequency here will therefore be 3 MHz. Depending on the application, transducers in the range 1-10 MHz are in use in cardiology today.

The lateral resolution is given mainly by the aperture of the transducer. The imaging depth ranges from about 2 cm to about 15 cm. In the near field the resolution will gain from a small focused aperture. In the far field the resolution will gain from a large unfocused aperture. For heart imaging the choice of diameter will be in the range 10-20 mm, also limited by the space between the ribs. In the choice of focusing and apodization there are no restrictions.

This work has two goals:

1. To develop a computer simulation program for analysing piston transducers and transient wave propagation from such.
2. To design transducers for simultaneous two-dimensional imaging and blood velocity measurements based on mechanical scanning.

The calculations of transient wave propagation are based on the spatial impulse response method [1,2,3]. In Chapter 2 the theory for this will be given. A model for the total echo response will be presented and losses will be included in the model.

Calculations of the transducer are based on the transmission line model [4]. In Chapter 3 this model is used to analyse the transducer. In particular we will seek to increase the bandwidth without reducing the sensitivity. Quarterwave matching layers are well suited to meet these requirements.

Calculations of transient fields are presented in Chapter 4. We shall see how the transmitted pulse and the aperture influence both the diffraction and the pressure pulse. The focal length is influenced both by a lens and by the excitation pulse, and we shall investigate the relationship. Dynamic focusing is achieved by controlling the time delay to the elements of an annular array. The number of elements required and the inprovement in resolution will be investigated.

Chapter 5 is the beginning of the experimental part. Here the design and measurements of the transducer elements will be presented. Chapter 6 presents the measurements of the diffraction fields. The measurements show that the calculations are in good agreement with reality.

The echo response is the most important figure for analysing an imaging system. Both calculations and measurements are presented in Chapter 7. On the basis of these it is possible to find the signature of different objects and obtain information about them.

2. THEORY OF TRANSIENT FIELDS

In order to analyse a pulse echo system it is necessary to understand transient wave propagation. It is the pulse length and the beam width that gives the resolution of the image.

The need to understand transient fields has led to the development of the spatial impulse response method. The method was initiated by P.R. Stepanishen [1,2,3] for uniformly vibrating pistons and was further developed by Fink [5], Arditi [6] and Harris [7]. An overview of the method is given by Harris [8].

In this chapter we shall develop the spatial impulse response method. We shall demonstrate how the diffraction can be separated into a spatial impulse response and a surface velocity. Medium losses will be included, and finally we shall see how a pulse echo system can be modelled by the use of this method.

2.1. The spatial impulse response method

The starting point for the spatial impulse response method is the Rayleigh integral [9],

$$\varphi(\vec{r},t) = \int_S \frac{v_n(\vec{r}_0, t - R/c)}{2\pi R} \, dS \qquad (2.1)$$

where φ is the velocity potential at the point $\vec{r}$ at time t, v_n is the normal velocity component at the surface S in position $\vec{r}_0$, and R is the distance between $\vec{r}$ and $\vec{r}_0$ as shown in fig.2.1. c is the sound velocity in the medium.

In the strict sense this integral is valid only for a plane transducer in an infinite and rigid baffle. The infinite medium should be homogeneous, lossless and non-dispersive.

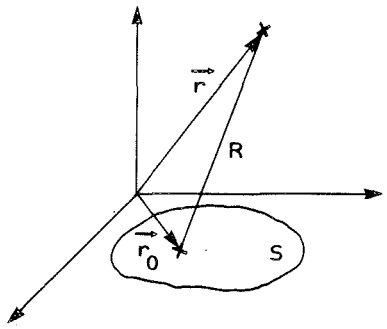

Fig. 2.1. Geometry for the Rayleigh integral.

As a typical excitation surface, consider a 3 MHz transducer element with diameter 12.7 mm or 25 wavelengths in water. This gives a highly directive beam and the influence of the baffle will be negligible. The properties of the medium will be discussed later.

We assume that the normal velocity component as a function of time, v(t), is the same throughout the whole surface, but in such a manner that the amplitude, $A(\vec{r}_0)$, might vary as a function of position. Further, we assume that v(t) might have a time delay, $\tau(\vec{r}_0)$, as a function of the position.

$$v_n(\vec{r}_0, t) = A(\vec{r}_0)\ v(t-\tau(\vec{r}_0)) \qquad (2.2)$$

This form makes it possible to describe general apodization and focusing. The Rayleigh integral now takes the form:

$$\varphi(\vec{r}, t) = \int_S \frac{A(\vec{r}_0)\ v(t- R/c\ -\tau)}{2\pi R}\, dS \qquad (2.3)$$

By applying the convolution theorem for the Dirac δ-pulse we can rewrite the expression

$$\varphi(\vec{r},t) = \int_{-\infty}^{\infty} v(\sigma) \int_S \frac{A(\vec{r}_0)}{2\pi R}\, \delta(t - R/c - \tau - \sigma)\, dS\, d\sigma$$

$$= v(t) * h(\vec{r},t) \qquad (2.4)$$

Thus we have:

$$h(\vec{r},t) = \int_S \frac{A(\vec{r}_0)}{2\pi R}\, \delta(t - R/c - \tau)\, dS \qquad (2.5)$$

This is called the spatial impulse response. We can see that the surface velocity v(t) of the transducer is to be convolved with the spatial impulse response to give the velocity potential. This means that the spatial impulse response corresponds to the velocity potential in a point $\vec{r}$ at time t when the aperture S is excited by a δ-pulse.

The velocity potential yields the pressure p, and the velocity $\vec{v}$:

$$p(\vec{r},t) = \varrho \frac{\partial}{\partial t} \varphi(\vec{r},t) \qquad (2.6)$$

$$\vec{v}(\vec{r},t) = -\text{grad}\, \varphi(\vec{r},t) \qquad (2.7)$$

Here ϱ is the density of the medium.

2.2. Dispersion and losses

So far we have assumed the medium to be homogeneous, lossless and non-dispersive. In this section we will examine these conditions.

An ultrasonic transducer used for cardiographic imaging is non-invasive. The beam penetrates the skin, fat, muscles, connective tissue and blood. The medium is by no means homogeneous. It is in fact the inhomogeneities that are the

origin of the scattered wave. The changes in acoustic impedance are however so small that the transmitted wave is not essentially decreased. Some data are listed in Table 2.1.

Tissue	Velocity [m/s]	Impedance [Mrayl]
Fat	1460	1.35
Muscle	1540 - 1630	1.65 - 1.74
Blood	1560	1.62
Liver	1530 - 1580	1.64 - 1.68
Kidney	1560	1.62
Bone	2700 - 4100	3.75 - 7.38

Table 2.1. Acoustic data for some biological tissues taken from [10].

We therefore adopt the following model:

- The sound propagates in a homogeneous medium.
- The objects are local variations in impedance and can be treated individually and independent of each other.

In this model an object can also be a structure of variations in impedance. The layered structure of a wall should be treated as a single object, but the front wall and the back wall of the heart can be treated separately. In general it is reasonable to assume that two variations in impedance can be treated separately if the distance between them is greater than one pulselength.

Losses in some biological tissues are shown in Table 2.2. We can see that the losses vary in both magnitude and frequency dependence. It is also here necessary to introduce some simplifications. We adopt the following model:

- The losses are the same throughout the whole medium.
- The losses are proportional with frequency.

This model is based on practical experience and the average losses are about 1 dB per MHz and cm.

Tissue	Attenuation coefficient at 1 MHz [dB/cm]	Frequency dependence (1-5 MHz)
Water	0.002	f^2
Hemoglobin	0.1	$f^{1.3}$
Soft tissue	0.3 - 1.5	f
Muscle	1.5 - 2.5	f
Ivory bone	3	f
Skull bone	10	$f^{1.5}$

Table 2.2. Data for losses and frequency dependence in biological tissue from [10].

This loss model can be included in the method with the spatial impulse response as shown by Fink [5]. For a point source in an infinite baffle that is excited by a δ-pulse, the velocity potential at a distance R can be written

$$h(\vec{r},t) = \frac{1}{2\pi R}\,\delta(t - R/c) \qquad (2.8)$$

The Fourier transform with respect to time is:

$$H(\vec{r},\omega) = \frac{1}{2\pi R}\,e^{-j\frac{\omega}{c}R} \qquad (2.9)$$

where ω is the angular frequency. Introducing the loss model yields:

$$H_A(\vec{r},\omega) = \frac{1}{2\pi R}\,e^{-j\frac{\omega}{c}R}\;e^{-\alpha|\omega|R} \qquad (2.10)$$

Here α is the attenuation per unit frequency and distance. The inverse Fourier transform gives us:

$$h_A(\vec{r},t) = \frac{1}{2\pi R} \frac{2\alpha R}{\alpha^2 R^2 + (t - R/c)^2} \tag{2.11}$$

Considering an aperture S the spatial impulse response in Eq. (2.5) will become:

$$h_A(\vec{r},t) = \int_S \frac{A(\vec{r}_0)}{2\pi R} \frac{2\alpha R}{\alpha^2 R^2 + (t - R/c - \tau)^2} \, dS \tag{2.12}$$

Again we can use the convolution theorem for δ-pulses.

$$h_A(\vec{r},t) = \int_S \frac{A(\vec{r}_0)}{2\pi R} \int_{-\infty}^{\infty} \delta(t - R/c - \tau - \sigma) \frac{2\alpha R}{\alpha^2 R^2 + \sigma^2} \, d\sigma \, dS \tag{2.13}$$

At this point we must introduce a simplification. R is the distance between the source and the observation point and therefore a variable over the aperture. For the attenuation however, this dependence is not important. It is in the far field that the attenuation is important and there the distance is nearly a constant over the aperture. In the fraction which accounts for the losses we therefore replace the distance R with a constant r, which is the distance from the centre of the aperture to the observation point. Thus the expression for the losses can be put outside the integral.

$$h_A(\vec{r},t) = \int_{-\infty}^{\infty} \frac{2\alpha r}{\alpha^2 r^2 + \sigma^2} \int_S \frac{A(\vec{r}_0)}{2\pi R} \delta(t - R/c - \tau - \sigma) dS \, d\sigma$$

$$= h(\vec{r},t) * \frac{2\alpha r}{\alpha^2 r^2 + t^2} \tag{2.14}$$

$$= h(\vec{r},t) * l(\alpha r, t)$$

$h(\vec{r},t)$ is the spatial impulse response as in Eq. (2.5) and $l(\alpha r,t)$ will be called the loss function. This simplified expression ensures that it is only the spatial impulse response that depends on the aperture.

It is important to note that the development above can be repeated for any loss function. The loss function that is used in the development is non-causal. Our knowledge about the losses is that the power decreases proportional with the frequency. Thus the module of the Fourier transform of the loss function can be written:

$$|L(\omega)| = e^{-\alpha|\omega|R} \qquad (2.15)$$

The next requirement is that the loss function must be causal. This can be achieved by letting the phase of the loss function be the Hilbert transform of the natural logarithm of the module. For computer simulations we can use the expression found in Oppenheim [11]:

$$\arg[L(\omega)] = \frac{1}{2\pi} P \int_{-\pi}^{\pi} \ln|L(\theta)| \operatorname{cotg}\left(\frac{\theta-\omega}{2}\right) d\theta \qquad (2.16)$$

where ω is the sampling frequency and P denotes the Cauchy principal value. By choosing this method we also have assumed that the function is of minimum phase. An analysis of this approach is given by Kuc [12] together with a Fortran algorithm for the Hilbert transform. In Fig. 2.2 is shown a computation of the loss function as a function of time with αr equal to 1.72 μs which corresponds to an attenuation of 1 dB/cm MHz and a depth of 15 cm.

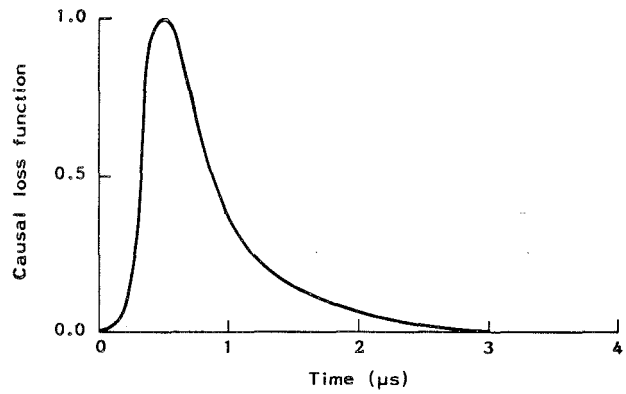

Fig. 2.2. The causal loss function with αr = 1.72 μs.

We can see that the causal loss function goes to zero at t equal to zero, while the loss function in Eq. (2.14) is symmetrical around t equal to zero. According to Eg. (2.14) the loss function is to be convolved with the spatial impulse response to give the attenuated spatial impulse response. If therefore the length of the loss function or the time constant αr is of the same order and longer than the non-attenuated impulse response, the losses will strongly influate on the result.

Finally we will see if the losses lead to dispersion. The one dimensional wave equation for the velocity in a medium with viscuos losses is

$$\frac{\delta^2 v}{\delta x^2} = \frac{1}{c^2}\frac{\delta^2 v}{\delta t^2} + \eta \frac{\delta v}{\delta t} \qquad (2.17)$$

where η and c are constants. Assuming harmonic fields, the dispersion relation becomes

$$\gamma^2 = -\frac{\omega^2}{c^2} + j\omega\eta \qquad (2.18)$$

Here j is the imaginary unit and γ is the propagation constant defined by

$$\gamma = \alpha + j\,k \tag{2.19}$$

Here α is the attenuation constant and k the wavenumber. Elimination of γ from Eq. (2.18) and Eq. (2.19) gives:

$$k^2 = \frac{\omega^2}{c^2} + \alpha^2 \tag{2.20}$$

$$\eta = \frac{2\alpha k}{\omega} \tag{2.21}$$

Introducing losses that are proportional with frequency

$$\alpha = \alpha_0\ \omega \tag{2.22}$$

we get

$$k = \frac{\omega}{c}\ \sqrt{1 + (\alpha_0\ c)^2} \tag{2.23}$$

Thus k is proportional with ω and the medium is non-dispersive. This is an important result because it gives us the possibility of doing the calculations in the time domain. If the losses are 1 dB per MHz and cm and the constant c is 1500 m/s, the constant in Eq. (2.23) becomes

$$\sqrt{1 + (\alpha_0\ c)^2} = 1.014 \tag{2.24}$$

For all practical purposes we can write

$$k = \frac{\omega}{c} \tag{2.25}$$

When the losses are proportional with frequency, then the phase and group velocity are equal, and for all practical purposes equal to the constant c.

2.3. The echo response

So far in this chapter we have endeavoured to put up independent expressions for the diffraction and for the

losses. We can now find the pressure at a point in space as a function of time from

$$p(t) = \varrho \frac{\partial}{\partial t} v(t) * h(t) * l(t) \qquad (2.26)$$

where all the symbols are defined earlier. In the next chapter we will develop an expression for the transducer transfer function and impulse response, g(t), defined by

$$v(t) = g(t) * u(t) \qquad (2.27)$$

where u(t) is the generator voltage. Together with Eq. (2.26) this gives

$$p(t) = \varrho \frac{\delta}{\delta t} u(t) * g(t) * h(t) * l(t) \qquad (2.28)$$

This expression can be interpreted as a cascade of three networks, as shown in Fig. 2.3.

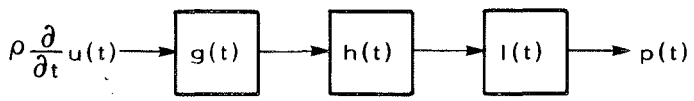

Fig. 2.3. The network model from voltage to pressure.

The great advantage with this model is that each network can be treated separately. We shall now go a step further and establish a total model for the echo response using the reciprocity theorem.

For a passive and linear twoport the following holds: If a voltage V_g on port 1 puts up a current I through the impedance Z_L on port 2, then a voltage V_g in series with Z_L on port 2 will put up the same current I through Z_g on port 1. See Fig. 2.4 for definitions.

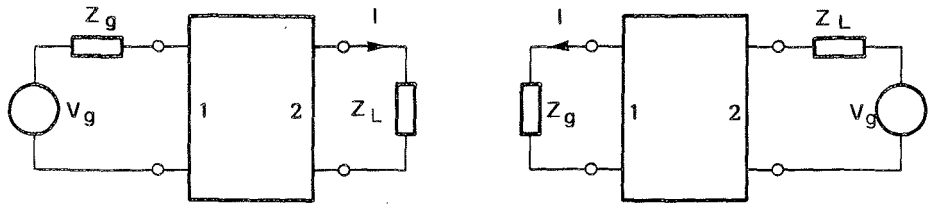

Fig. 2.4. Illustration of the reciprocity theorem.

This is one formulation of the reciprocity theorem. A more general formulation can be found in [13]. When used on acoustic twoports the voltage must be exchanged with a force and the current with a velocity.

Considering the transducer, this means that the same impulse response is valid for both transmission and reception.

$$v_1(t) = g(t) * u(t)$$

$$i(t) = g(t) * f_1(t) \qquad (2.29)$$

Here $u(t)$ is the generator voltage and $v_1(t)$ is the velocity out of the acoustic port during transmission. $f_1(t)$ is the incoming force on the acoustic port and $i(t)$ is the current through the generator impedance during reception. We have of course assumed that the parameters are unchanged.

Further we assume that the impulse response of a point object can be written as $s(t)$.

$$v_2(t) = s(t) * p_2(t) \qquad (2.30)$$

Here $p_2(t)$ is the incoming pressure on the object and $v_2(t)$ the reflected velocity from the object. If the object is small compared to the wavelength, then we can assume that the pressure is constant over the equivalent surface of the object, A. The force on the object is then:

$$f_2(t) = A\, p_2(t) \tag{2.31}$$

From Eqs. (2.4), (2.6) and (2.31) we get:

$$f_2(t) = A\, \varrho \left(\frac{\partial}{\partial t} v_1(t) \right) * h(t) \tag{2.32}$$

The reciprocity theorem applied to the spatial impulse response gives us the resulting force on the transducer.

$$f_1(t) = A\, \varrho \left(\frac{\partial}{\partial t} v_2(t) \right) * h(t) \tag{2.33}$$

The total echo response can then be found from Eqs. (2.29) - (2.33).

$$i(t) = A\, \varrho^2 \left(\frac{\partial^2}{\partial t^2} u(t) \right) * h(t) * h(t) * g(t) * g(t) * s(t) \tag{2.34}$$

It is now the current i(t) that contains the information about the object s(t). The representation will be perfect if g(t) and h(t) are δ-pulses. It is therefore important to find g(t) and h(t) to study their influence on the total echo response.

The next problem will be to find an expression for the impulse response of the object, s(t). To do this we need to introduce a simplification. We assume that the waves at the object are planar, so that the ratio between pressure and velocity in the medium is given by the characteristic impedance, ϱc. The reflected pressure can then be written as:

$$p_r(t) = \varrho c \left(v_2(t) \right) \tag{2.35}$$

Using Eq. (2.30) we get:

$$p_r(t) = \varrho c \left(s(t) * p_2(t) \right) \tag{2.36}$$

We can see that $\varrho c\, s(t)$ is the inverse Fourier transform of the well known reflection coefficient for planar waves, $C(\omega)$.

$$s(t) = \frac{1}{\varrho c} \frac{1}{2\pi} \int_{-\infty}^{\infty} C(\omega)\, e^{j\omega t}\, d\omega \qquad (2.37)$$

From here on we can use the formulas in plane wave theory to find the impulse response of the object [14].

The above assumptions of planar waves are most likely to be true in the far field and for large objects. If the object is so large that the various contributions differ significantly in timedelay or magnitude it can be divided into many smaller objects, and the contribution from each part can be summed due to the principle of superposition. The resulting force on the transducer is then:

$$f(t)_{tot} = \sum_{n=1}^{N} f_{1n}(t) \qquad (2.38)$$

Here $f_{1n}(t)$ is the force on the transducer from the area ΔA_n and all together there are N such areas. Fig. 2.5 shows schematically the various contributions to the total echo response in this case. The area ΔA_n is in the position $\vec{r}_n$.

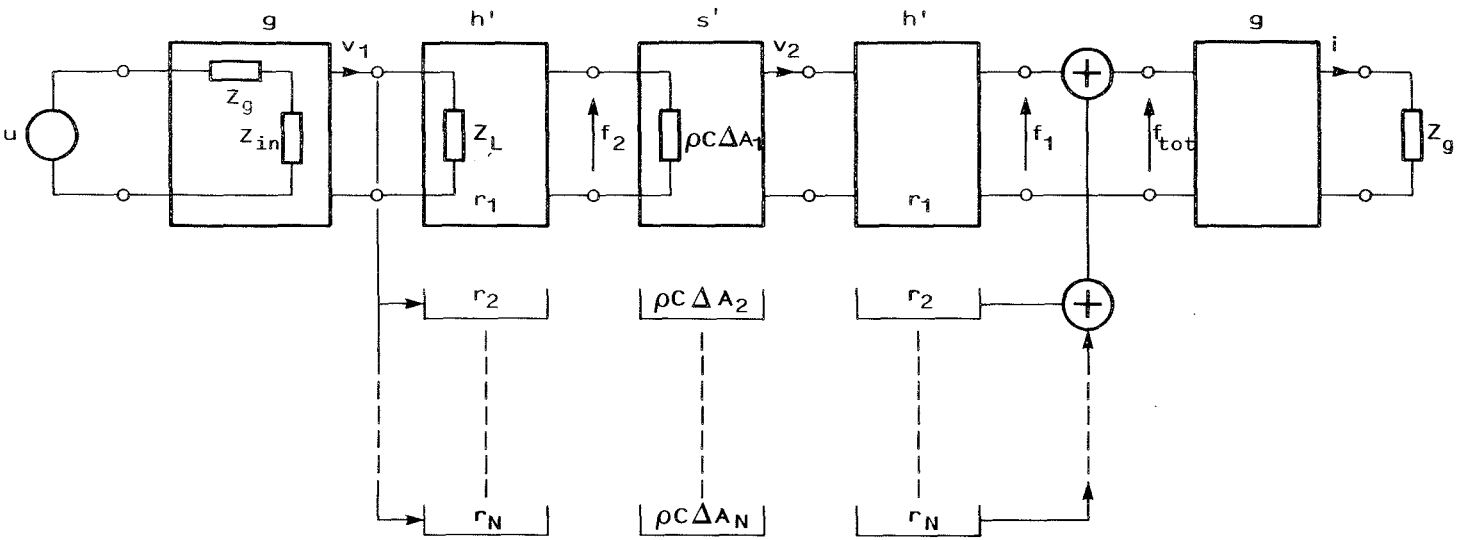

Fig. 2.5. The total pulse echo response model.

$v_1 = g * u$, $f_2 = h' * v_1$, $v_2 = s * f_2$, $f_1 = h' * v_2$, $f_{tot} = \sum_N f_{1n}$, $i = g * f_{tot}$

$$h'(\vec{r}, t) = \rho \Delta A \frac{\partial}{\partial t} h(\vec{r}, t)$$

$$s'(t) = s(t)/\Delta A$$

3. TRANSDUCER MODELLING AND CALCULATIONS

In the previous chapter we summarized the diffraction theory. This will enable us to design an appropriate aperture function. In this chapter we will analyse the transducer itself and see how the front velocity can be calculated. We will also calculate the transfer function and the electric input impedance.

As mentioned earlier, we want to design a transducer for both echo imaging and doppler measurements. The echo imaging requires a pulse length that is shorter than 1 mm or 2 wavelengths at 3 MHz. Thus we need a 50% bandwidth. On the other hand the doppler measurements require high sensitivity. A good doppler transducer should have an efficiency of better than 50%.

The transducer material we will use is lead-zirconate titanate (PZT). The reason for this is its high coupling efficiency. The greatest disadvantage is its high acoustic impedance. The impedance varies for the different types, but is about 35 Mrayl (10^6 kg/m^{2}s). This is around 20 times the impedance of water and biological tissue. The coupling between the transducer and the medium will therefore be poor if nothing is done.

In this chapter we shall first outline a calculation model for the transducer. Secondly, we will use the model to investigate the performance of the transducer.

3.1. The calculation model

A piezoelectric transducer for pressure wave generation is in general made of a disc of PZT with silver electrodes on both sides. The electrodes are the electric port, and the surfaces of the disc are the mechanical ports, see Fig. 3.1. When the transducer is in mechanical contact with air, water or

biological tissue, both parallel and series resonance are near a frequency that makes the transducer half a wavelength thick or possibly one half wavelength plus an integer number of wavelengths. At resonance the electric input impedance has a large real part, and power can be fed into the element. To gain the greatest possible relative bandwidth we chose the element to be half a wavelength thick. At 3 MHz and a bulk velocity of 4500 m/s the thickness will be 0.75 mm. As mentioned earlier, the diameter of the disc in our application will be 10-20 mm. Thus we are dealing with thin disc transducers.

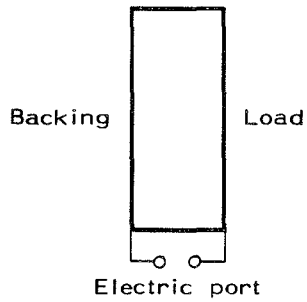

Fig. 3.1. A piezoelectric element for pressure wave generation.

Three different calculation models have been used for thin disc transducers. The first one is the Mason model [15] which is an equivalent circuit consisting of passive electric components. The second one is the impulse response model [16,17]. The idea here is that an impulse is generated at the electrodes and is reflected back and forth in the element with a fractional transmission at each reflection. The last model is called the transmission line model and was introduced by Krimholtz, Leedom and Matthaei [4]. This model will be used here. The reason for this is that the model gives a better understanding of the quarterwave matching layers.

A detailed outline of the transmission line model is given in [4,18,19] and will not be repeated here. We will only present the results as shown in Fig. 3.2.

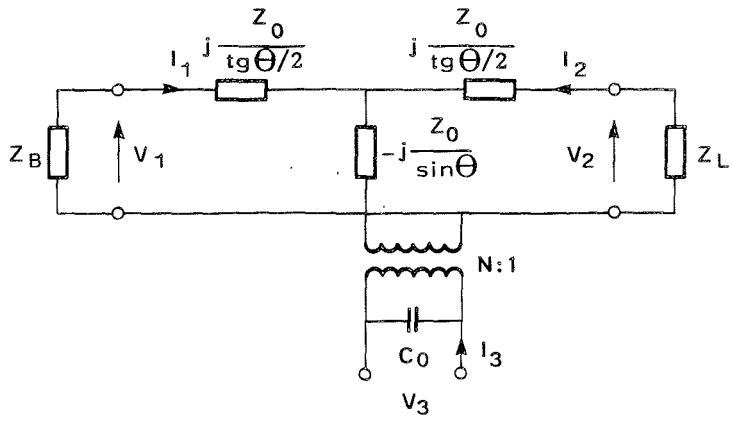

Fig. 3.2. The transmission line model after Krimholtz, Leedom and Matthaei [4].

Here the following definitions are used

$$k_0 = \omega \sqrt{\frac{\varrho}{\kappa}} \tag{3.1}$$

$$\theta = k_0 t \tag{3.2}$$

$$Z_0 = \frac{k_0 \kappa A}{\omega} \tag{3.3}$$

$$C_0 = \frac{\varepsilon_0 \varepsilon A}{t} \tag{3.4}$$

$$N = h C_0 \tag{3.5}$$

And we have the following notations:

- ω - angular frequency
- ϱ - density
- κ - compressibility
- ε_0 ε - dielectric constant under constant strain
- h - piezoelectric constant
- t - thickness of the disc

A - area of the disc
k_0 - wavenumber
θ - thickness of the disc in degrees
C_0 - capacitance of the disc
N - coupling factor
Z_0 - acoustic impedance of the disc
Z_L - load impedance
Z_B - backing impedance
V_1 - force on front port
I_1 - velocity into front port
V_2 - force on back port
I_2 - velocity into back port
V_3 - voltage on electric port
I_3 - current into electric port

In solid media the wave-equation will in general have nine independent solutions, one pressure wave and two shear waves in each of the three directions of space. The transmission line model takes only one of these solutions into account, namely the pressure wave perpendicular to the disc. The model is therefore said to be one-dimensional. This approximation also applies to the Mason model and to the impulse model.

Fluid media and soft tissue will only propagate pressure waves due to the fact that the medium can only store potential energy in volume alteration and not in shape alteration. The generation of waves in these media is therefore determined by the normal velocity at the surface of the transducer. Modes that give a normal velocity on the surface of the transducer are therefore the most important, but the others will store energy and thereby increase the ring time. We will however concentrate on the mode that can be calculated from the transmission line model, but have in mind that also other modes can influence the acoustic field. Our primary concern is the field in the medium and not in the transducer itself.

We shall now develop some mathematical expressions used in the calculations of the transducer. First of all, we are interested in the transfer function from the electric port

to the acoustic front port. From Fig. 3.2 we can put up the following equations:

$$V_1 = I_1 \frac{Z_0}{j\ tg\theta} + I_2 \frac{Z_0}{j\ sin\theta} + I_3 \frac{N}{j\omega C_0} \qquad (3.6)$$

$$V_2 = I_1 \frac{Z_0}{j\ sin\theta} + I_2 \frac{Z_0}{j\ tg\theta} + I_3 \frac{N}{j\omega C_0} \qquad (3.7)$$

$$V_3 = I_1 \frac{N}{j\omega C_0} + I_2 \frac{N}{j\omega C_0} + I_3 \frac{1}{j\omega C_0} \qquad (3.8)$$

All the symbols are defined in connection with Fig. 3.2 or in Eqs. (3.1)-(3.5) We terminate the acoustic ports so that:

$$V_1 = - Z_B \quad I_1 \qquad (3.9)$$

$$V_2 = - Z_L \quad I_2 \qquad (3.10)$$

From Eqs. (3.6) - (3.10) we can eliminate all the unknowns except I_2 and V_3, and thereby find an electro-acoustic transfer function.

$$\frac{I_2}{V_3} = \frac{B - D}{\frac{Z_L}{N} D - C Z_L + \frac{A}{N} D - AC - \frac{B^2}{N} - CD + 2BC} \qquad (3.11a)$$

where we have defined

$$A = \frac{Z_0}{j\ tg\theta} \qquad (3.11b)$$

$$B = \frac{Z_0}{j\ sin\theta} \qquad (3.11c)$$

$$C = \frac{N}{j\omega C_0} \qquad (3.11d)$$

$$D = Z_B + \frac{Z_0}{j\ tg\theta} \qquad (3.11e)$$

Another expression of interest is the electric input impedance. Elimination of all the unknowns in Eqs. (3.6) - (3.10) except V_3 and I_3 gives:

$$Z_3 = \frac{V_3}{I_3} = \frac{1}{j\omega C_0} + \frac{N^2}{\omega^2 C_0^2 Z_0} \quad \frac{2Z_0(\cos\theta - 1) + j(Z_L + Z_B)\sin\theta}{(Z_L+Z_B)\cos\theta + j(Z_0 - \frac{Z_L Z_B}{Z_0})\sin\theta} \tag{3.12}$$

For system evaluations it is more convenient to calculate the generator voltage, V_g, to front velocity, I_2, transfer function. If the generator impedance is Z_g we get:

$$\frac{I_2}{V_g} = \frac{I_2}{V_3} \frac{Z_3}{Z_g + Z_3} \tag{3.13}$$

where I_2/V_3 is given in Eq. (3.11) and Z_3 in Eq. (3.12). The impulse response can now be found by inverse Fourier transformation.

$$g(t) = \int_{-\infty}^{\infty} \frac{I_2}{V_g} e^{j\omega t} \, d\omega \tag{3.14}$$

To discuss the results in Eqs. (3.12) to (3.14) we carry out a calculation of the transfer function, impulse response and input impedance. The data for PZ27 or PZT5A are given in [20]

$h = 22 \times 10^8$ V/m

$\varepsilon^S = 830$

$c^D = 4350$ m/s

$Z_0 = 34$ Mrayl (10^6 kg/sm^2)

and we choose

diameter: d = 12.7 mm

thickness: t = 0.69 mm

Taking water as the load medium and air as the backing.

Z_L = 1.5 Mrayl

Z_B = 360 rayl

The results of the calculations are shown in Fig. 3.3. The module of the transfer function and the impulse response is normalized so that the peak value is one.

The transfer function shows that with the chosen thickness the maximum transfer is around 3 MHz. The exact frequency is given also by the electric generator impedance. Maximum transfer of power takes place when the generator impedance is the complex conjugated of the input impedance. In the calculations 50 Ω has been used as the generator impedance. The maximum transfer will lie between the series and parallel resonance. In this range the module of the input impedance varies from a small value to a large value, depending on the load.

The calculations of the input impedance also show that the transducer is purely capacitive for all frequencies except around resonance. Only in the neighbourhood of the series and parallel resonance the impedance has a significant real component and possibility for input of power.

The relative bandwidth of the transfer function is about 25% and the 20 dB pulselength is about 2 μs. This gives a depth resolution of 3 mm in water and in biological tissue.

Finally, we note that the transfer function goes to zero at twice the resonance frequency. This gives a theoretical limit for the bandwidth. With a bandwidth of twice the resonance frequency we get a pulse that is around half a period long.

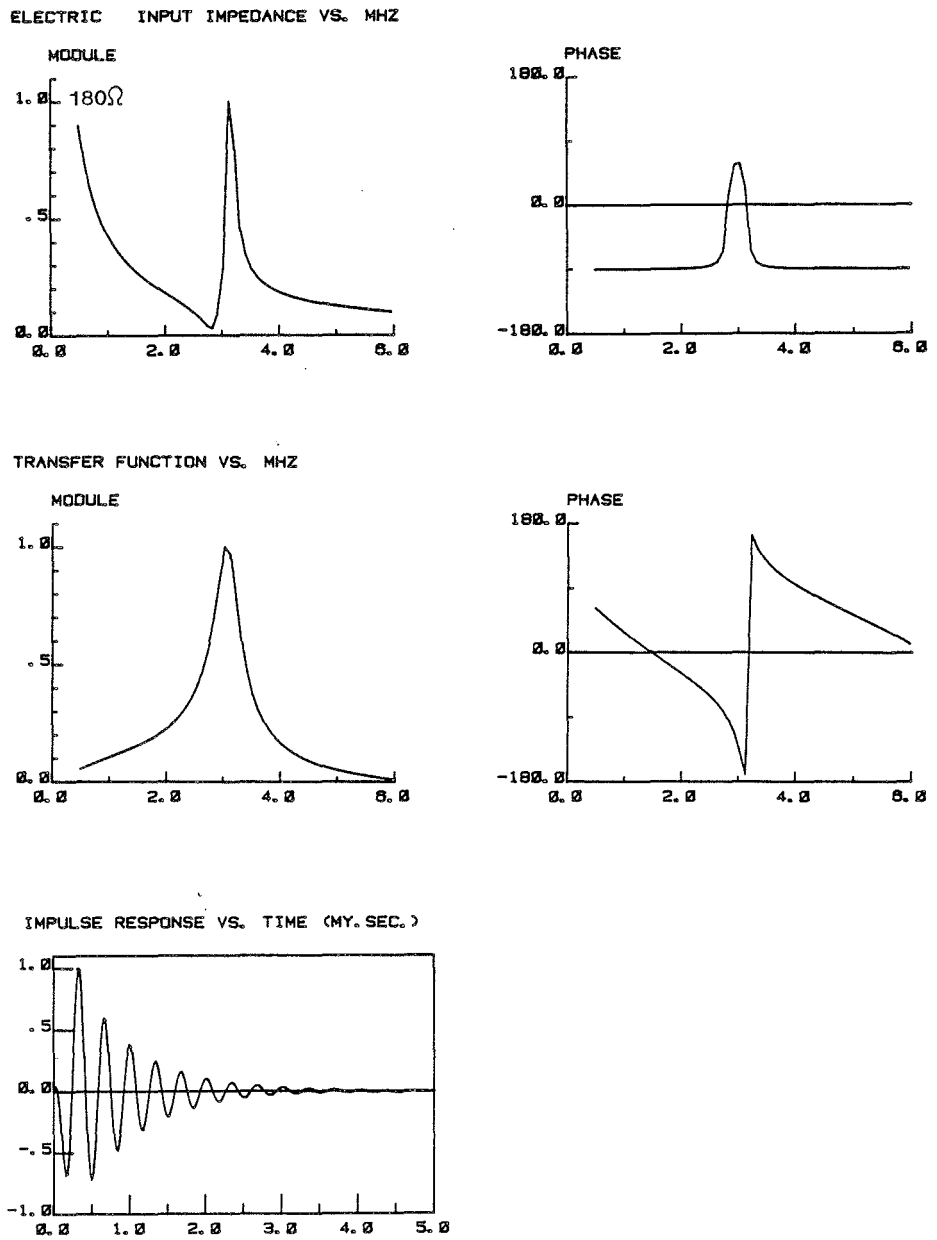

Fig. 3.3. Calculations of electric input impedance, transfer function and impulse response for a PZ27 element with water load and air backing. The disc diameter is 12.7 mm and the centre frequency is 3 MHz.

3.2. Transducer losses

The transmission line model as described in the previous section is lossless. We will now include a simple loss model.

There are two kinds of losses that are important. The first is the dielectric loss in the piezoelectric element and the second is the acoustic propagation loss in the element itself. Mason includes these losses as resistances in his model [15]. The dielectric loss is a resistance in parallel with the electric port. The acoustic propagation loss is a resistance in series with the acoustic load impedance. We will follow the same procedure.

From Ferroperm [21] we find that the loss angle for PZ27 is

$$\text{tg } \delta = 0.016 \tag{3.17}$$

With the data used in the calculations in the previous section the value of the parallel resistance is 2500 Ω. The real part of the input impedance can be seen in Fig. 3.3 to be far below this value. Thus the dielectric loss is not important and will not be included.

From Frazer [19] we find that the mechanical Q-factor for a thin disc transducer with low coupling can be written:

$$Q_m = \frac{\pi}{2} \left(\frac{Z_0}{Z_L + Z_B} \right) \tag{3.18}$$

Assuming that the acoustic propagation loss can be included as a resistance in series with the load we can write

$$Q_m = \frac{\pi}{2} \left(\frac{Z_0}{Z_L + Z_B + R_m} \right) \tag{3.19}$$

Here R_m is the acoustic resistance in the element. From Ferroperm [21] we find that the Q-factor for the element alone is 80. This gives a resistance of

$$R_m = \frac{\pi}{2} \cdot \frac{Z_0}{Q_m} = 0.66 \text{ Mrayl} \qquad (3.20)$$

We share the loss equally between the two acoustic ports so that $R_m/2$ is in series with both the load at the front and the back. Thus we have a loss model as shown in Fig. 3.4.

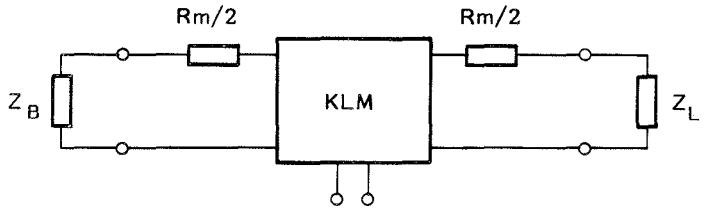

Fig. 3.4. Transducer loss model.

To verify the model the input impedance was measured on an element in air. The measurement is shown in Fig. 3.5.a. Calculations of the input impedance with and without the loss are shown in Fig. 3.5.b and c. Most sensitive to the loss in these plots is the peak of the phase plot. For the lossless case the peak is at + 90 degrees, but with the loss included the peak is at about + 80 degrees. The latter is in much better agreement with the measurement.

The measured impedance also shows a weak resonance at 2 MHz which is difficult to account for. We shall however, discuss spurious modes of vibration in Chapter 5. We also observe a series resonance at 5 MHz. This must be due to the inductance in the cable and the connector.

We also note that the measured module peak is higher than both calculated values. This is due to the fact that the peak is very narrow and the resolution in the calculations is 0.1 MHz, while in the measurement the frequency is adjusted to find the peak value. A serge for the peak in the calculations has shown that the peak value is 552 Ω when the acoustic losses are included. This value is so high that the dielectric losses will influence the result. With a parallel resistance of 2500 Ω on the input, the total result will be a peak value of 452 Ω. This is in good agreement with the measurement. For an element with a more realistic load, the peak value will be below 100 Ω and the dielectric losses will not be important anymore. In the lossless case the peak value of the module was found to be about 3000 Ω.

Finally, we will see how the loss modifies the impulse response. With the same parameters as in Fig. 3.3, but now with the loss included, Fig. 3.6 shows the impulse response from a transducer with water load and air backing. Comparing this with Fig. 3.3.c we observe that the two impulse responses are very similar. The ringdown time is however slightly shorter in the latter case.

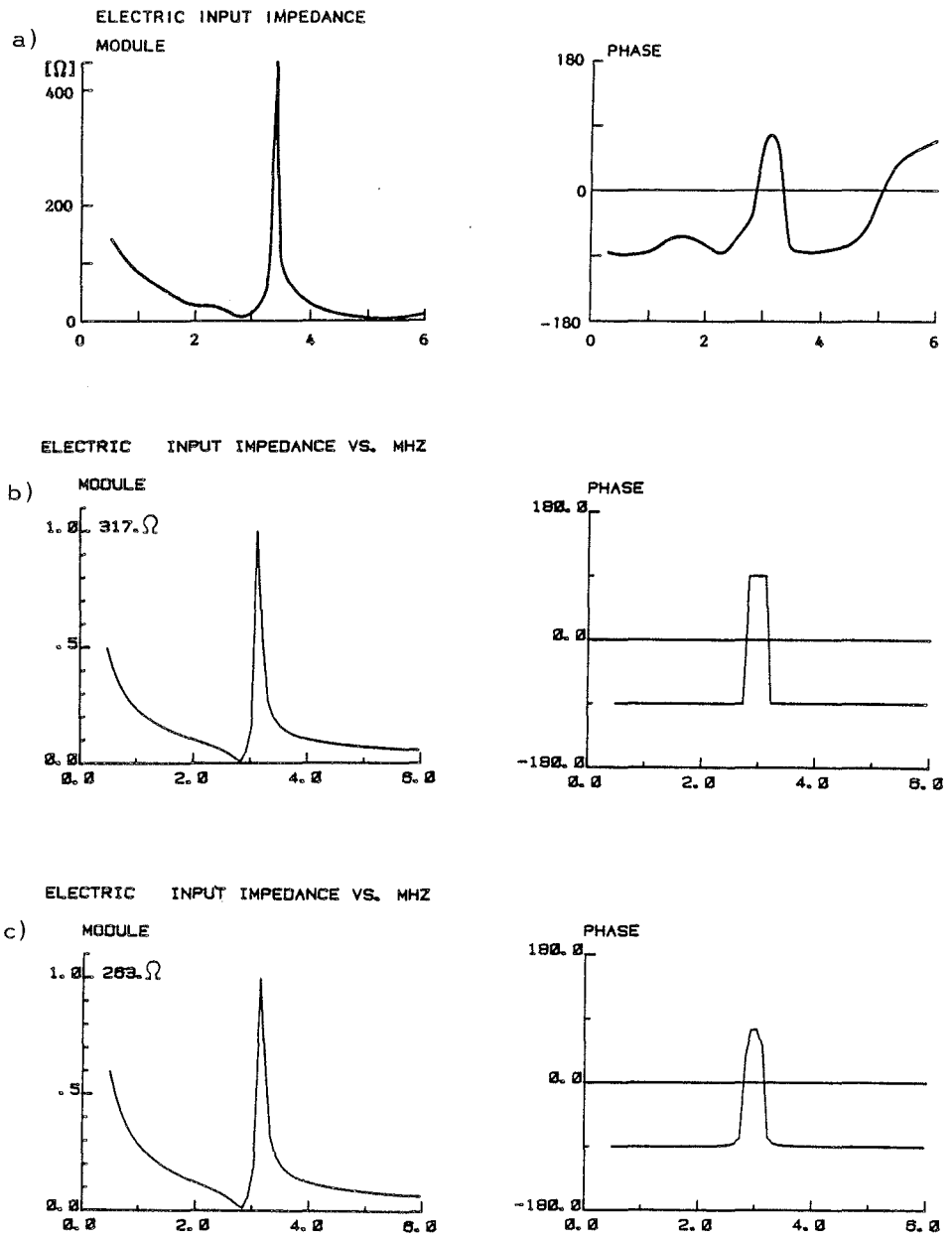

Fig. 3.5. Electric input impedance for a PZ27 element in air. The disc diameter is 12.7 mm and the centre frequency is 3 MHz.

a) Measurements
b) Calculations from the lossless model
c) Calculations from the model with losses.

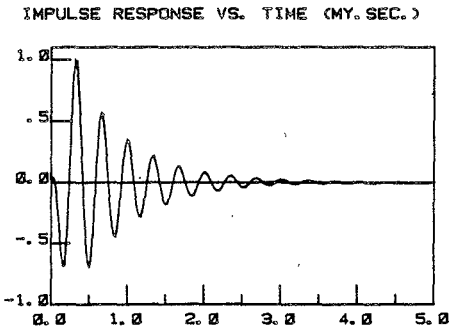

Fig. 3.6. Impulse response for a transducer with water load and air backing when the losses are included. The disc diameter is 12.7 mm and the centre frequency is 3 MHz.

3.3. Increase of bandwidth

Three different methods are in use to increase the bandwidth of thin disc transducers.

1. Use of a heavy backing with high impedance and high absorption
2. Acoustic matching with quarter-wave matching layers
3. Electric matching with inverse filters.

Transducers for echo imaging are often attached to a heavy backing material with an acoustic impedance that matches the element and has high absorption. This increases the coupling from the element and thereby reduces the ring down time. The power is however coupled to the backing and the sensitivity is therefore reduced as well. When the transducer is also to be used for doppler measurements the sensitivity is of great importance, and this method cannot be used.

Acoustic matching between the element and the medium will also increase the coupling and reduce the ring down time. In this case, however, the coupling is into the medium and the sensitivity is less effected.

It is well known that impedance matching between two transmission lines can be achieved with a quarterwave matching layer with an impedance which is the geometrical mean of the two transmission lines. A layer will however be a quarterwave thick for one frequency only. For transient pulses it is necessary that the matching has a certain bandwidth. We want the impulse response of the transducer to be compact, which means that the half value length should be as short as possible and that the tail of the pulse is as small as possible. The impulse response is the inverse Fourier transform of the transfer function. The transfer function should therefore have the largest possible bandwidth, but should also be as smooth as possible. For a given bandwidth a gaussian function would be the optimum.

For a finite number of layers, however, a gaussian transfer function cannot be achieved. We shall therefore use the impedances that give the maximum flat response for a finite number of layers. A thorough study of matching layers that gives maximally flat response can be found in De Silets [22]. The results of this study are given in Table 3.1, and are taken from Frazer [19].

Layer no.	1	2	3	Z_L'
1 layer	$Z_L^{2/3}\ Z_0^{1/3}$	-	-	$Z_L^{1/3}\ Z_0^{2/3}$
2 layers	$Z_L^{3/7}\ Z_0^{4/7}$	$Z_L^{6/7}\ Z_0^{1/7}$	-	$Z_L^{1/7}\ Z_0^{6/7}$
3 layers	$Z_L^{4/15}\ Z_0^{11/15}$	$Z_L^{10/15}\ Z_0^{5/15}$	$Z_L^{14/15}\ Z_0^{1/15}$	$Z_L^{1/15}\ Z_0^{14/15}$

Table 3.1. The impedances in the matching layers for maximally flat response when Z_0 is the element impedance, Z_L the load impedance. Z_L' is the modified load impedance.

We shall now see how the transfer function, impulse response and electric input impedance can be found for a transducer with matching layers. The input impedance in Eq. (3.12) and the transfer function in Eq. (3.11) are still valid if the load impedance, Z_L, is interchanged with the impedance seen through the matching layers, Z_L'. The transformation formula for the impedance in the i'th layer is:

$$Z_{Li}' = Z_{oi} \frac{Z_{Li} + j\, Z_{oi}\, tg\theta_i}{Z_{oi} + j\, Z_{Li}\, tg\theta_i} \qquad (3.21)$$

Here Z_{oi} is the acoustic impedance of the i'th layer and θ_i is the thickness of the i'th layer relativ to the wavelength measured in radians. Equation (3.21) is used successively for each layer from the medium to the element.

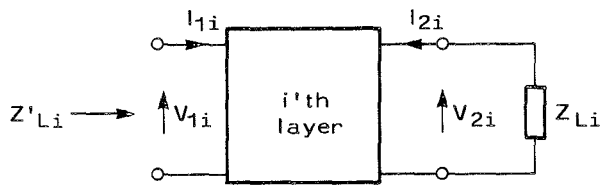

Fig. 3.7. Definition of the symbols used for the matching layers.

To find the total transfer function for the transducer we will have to find the transfer function for each layer. These layers have neither piezoelectric coupling nor an electric port. The equations (3.6) - (3.8) can therefore now be written for the i'th layer:

$$V_{1i} = I_{1i} \frac{Z_{oi}}{j\, tg\, \theta_i} + I_{2i} \frac{Z_{oi}}{j\, \sin\, \theta_i} \qquad (3.22)$$

$$V_{2i} = I_{1i} \frac{Z_{oi}}{j\, \sin\, \theta_i} + I_{2i} \frac{Z_{oi}}{j\, tg\, \theta_i} \qquad (3.23)$$

The symbols are defined in Fig. 3.7. For calculations of the transfer function it is better to have the equations on the cascade form.

$$V_{2i} = V_{1i}\cos\theta_i - j Z_{oi} I_{1i} \sin\theta_i \qquad (3.24)$$

$$I_{2i} = j \frac{V_{1i}}{Z_{oi}} \sin\theta_i - I_{1i}\cos\theta_i \qquad (3.25)$$

These equations can be used to find the total transfer function by applying them on the layers successively from the element to the medium. This formulation of the problem has been inspired by Angelsen [23].

Calculations of transfer functions and impulse responses for transducers with 1, 2 and 3 quarterwave matching layers are shown in Figs. 3.8 and 3.9. The data for the element is the same as before, and the impedances of the matching layer are those found in Table 3.1. We can see that the transfer functions in Fig. 3.8 are smooth and that the phases are nearly linear over the passband. The bandwidth increases with the number of layers. With one matching layer the 6 dB bandwidth is 1.6 MHz, with two matching layers the bandwidth is 2.3 MHz and with three matching layers the bandwidth is 2.8 MHz. This gives us impulse responses that decrease in length with the number of layers, as can be seen in fig. 3.9. The 12 dB pulse lengths are 0.9 μs, 0.6 μs and 0.5 μs with 1, 2 and 3 matching layers. The efficiency of the transducer is also enhanced with matching layers, due to the increased load impedance for the PZT-element. Using the loss model developed in the previous section, the efficiency is 68%, 94%, 97% and 98% with 0, 1, 2 and 3 matching layers for a transducer with airbacking. The losses in the matching layers is not significant.

The third possibility to improve the transducer transfer function is to use inverse filtering. Inverse filtering is in general of great importance in transmission systems, but will not be used here. In principle it is possible to shape a total transfer function arbitrarily with an inverse filter.

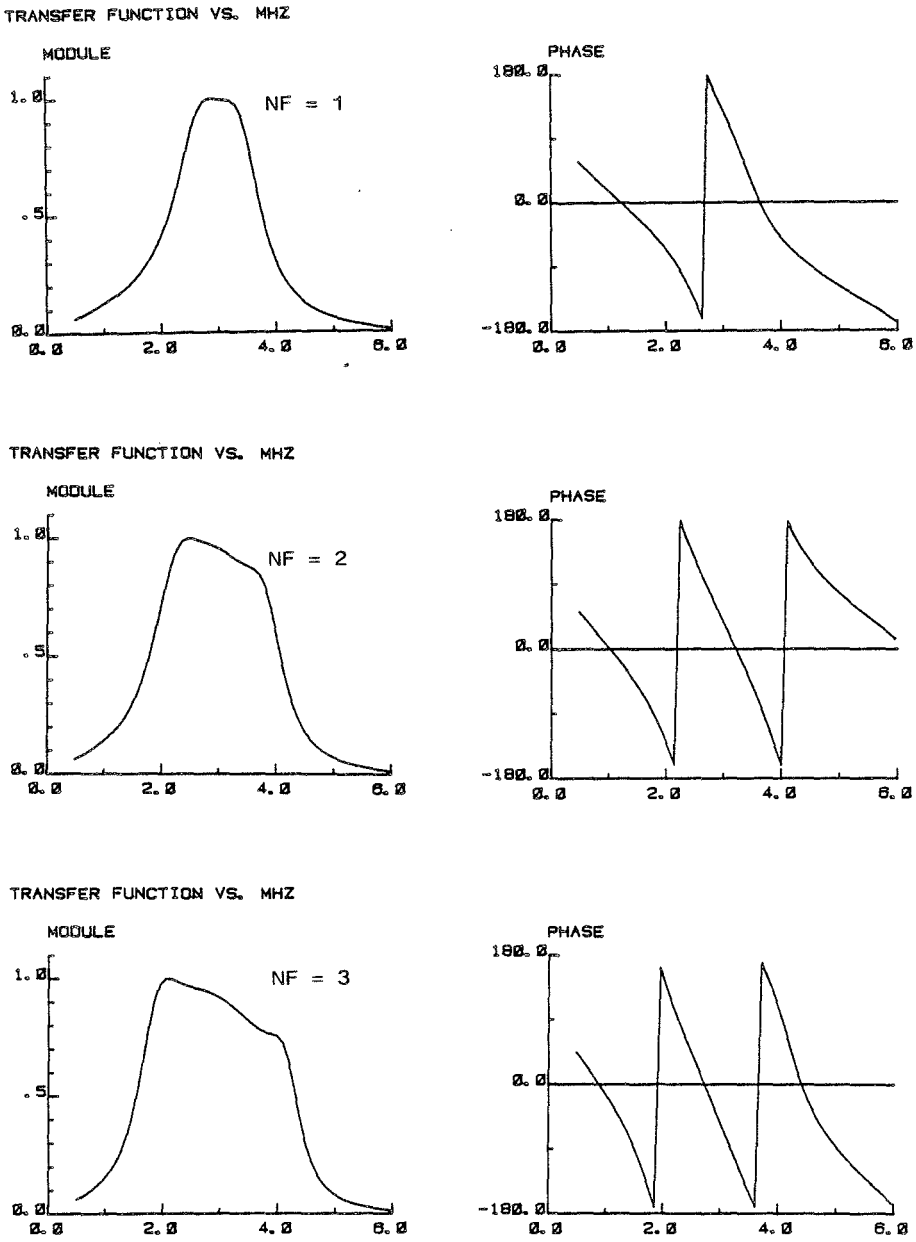

Fig. 3.8. Transfer functions for a PZ27 element with NF=1, 2 and 3 matching layers. The disc diameter is 12.7 mm and the centre frequency is 3 MHz.

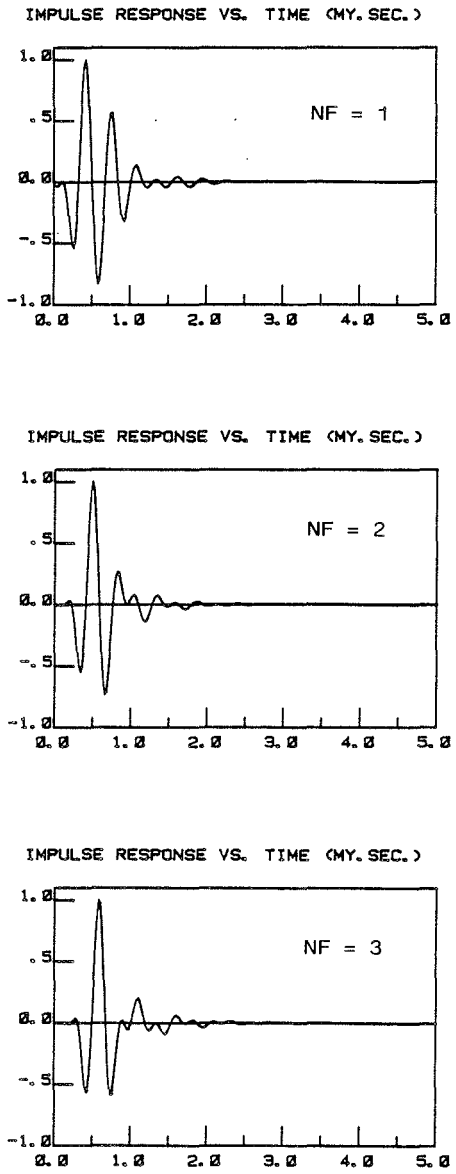

Fig. 3.9. Impulse responses for a PZ27 element with NF=1, 2 and 3 matching layers. The disc diameter is 12.7 mm and the centre frequency is 3 MHz.

An exception is of course the zeros in the original function. A transducer for 3 MHz has zeros at 0 and 6 MHz. If we however are able to make a flat transfer function in the range 0-6 MHz, we will get an impulse response that is close to half a period. In practice, however, such a radical inverse filtering will be limited because of the signal to noise ratio.

Not only the transducer should be taken into account when an inverse filter is designed. If good models for the echo response are available, the influence of the whole measuring system can in principle be eliminated.

4. CALCULATIONS OF TRANSIENT DIFFRACTION PATTERNS

We start by developing methods for calculating the spatial impulse response $h(\vec{r},t)$. The velocity potential $\varphi(\vec{r},t)$ is related to the impulse response through

$$\varphi(\vec{r},t) = v(t)*h(\vec{r},t) \qquad (4.1)$$

where * denotes the convolution and $v(t)$ is the normal component of the velocity at the transducer surface.

The pressure can then be derived from

$$p(\vec{r},t) = \varrho \frac{\partial}{\partial t} \varphi(\vec{r},t) \qquad (4.2)$$

where ϱ is the density of the medium. Thus, the pressure is the time derivative of the convolution of the spatial impulse response and the transducer surface velocity. For presentation of the fields we will in the following use the pressure.

Comparisons of the different apertures will be based on two features. One is the half value beam diameter as a function of depth. The second is the sidelobes and the skirts of the beam profile. We will calculate focal lengths as a result of natural focus, lenses and time delay to the elements of annular arrays.

4.1. Methods for calculations of the spatial impulse response

Before starting on the numerical calculations of the spatial impulse response, we shall try a more intuitive approach. In fig. 4.1 is shown a point, 0, above the surface, S. Points on the surface with the same distance to 0 are circles with centre at the projection of 0 on S. If the surface is excited with a δ-pulse, the points on one circle will contribute at the same time to the potential at 0. The first contribution

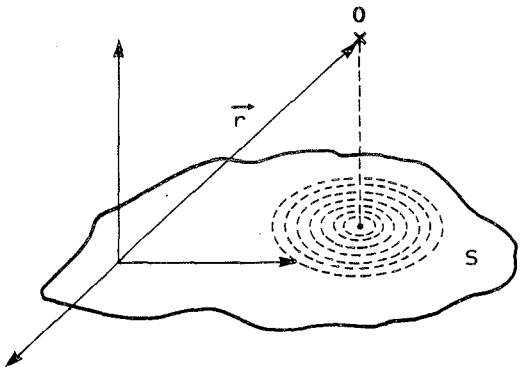

Fig. 4.1. Geometry for the intuitive approach to find the spatial impulse response.

comes from the centre and subsequently circles with increasing diameter will contribute until the edge of the surface is reached.

In the case of a circular aperture, it is easy to find the potential on the axis. As we shall see later, the area that contributes from a plane surface within a given time interval is independent of time. The potential is therefore a rectangular function of time, as shown in Fig. 4.2.a. The time t_0 corresponds to the distance from 0 to S, and t_1 corresponds to the distance from 0 to the edge of the aperture. In a short distance from the aperture the distance between t_0 and t_1 will be largest. In the far field the rectangular function will pass over to a δ-pulse. For focused apertures the far field is moved into the focal plane and the potential function in the focal point will be a δ-pulse as a function of time. In general this is true for all focused apertures. Further away outside focus the contribution from the edge will come first, so that t_0 and t_1 change places in Fig. 4.2.a.

When the point 0 is off-axis, the potential will be constant only until the circles on S at one point pass over the edge of the aperture. Afterwards the potential will decrease monotonically. In Fig. 4.2.b the time t_1 is the minimum

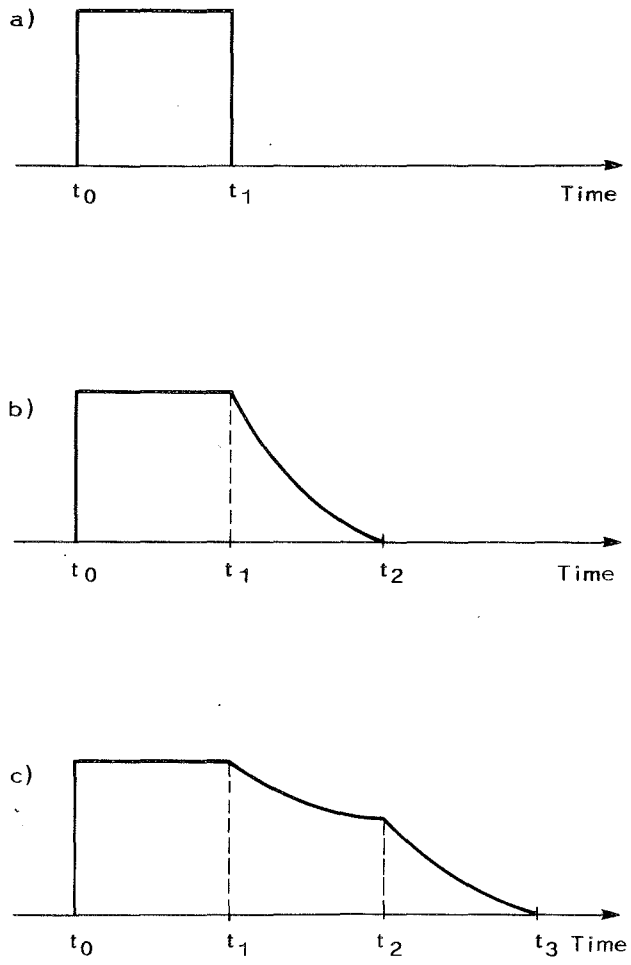

Fig. 4.2. Examples of spatial impulse responses
a) Circular aperture, on-axis
b) Circular aperture, off-axis
c) Rectangular aperture, on- axis

additional delay to the edge of the aperture and the time t_2 is the maximum additional delay to the edge of the circular aperture. For a point on the axis t_1 equals t_2.

For non-circular apertures the potential is more complex. The potential resulting from a uniformly excited rectangular aperture with the observation point on-axis is shown in Fig. 4.2.c. The time t_1 is the minimum additional delay between the centre of the rectangle and the nearest sides in the rectangle; the time t_2 is the delay to the two remaining sides in the rectangle, and the time t_3 is the delay to the four corners. More complex functions will be found if the aperture is nonuniformly excited and focused. Only time consuming computer calculations can give quantitative results.

We shall first develop in detail the spatial impulse response for the circular aperture and show how an analytic solution can be found for this case. A method to find the response from a focused aperture can be found in [6] and will only be listed here. The response from a general aperture can be found through purely numerical integration and will be presented in the end. We shall also see how the response from annular arrays can be found.

4.1.1. Planar circular aperture

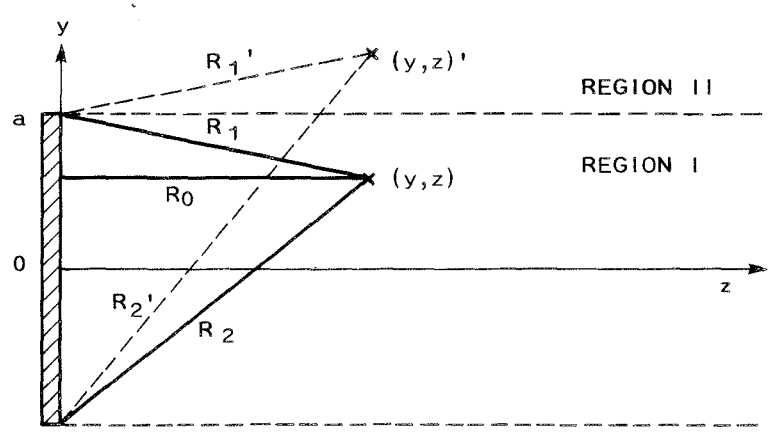

Fig. 4.3. Geometry and definitions for the planar circular aperture.

Fig. 4.3 shows a planar circular aperture with radius a. We divide the space in front of the aperture in regions I and II. Region I is the cylinder with radius a and axis along the z-axis. Region II is the rest of the space. Because of the circular symmetry along the z-axis, we disregard the x-dimension which is equivalent to the y-dimension.

For a point (y,z) in region I there are three characteristic distances. R_0 is the distance to the nearest point on the aperture. R_1 is the distance to the nearest point on the edge of the aperture. And R_2 is the distance to the point on the edge of the aperture furthest away.

We introduce the times

$$t_i = R_i/c, \qquad (4.3)$$

where $i = 0,1,2$ and c is the velocity of the medium. Accordingly

$$t_0 < t_1 < t_2 \ . \qquad (4.4)$$

At the time interval between t_0 and t_1 the contributions come from circles that are completely inside the aperture. We can disregard the limitations due to the finite aperture.

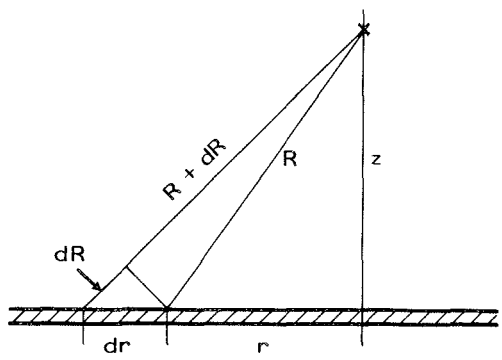

Fig. 4.4. Geometry and definitions for the calculation of the response in the time interval t_0 to t_1 in Region I.

From Fig. 4.4 we will now find the area dS that contributes to the response in the time interval dt. The differential distance is given by

$$dR = c\,dt \tag{4.5}$$

From Fig. 4.4 we can see that the differential radius on the aperture becomes

$$dr = dR \quad \frac{R}{r} \tag{4.6}$$

Thus the differential area becomes

$$dS = 2\pi r\,dr = 2\pi R\,dR \tag{4.7}$$

From Eq. (2.5) we get

$$\begin{aligned} h(\vec{r},t) &= \int_S \frac{1}{2\pi R}\,\delta(t-R/c)\,dS \\ &= c \int_{t_0}^{t_1} \delta(t-R/c)\,d(\frac{R}{c}) \\ &= c \quad \text{for} \quad t_0 \leq t \leq t_1 \end{aligned} \tag{4.8}$$

We have found that the response is a constant in the time interval t_0 to t_1 and equals c.

After the time t_1 only a fraction of the aperture contributes to the acoustic field. This is shown in Fig. 4.5. Here the aperture is seen from the front.

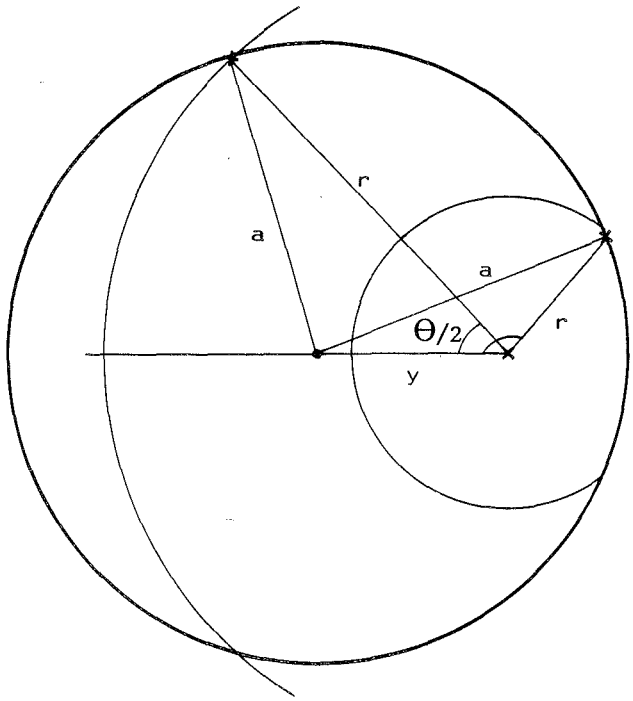

Fig. 4.5. Geometry and definitions for the calculations of the response in the time interval t_1 to t_2 in Region I.

We use the extended Pythagoras law on the triangle in Fig. 4.5.

$$a^2 = r^2 + y^2 - 2ry \cos(\theta/2) \tag{4.9}$$

We also have

$$R^2 = r^2 + z^2 \tag{4.10}$$

This gives

$$\theta = 2 \arccos\left[\frac{R^2 - z^2 + y^2 - a^2}{2y\sqrt{R^2 - z^2}}\right] \tag{4.11}$$

Thus the differential area that contributes within the time interval dt is

$$dS = \theta\, R\, dR$$

$$= 2\, R\, dR \arccos\left[\frac{R^2 - z^2 + y^2 - a^2}{2y\sqrt{R^2 - z^2}}\right] \qquad (4.12)$$

From Eq. (2.5) we get

$$h(r,t) = \int_S \frac{1}{2\pi R}\,\delta(t-R/c)\,dS$$

$$= \frac{c}{\pi}\int_{t_1}^{t_2} \delta(t-R/c)\arccos\left[\frac{R^2 - z^2 + y^2 - a^2}{2y\sqrt{R^2 - z^2}}\right] d\left(\frac{R}{c}\right)$$

$$= \frac{c}{\pi}\arccos\left[\frac{c^2t^2 - z^2 + y^2 - a^2}{2y\sqrt{c^2t^2 - z^2}}\right]$$

$$\text{for} \quad t_1 \leq t \leq t_2 \qquad (4.13)$$

We can see that θ decreases monotonically from 2π to 0 within the time interval from t_1 to t_2. The impulse response will within the same time interval also decrease monotonically from c to 0.

For region II R_0 is not defined. R_1' and R_2' are defined in Fig. 4.3 for the point $(y,z)'$. In Fig. 4.6 the aperture is shown from the front.

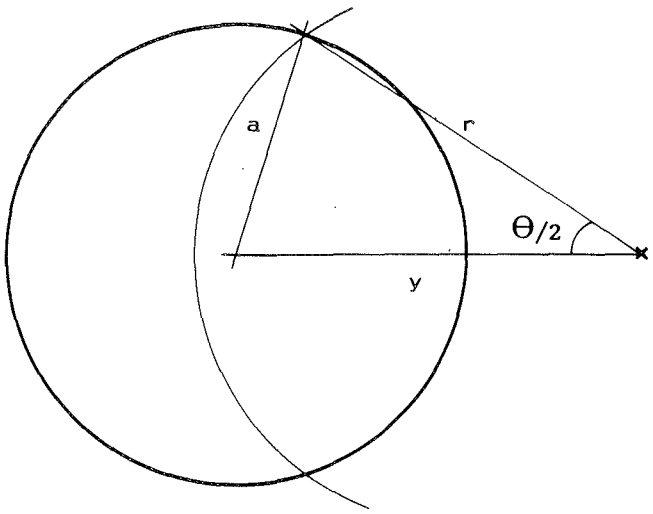

Fig. 4.6. Geometry and definitions for the calculation of the response in Region II.

From Fig. 4.6 we get

$$a^2 = y^2 + r^2 - 2yr \cos(\theta/2) \qquad (4.14)$$

This is the same as in Eq. (4.9).

Thus we obtain

$$h(\vec{r},t) = \frac{c}{\pi} \arccos\left[\frac{c^2t^2 - z^2 + y^2 - a^2}{2y\sqrt{c^2t^2 - z^2}}\right]$$

$$\text{for} \quad t_1 \leq t \leq t_2 \qquad (4.15)$$

The difference from region I is that θ will start from zero, increase to maximum π and decrease again to zero. This gives a single peaked impulse response in region II.

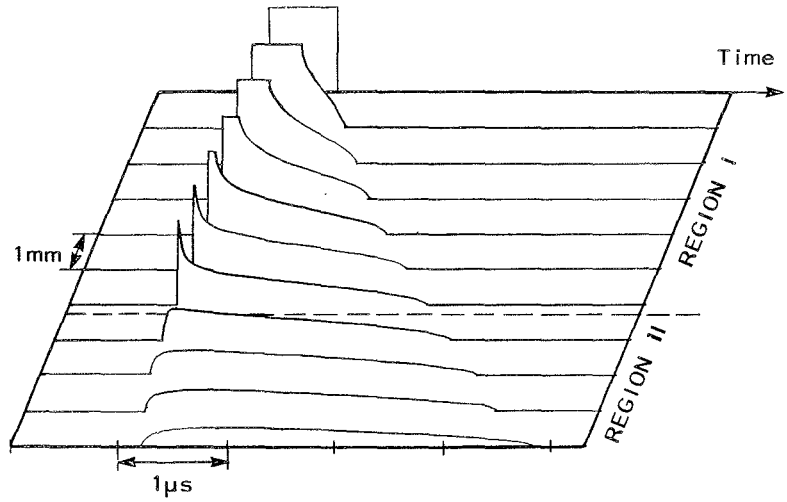

Fig. 4.7. The spatial impulse response from a planar circular aperture as a function of time and radial distance from the acoustic axis in a given distance from the aperture along the axis.

In Fig. 4.7 the spatial impulse response is plotted as a function of time and distance from the axis. The distance from the aperture is 20 mm and the diameter of the aperture is 12.7 mm. We can see that the response is rectangular on the axis. The time derivative is therefore two δ-pulses, the first at time t_0, the second at time $t_1 = t_2$. Near the aperture the distance between t_0 and t_1 is largest, and if the excitation is short enough the pulse will consist of two pulses. The latter is the negative of the former, and is in the literature often called the edge wave. This name is due to the time of arrival which corresponds to the distance to the edge. It is not generated at the edge but as a result of the finite aperture. Off-axis in region I the impulse response has a rectangular beginning, but a monotonically decreasing end. This gives a pressure pulse where the edge waves are only a tail on the main pulse. In region II the response is a smooth function of time and therefore the pressure pulse will be much smaller than in region I.

Increasing the distance from the aperture, the on-axis response will be shorter and for the far field it can be taken as a δ-pulse. For a given wavelength λ the far field distance can be defined as the distance to the point where the response is half a wavelength long. This is

$$z = a^2/\lambda \qquad (4.16)$$

The result is well known for continuous wave transducers [24].

4.1.2. Focused circular aperture

We will now present a method for finding the spatial impulse response for a focused circular aperture, or rather a curved surface. The method that will be presented is developed by Arditi [6], and only the results will be given here.

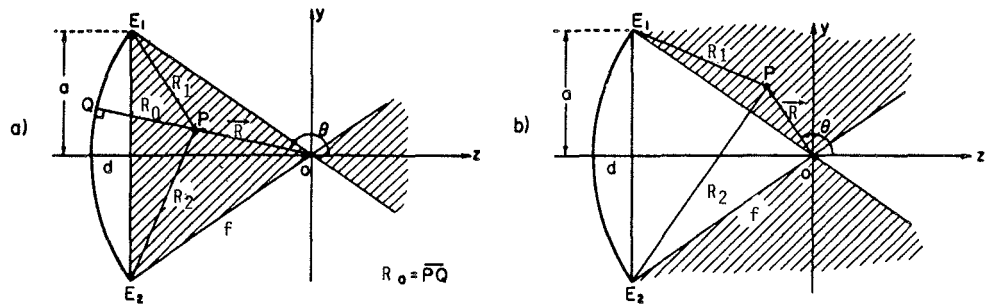

Fig. 4.8. Geometry and definitions for the Arditi method.
a) Region I
b) Region II

We have a circular aperture with radius a and radius of curvature f as shown in Fig. 4.8. Thus f is the focal length of the aperture and we choose the focal point to be the origo. The calculations are done separately for each region as shown in Fig. 4.8 a. and b. Region I can be called the geometrically illuminated region and region II is the rest of

the space in front of the apertur. Assuming circular symmetry it is sufficient to find the solution in the yz-plane.

We also introduce polar coordinates

$$y = R \sin \theta$$
$$z = R \cos \theta \qquad (4.17)$$

It is necessary to find some characteristic distances. The length of the normal from the observation point to the aperture is defined in region I only

$$R_0 = \begin{cases} f - R & \text{for} \quad z < 0 \\ f + R & \text{for} \quad z > 0 \end{cases} \qquad (4.18)$$

The distance from the observation point to the nearest edge E_1 and to the furthest edge E_2 is given by

$$R_1 = \sqrt{(a-y)^2 + (f-d+z)^2} \qquad (4.19)$$

$$R_2 = \sqrt{(a+y)^2 + (f-d+z)^2} \qquad (4.20)$$

Here d is the depth of the aperture

$$d = f(1 - \sqrt{1 - (a/f)^2}) \qquad (4.21)$$

Defining also the times

$$t_i = R_i/c \qquad (4.22)$$

where $i = 0,1,2$ we can find the spatial impulse response from Table 4.1.

$h(\vec{r},t)$ =	Region I		Region II
	$z < 0$	$z > 0$	
0	$t < t_0$	$t_0 < t$	$t < t_1$
$\frac{cf}{R}$	$t_0 < t < t_1$	$t_2 < t < t_0$	-
$\frac{cf}{R\pi} \arccos\left[\frac{\eta(t)}{\sigma(t)}\right]$	$t_1 < t < t_2$	$t_1 < t < t_2$	$t_1 < t < t_2$
0	$t_2 < t$	$t < t_1$	$t_2 < t$

where

$$\eta(t) = \frac{1 - d/f}{\sin\theta} + \frac{1}{\tan\theta}\left[\frac{f^2 + R^2 - c^2t^2}{2Rf}\right]$$

and

$$\sigma(t) = \left[1 - \left[\frac{f^2 + R^2 - c^2t^2}{2Rf}\right]^2\right]^{1/2}$$

Table 4.1. The spatial impulse response for a focused circular aperture after Arditi [6].

The spatial impulse response for three different distances from the aperture are shown in Fig. 4.9. Inside the focal plane the response is very much the same as in Fig. 4.7. At the focal plane the response has no rectangular parts and in the focal point it is a δ-pulse. Outside the focal plane the response is changed so that the rectangular part of the pulse comes at the end.

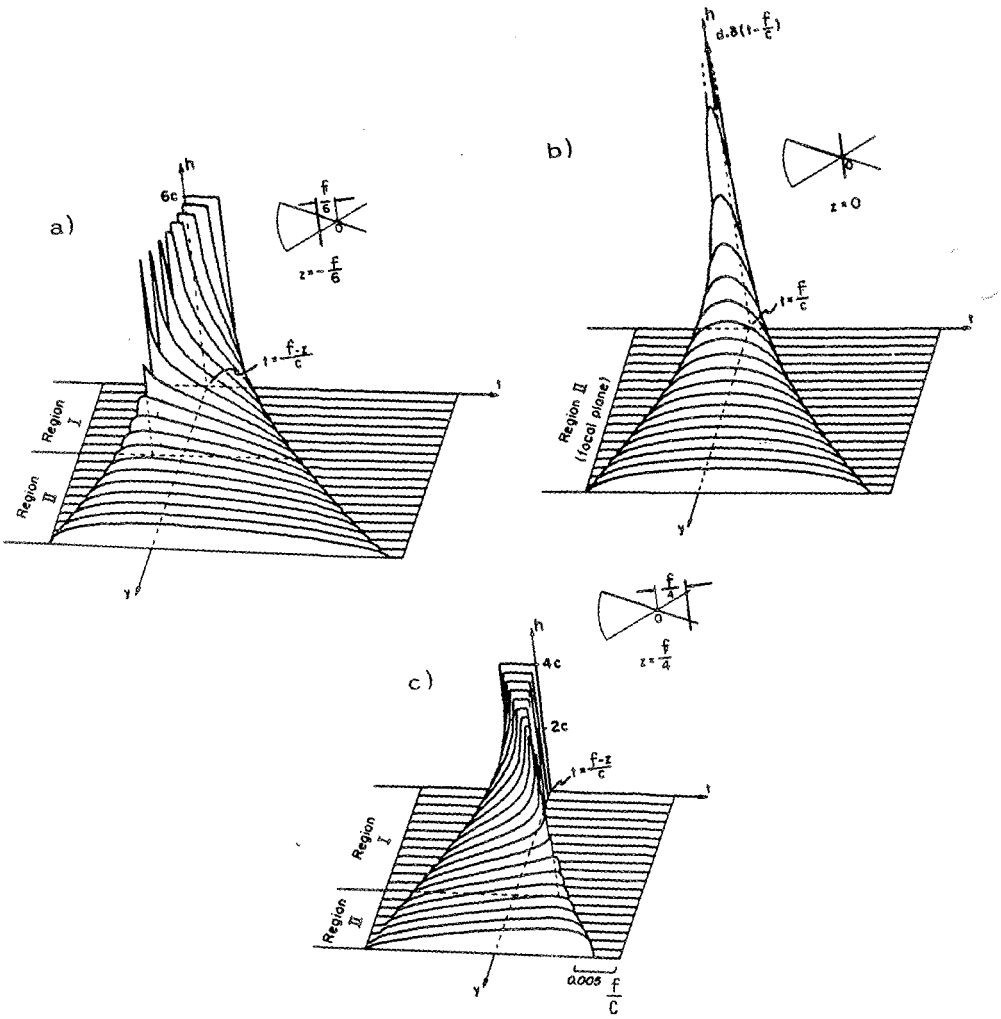

Fig. 4.9. The spatial impulse response as a function of time and distance from the z-axis from a focused circular aperture. The drawings are taken from Arditi [6].

a) z = - f/6
b) z = 0
c) z = f/4

4.1.3. The general aperture

In the more general case with an apodized and focused aperture a direct numerical interpretation of the Huygen principle can be used. The aperture is divided into small elements that are less than half a wavelength. Each element is assumed to radiate uniformly into the infinite half space. In a given observation point in space the response from each element can be found and superimposed. The amplitude is given by the position and apodization of the element. The time of arrival is given by the position and focusing of the element. When the medium is linear, the principle of superposition tells us that the contribution of each element can be summed to give the total response in the observation point. Mathematically this can be expressed:

$$h(r,t) = \sum_i \frac{A_i}{2\pi\,|\vec{r}-\vec{r}_i|}\,\delta\left(t - \frac{|\vec{r}-\vec{r}_i|}{c} - \tau_i\right) \qquad (4.23)$$

Here we have:

- $\vec{r}$: position of the observation point
- $\vec{r}_i$: position of the i'th element
- A_i: excitation of the i'th element
- τ_i: time delay of the i'th element
- c: velocity of the medium

This method can be used for any aperture. The disadvantage is that the calculations of a more complete field are very time consuming. A comparison of this crude numerical approach and the Arditi method is shown in Fig. 4.10. Here we can see the response for an observation point on-axis and 10 mm from the aperture. The calculation by the Arditi method gives a rectangular function. The numerical integration gives a rectangular function with numerical noise, Here the aperture is divided into 18000 elements, which gives a calculation time

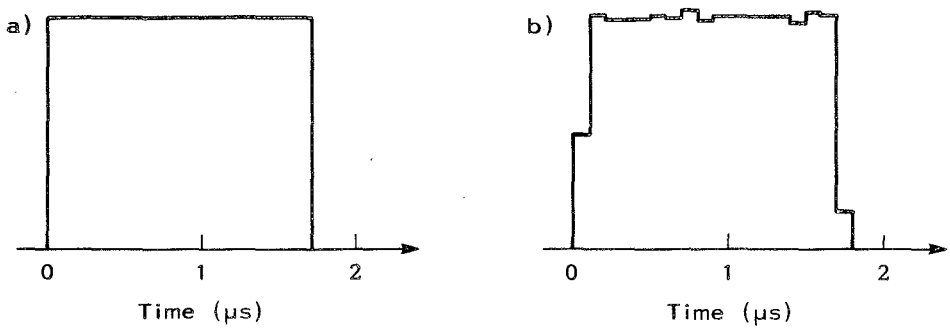

Fig. 4.10. The on-axis response at depth 10. mm from a circular focused aperture with diameter 12.7 mm and a radius of curvature of 75.mm.

a) Arditi method
b) Numerical integration

thirty times longer than for the Arditi method. For a circular focused aperture the Arditi method should be used, but for non-circular and apodised apertures we have to use the numerical integration. The numerical integration is stable, where as the Arditi method give problems in the focal point where the response is a δ-pulse.

4.1.4. Annular arrays

Annular arrays are used for dynamic focusing, which means that one can adjust the focal length of the aperture as a function of time. This possibility is used in echo imaging during reception. A pulse is sent out with a fixed focus, but during reception the focal length is adjusted to match the depth from which the echo has its origin. At first the echoes come from objects close to the transducer and later on from objects further and further away.

The methods developed for circular apertures can easily be extended to annular arrays. The response from a circular element with inner radius a_1 and outer radius a_2 can be found

by calculating the difference between the response from an aperture with radius a_2 and an aperture with radius a_1. Thus for element number n we have

$$h_n(\vec{r},t) = h_{a_2}(\vec{r},t) - h_{a_1}(\vec{r},t) \qquad (4.24)$$

The total response from an annular array is then found by adding the contributions from all elements. By introducing a time delay on each element one can control the focal length.

$$h(\vec{r},t) = \sum_n h_n(\vec{r},t + \Delta t_n) \qquad (4.25)$$

Here Δt_n is the time delay to the n'th element. If the array consists of N elements and the phase front is to be an approximation to a spherical surface with radius of curvature f_2, we can let the outer radius of the n'th element be

$$a_n = \sqrt{\frac{n}{N}}\ a \qquad (4.26)$$

when a is the radius of the whole aperture. This will give an equal area for each element. The time delay between each successive element should be

$$\Delta t = \frac{a^2}{2 f_2 N c} \qquad (4.27)$$

so that the time delay to the n'th element will be

$$\Delta t_n = (n-1)\ \Delta t \qquad (4.28)$$

A discussion of these results has been given by Dietz [25].

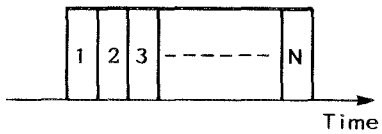

Fig. 4.11. On-axis response from a planar annular array with N elements without time delay.

We have seen that the on-axis response from a circular aperture is a rectangular function. If the aperture consists of annular elements without time delay, the response from each element will arrive in time succession as illustrated in Fig. 4.11. Here element 1 is the centre element and element N the periferal element. If the elements are given a time delay according to Eqs. (4.27 - 28), the responses from each element will coincide at distance f_2 from the aperture. The length of the spatial impulse response at the distance f_2 from a plane aperture of radius a is

$$t_1 - t_0 = \frac{1}{c}\left[\sqrt{f_2^2 + a^2} - f_2\right] \qquad (4.29)$$

when no time delay is used. When N elements are used and given a proper time delay the length of the impulse response will be devided with N. Ideally we want to make the response so short that it will be a δ-pulse for all practical purposes. We can require a response that is shorter than half a period, $\lambda/2c$. This gives us the following requirement for the number of elements if we want to focus at the distance f_2 from the aperture.

$$N > \frac{\sqrt{f_2^2 + a^2} - f_2}{\lambda/2} \qquad (4.30)$$

With λ = 0.5 mm, f_2 = 20 mm and a = 6.35 mm we get N > 3.9. Thus we will need 4 elements to focus at a distance of 20 mm. This estimate is highly simplified. We don't yet know how the field will be off-axis. However, the above approach is illustrational and may serve as a rule of thumb.

If the array in addition to the adjustable focus f_2, has a fixed focus f_1, the total focal length can be found from

$$f^{-1} = f_1^{-1} + f_2^{-2} \qquad (4.31)$$

This is a well known result from thin lens theory in geometrical optics [26].

4.2. Calculated results

In this part of the chapter we will present and discuss some results from the calculations. The computer programs for calculation of transient fields have possibilities for variation of many parameters and parameter combinations. It will therefore not be possible to present a thorough analysis of all the possible parameter set-ups. The selections chosen can be seen in the light of two requirements. The first is to demonstrate the potentials for studying transient fields with the use of these programs. The second is to run the calculations for the transducers of interest to the specific application.

We will limit ourselves to circular apertures. In particular, we will look into focusing with lenses and annular arrays. To study transient behaviour we will excite the medium with three different velocities on the surface of the transducer. These are a continuous wave, a half wavelength pulse and the calculated impulse response from a transducer with one matching layer. The continuous wave is a reference. The half wavelength pulse can be regarded as the ideal echo pulse. While the pulse from a transducer with one matching layer is somewhere in between. Also it is a transducer with one matching layer we will design for the experimental investigations.

A proper presentation of transient fields is not easy since the field is five-dimensional. The field has four independent variables in space and time, and one dependent variable in the field amplitude. It is therefore necessary to present more than one plot for each field pattern. The radial symmetry reduces the space dimension from three to two. Therefore a point in space will be given by the distance from the aperture along the acoustic axis also called the depth and the radial distance from the acoustic axis. At each point in space the pressure or some other field value can be calculated as a function of time. These time functions can be presented directly. But for the study of beam profiles and focusing it

is convenient to use peak detection of pulses and amplitude detection of CW, so that the time dimension is left out. Thus we can present plots for beam profiles at a given distance from the aperture as a function of the distance from the axis. On the basis of the beam profiles we can use half value detection at different distances from the aperture and get a plot that shows the beam diameter as function of the distance from the aperture.

In all the calculations the diameter of the aperture is 12.7 mm and the centre frequency is 3 MHz.

4.2.1. The focused circular disc

We start by presenting the calculations for the most traditional aperture, a circular disc that is focused. The focal length is chosen to be 75 mm.

Figure 4.12 shows calculations of the pressure amplitude when the surface velocity is generated by a continuous signal. Figure 4.12.a shows the half value width of the beam. We can see that the beam is at its narrowest at a distance of 40 mm from the aperture. This is called the beam waist and here the beam diameter is 2.7 mm, while it is 8.5 mm at a distance of 150 mm, and 6.3 mm at a distance of 20 mm. The beam waist is not located at the focal point. This is a diffraction phenomenon and will be discussed in the next subsection.

Figure 4.12.b shows the pressure amplitude in spatial perspective. Also shown in the plot are the 6 dB and 12 dB lines relative to the spatial peak. We observe that the spatial peak occurs at a distance of 50 mm from the aperture.

Figure 4.12.c shows the pressure amplitude across the beam at the distances z equal to 20, 30, 50, 70, 100 and 150 mm from the aperture. We note that the pressure has several peaks for z equal to 20 and 30 mm. At z equal to 50 mm the beam profile has become single-peaked and is the narrowest of those shown.

At the distance z equal to 70 mm we recognize the Bessel function or the Airy's disc. The focal plane is actually at 75 mm, but due to numerical instability the beam profile is shown at 70 mm. The diameter of Airy's disc is given by [26]

$$D = 1.22 \frac{z \lambda}{a} \qquad (4.32)$$

where a is the radius of the aperture and λ is the wavelength. For z equal to 70 mm Eq. (4.31) gives a diameter of 6.7 mm. The first order sidelobe should be 13% of the main lobe [26]. We can see that this is in agreement with the calculations.

For distances greater than the focal length the beam profile gets wider with increasing distance. Continuous waves have zeros both in the near field and in the focal plane. This is due to the fact that in certain locations phase cancellation takes place. This is a result from continuous wave theory [14], but the zeros are difficult to hit in a calcutation.

In the method that is used here the spatial impulse response is convolved with a sinusoid. On-axis the spatial impulse response is a rectangular function. It is then easy to imagine that the result of the convolution is zero when the spatial impulse response is an integer number of periods long. Similarly, the peaks occur where the spatial impulse response is an odd number of half periods long. Somewhat more complicated is the physical explanation of the zeros in the focal plane, but also here the spatial impulse response is such that the result of the convolution is zero.

Figure 4.13 shows the pressure field for the case when the transducer excites the medium with the impulse response from a transducer with one matching layer. Peak detection of the pulse is assumed in Figs. 4.13.a, b and c.

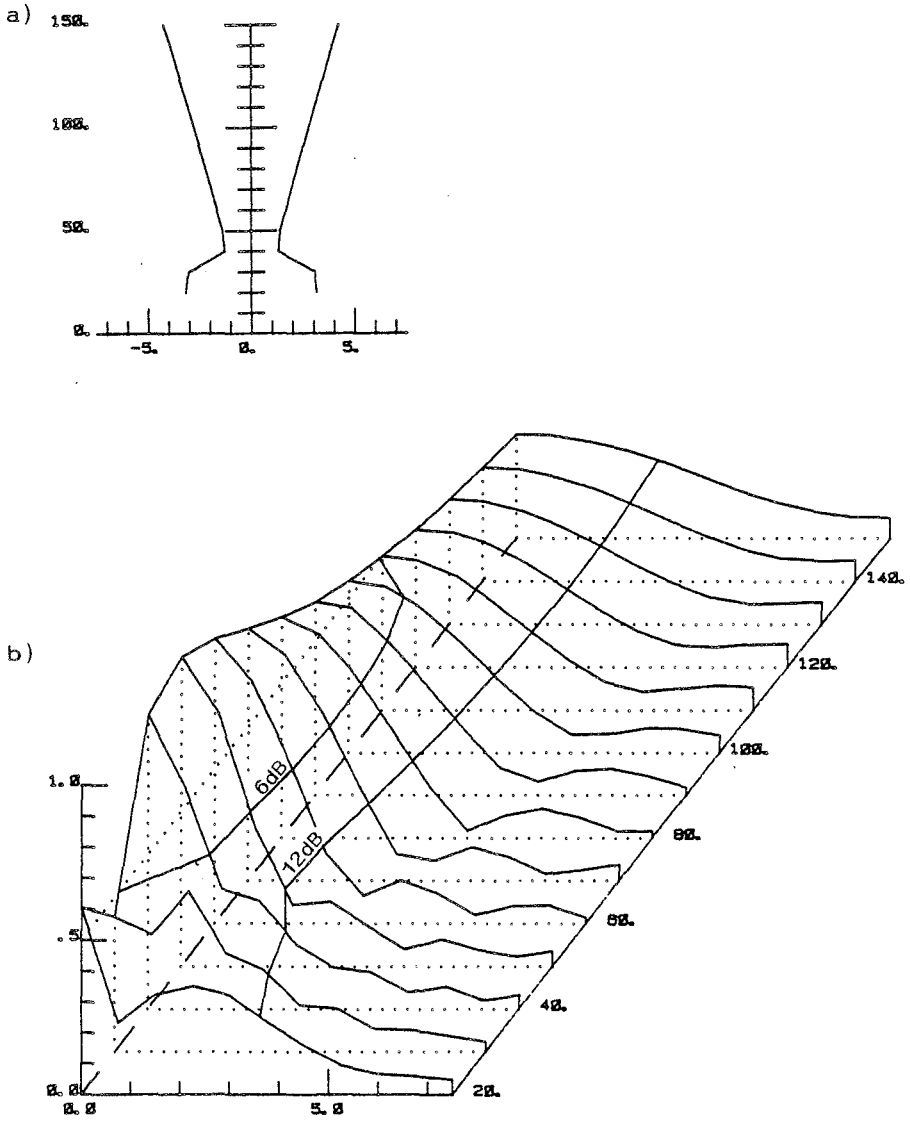

Fig. 4.12. Pressure amplitude from a focused circular disc excited with a continuous wave signal. The aperture diameter is 12.7 mm, the focal length is 75. mm and the frequency is 3 MHz.

a. Beam diameter in mm as a function of distance from the aperture in mm.
b. Beam profile as a function of distance from the aperture and distance from the axis both in mm.

c)

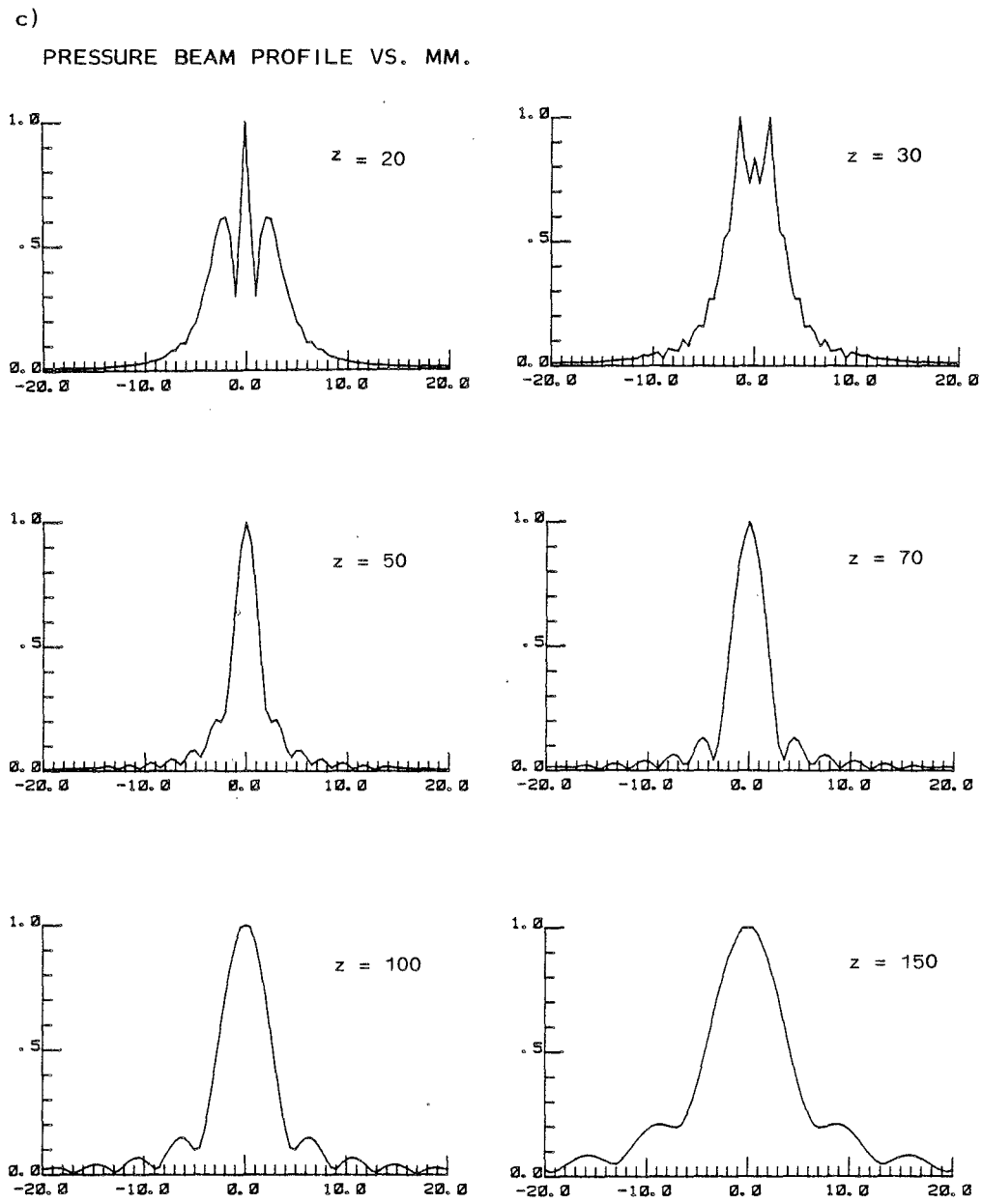

Fig. 4.12.c. Beam profile as a function of distance from the axis at distance z from the aperture both in mm.

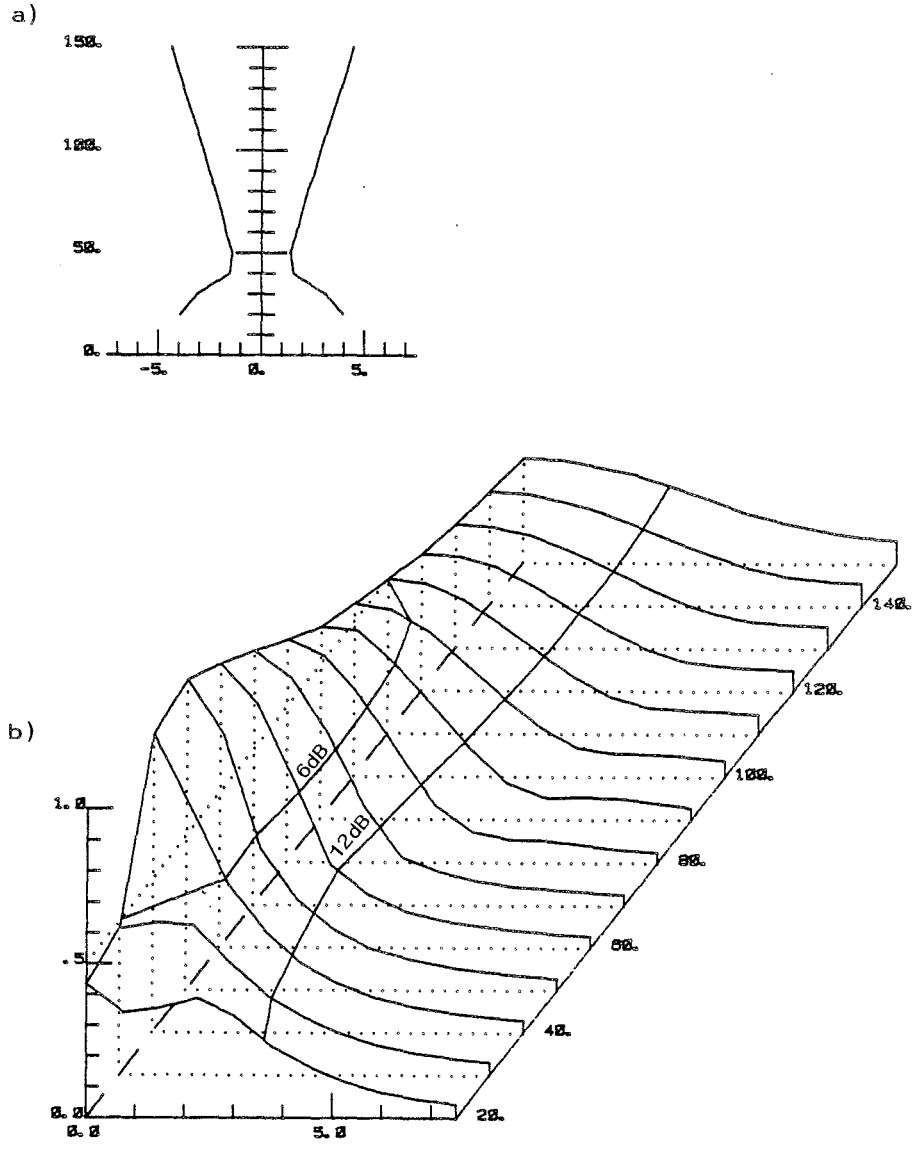

Fig. 4.13. Pressure from a focused circular disc excited with a pulse from a transducer with one matching layer. The aperture diameter is 12.7 mm, the focal length is 75.mm and the centre frequency is 3 MHz.

a. Beam diameter in mm as a function of distance from the aperture in mm.

b. Beam profile as a function of distance from the aperture and distance from the axis both in mm.

c)

PRESSURE BEAM PROFILE VS. MM.

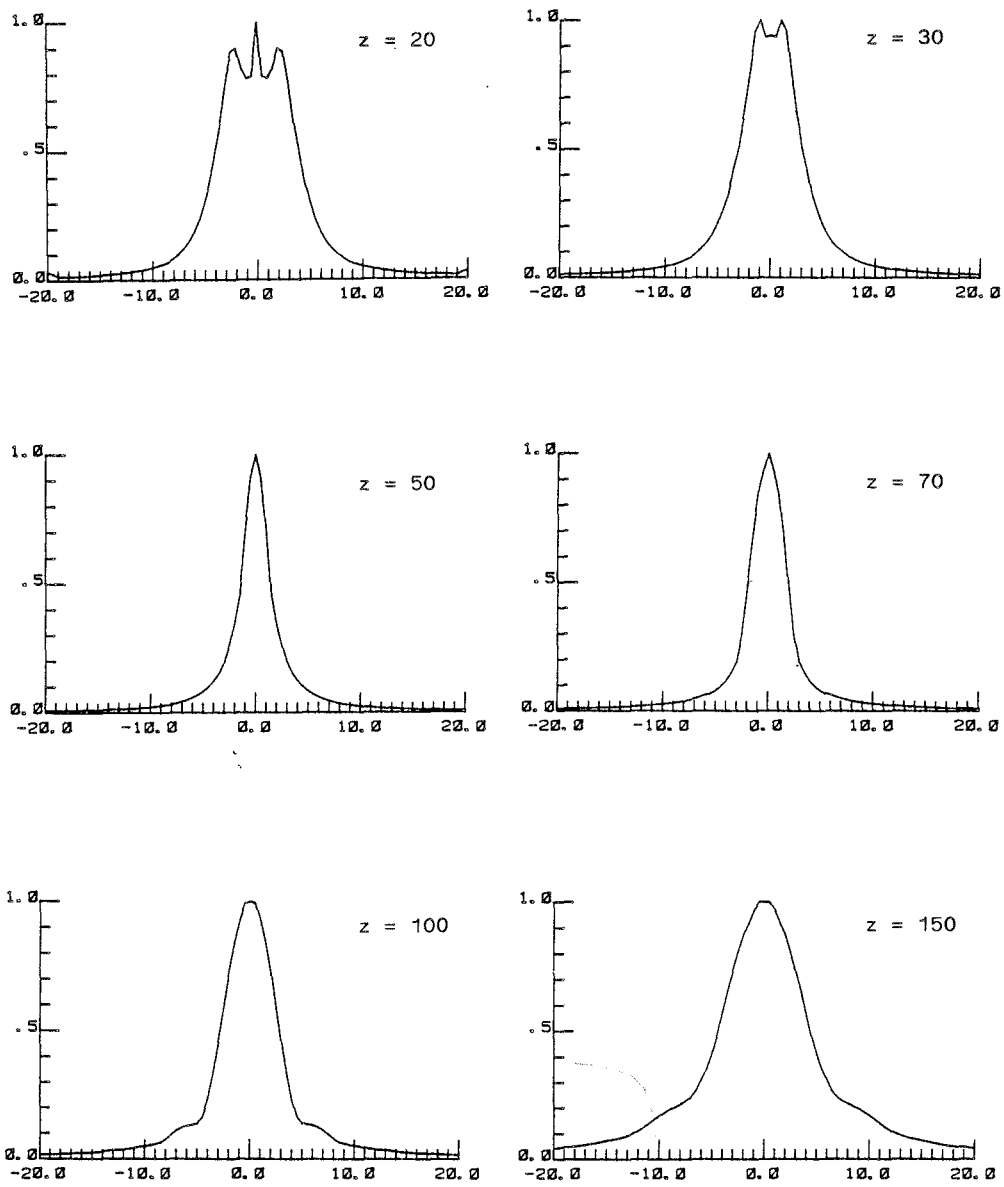

Fig. 4.13.c. Beam profiles as functions of distance from the axis at distance z from the aperture both in mm.

d)

PRESSURE VS. TIME AND RADIAL DISTANCE (MM.)

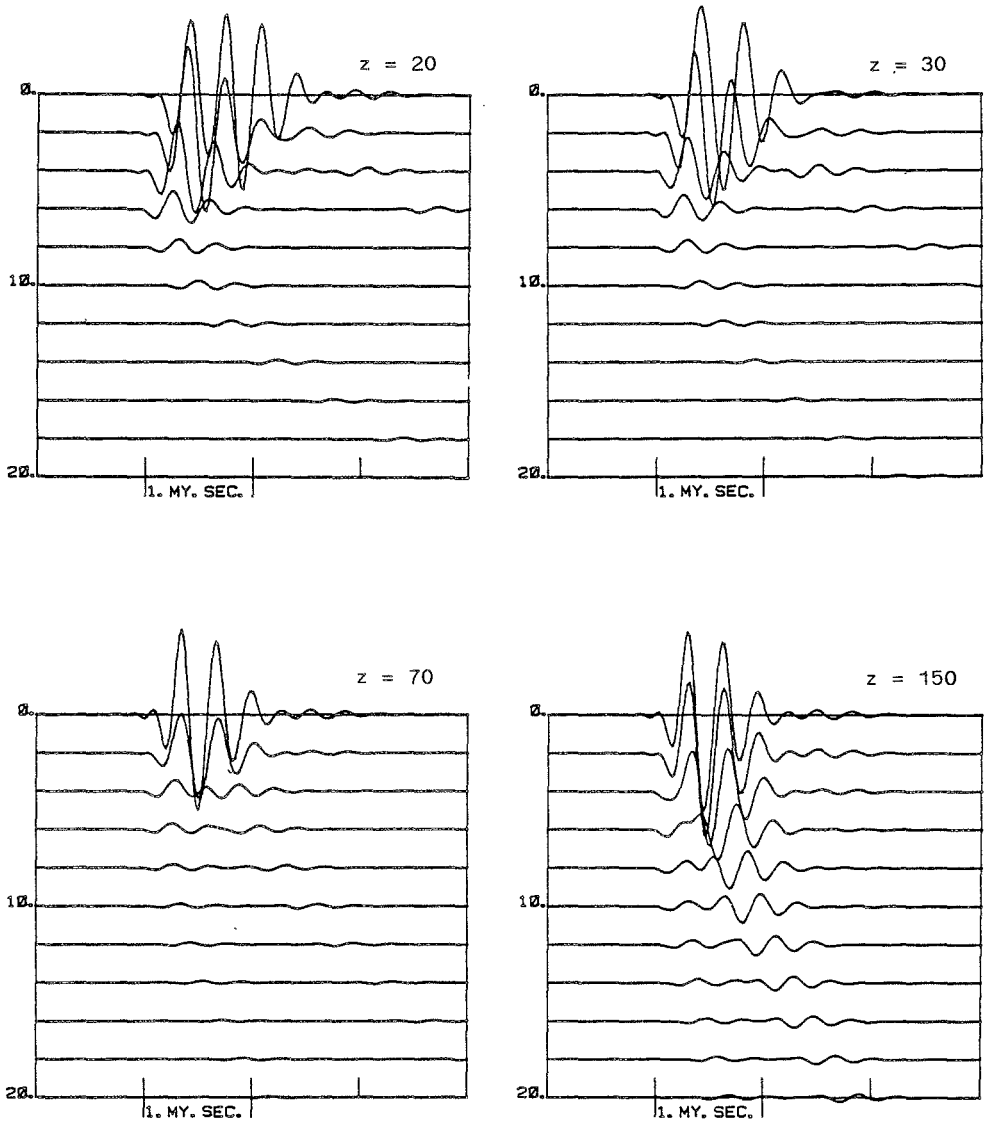

Fig. 4.13.d. Pressure as a function of time and distance from the axis in mm at distance z from the aperture in mm.

Figure 4.13.a shows the half value width of the beam as a function of the distance from the aperture. The beam waist is located at 50 mm distance. There the beam diameter is 2.8 mm, while it is 8.8 mm at 150 mm and 7.9 mm at 20 mm.

Figure 4.13.b shows the beam in perspective in space. The spatial peak is at a distance 50 mm from the aperture.

Figure 4.13.c shows the beam profiles for the same distances from the aperture as in Fig. 4.12.c. Also in this case the profiles at distances of 20 and 30 mm have several peaks, but the variation is much less in the latter case. For z equal to 50 and 70 mm, we note that the profiles decrease monotonically with the distance from the axis. No sidelobes, only skirts can be observed. Also at distances of 100 and 150 mm we can see that the sidelobes are less separated from the main lobe than they were with CW excitation. The calculation shows that transient fields do not form zeros in the fields. This can be understood when we keep in mind that peak detection has been performed on two transient functions that have been convolved. It is difficult to imagine two transient functions giving zero after such a processing.

Figure 4.13.d shows the pressure as a function of time and distance from the axis at distances z equal to 20, 30, 70 and 150 mm from the aperture. These plots show that the temporal peaks occur at different times at different distances from the axis. The pulses at different locations are different in shape. For all practical purposes the on-axis pulse is the same from z equal to 30 mm and further away, while for z equal to 20 mm the pulse is longer. This is due to the influence of the length of the spatial impulse response so close to the aperture. We also note that for all z the pulse gets longer the further away from the axis they are.

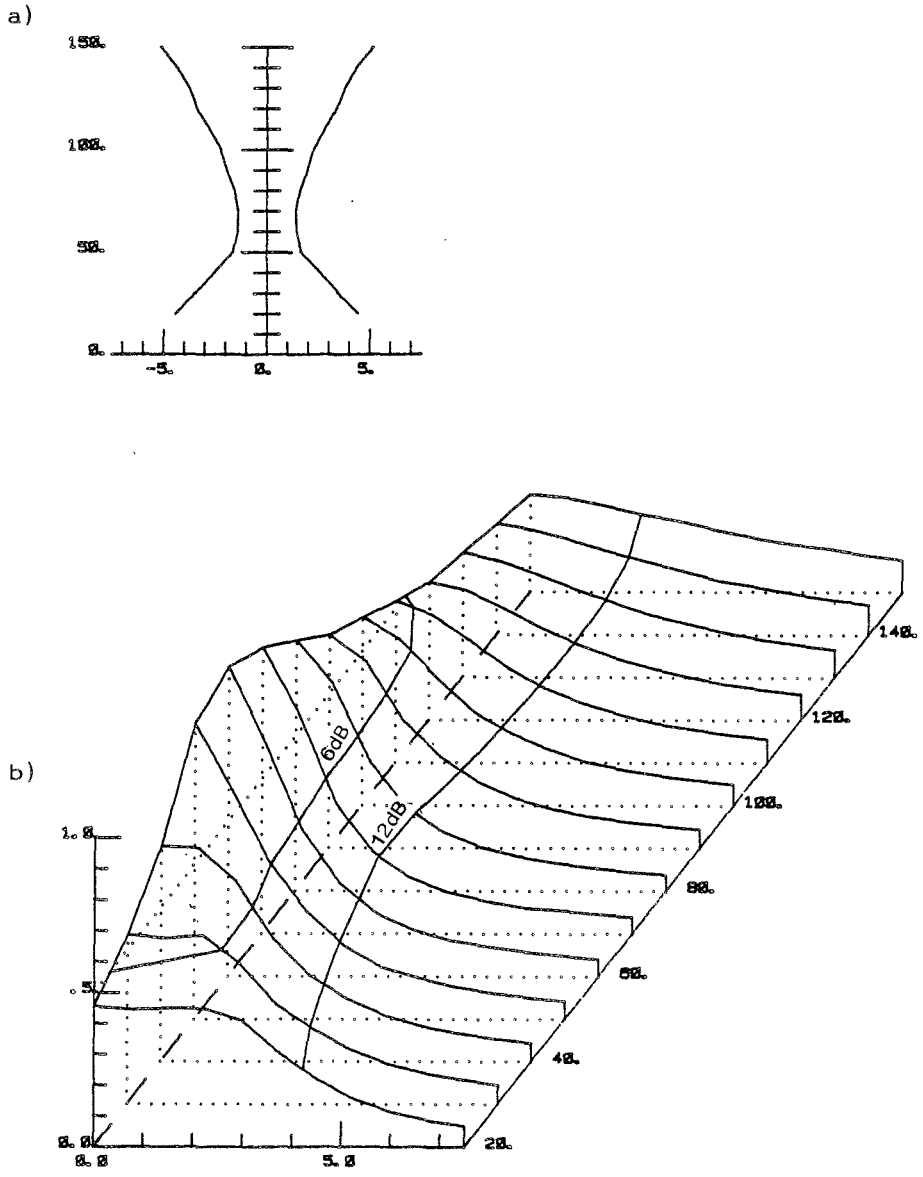

Fig. 4.14. Pressure from a focused circular disc exciting the medium with a half period pulse. The aperture diameter is 12.7 mm, the focal length is 75. mm and the centre

a. Beam diameter in mm as a function of distance from the aperture in mm.

b. Beam profile as a function of distance from the aperture and distance from the axis both in mm.

c)

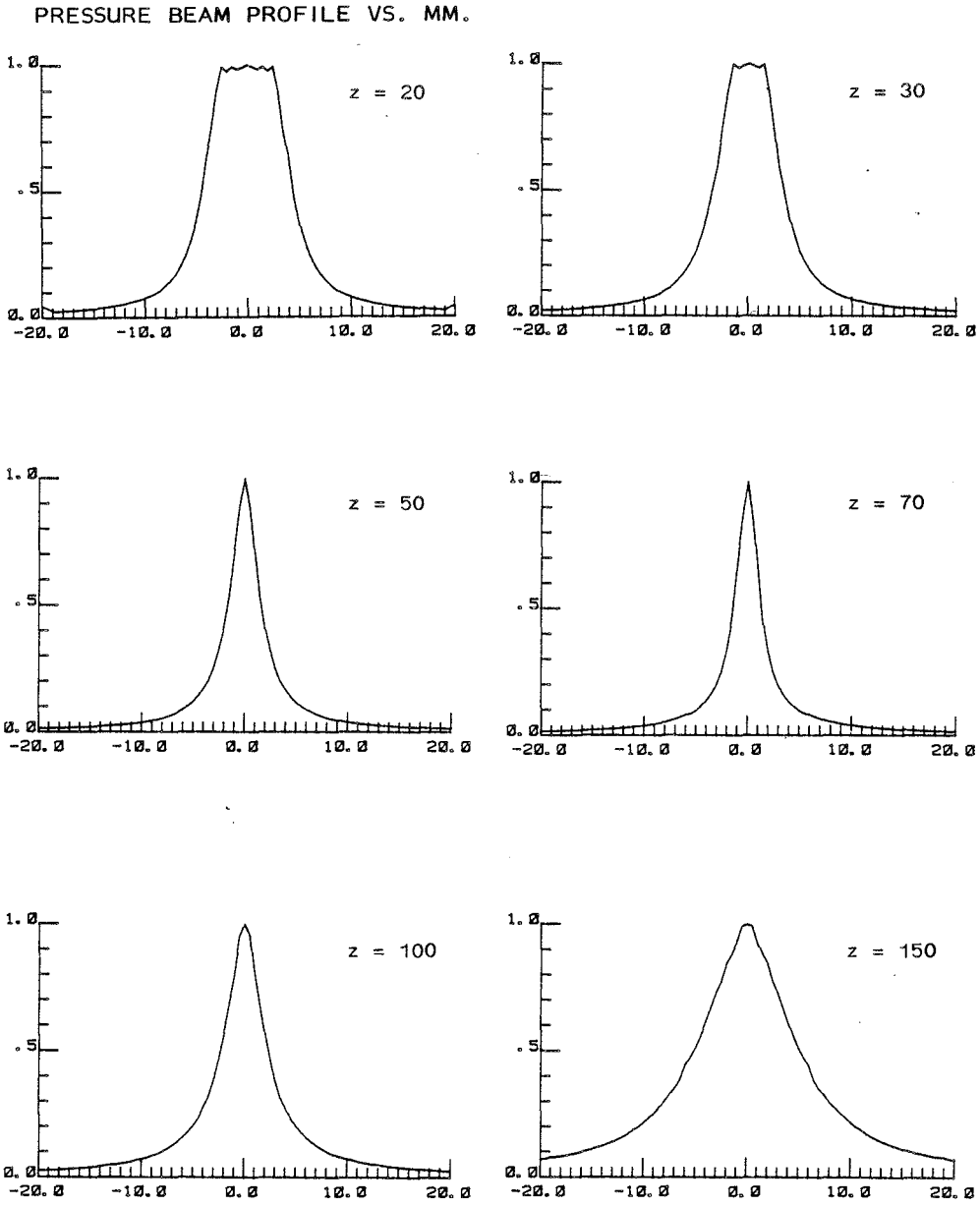

Fig. 4.14.c Beam profiles as a function of distance from the axis in mm at distance z from the aperture in mm.

d)

PRESSURE VS. TIME AND RADIAL DISTANCE (MM.)

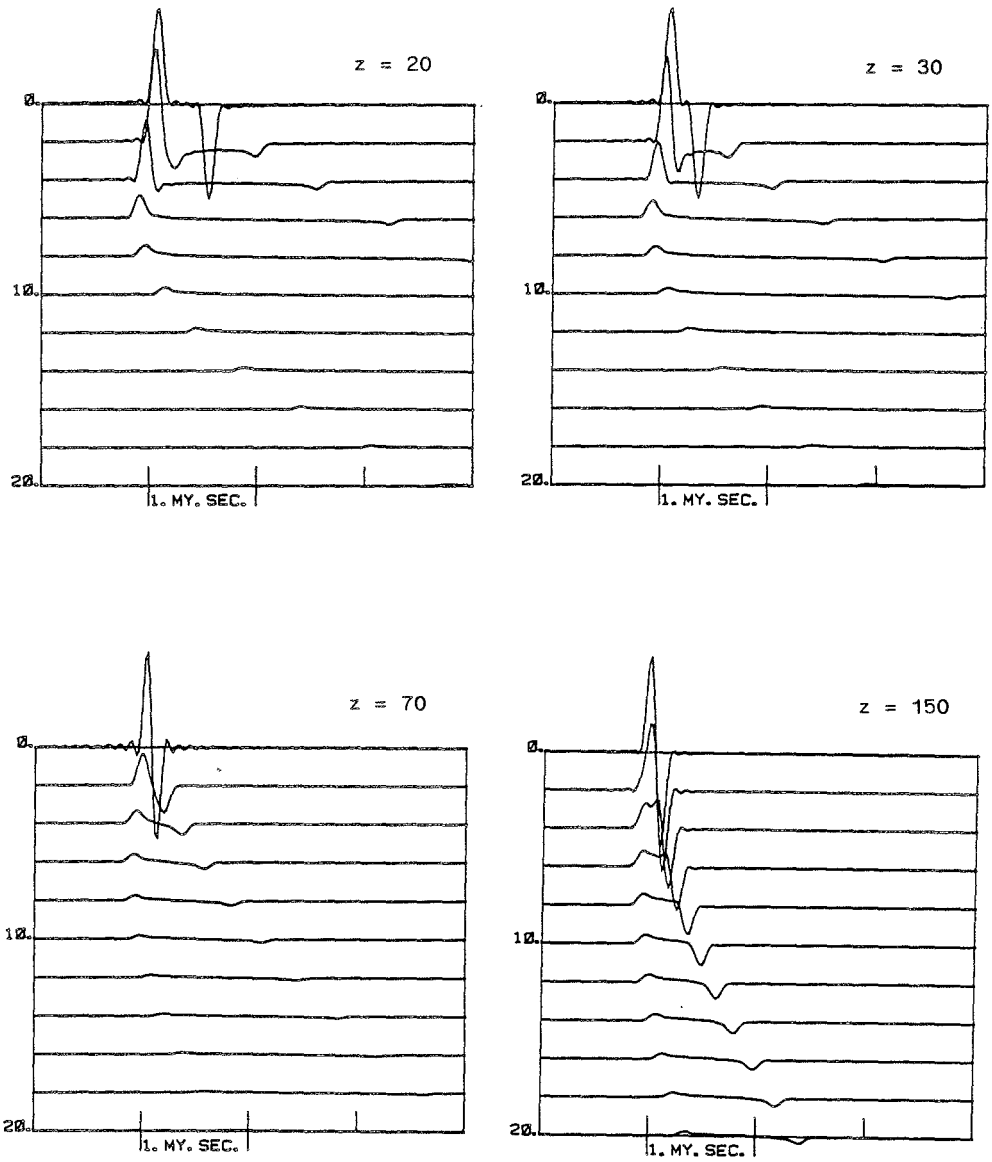

Fig. 4.14.d Pressure as a function of time and distance from the axis in mm at the distance z from the aperture in mm.

In Fig. 4.14 the medium is excited with a pulse that is half a period long. Figure 4.14.a shows the half value beam diameter. The beamwaist is located at depth z equal to 70 mm, where the diameter is 2.8 mm. At z equal to 20 mm the diameter is 8.8 mm and at 150 mm it is 10.3 mm.

Figure 4.14.b shows the beam in perspective in space and we can see that the spatial peak is located at a depth of 60 mm.

Figure 4.14.c shows the beam profiles when peak detection is used. We can see that the beam profiles at z equal to 20 and 30 mm are essentially flat at the top. The sidelobes have disappeared completely and the profiles decrease monotonically at all distances from the aperture.

In Fig. 4.14.d the pulses are shown as functions of time and distance from the axis at the same distances from the aperture as in Fig. 4.13.d. On the axis at z equal to 20 mm we can see how the length of the spatial impulse response influences the pressure pulse. Arriving first is a positive pulse and then a negative pulse due to the beginning and the end of the spatial impulse response. The negative pulse is the one that previously was refered to as the edge wave. Further away from the aperture, the length of the spatial impulse response decreases, and in the focal point it is a δ-pulse. Here the pressure pulse is the time derivative of the half period. Also at z equal to 150 mm we can see that the spatial impulse response is essentially a δ-pulse. The length of the off-axis pressure pulse increases with distance from the axis. Some ripples can be observed in the neighbourhood of the strongest pulses. This is a numerical error due to the truncation of the storing arrays in the computer and is of no physical significance.

A well known method to reduce sidelobes is apodization. In Fig. 4.15 it is shown how apodization with a cosine square function works on the beam profile at a distance 150 mm from the aperture. Figs. 4.15.a and b show the beam profile for a continuous wave without and with apodization.

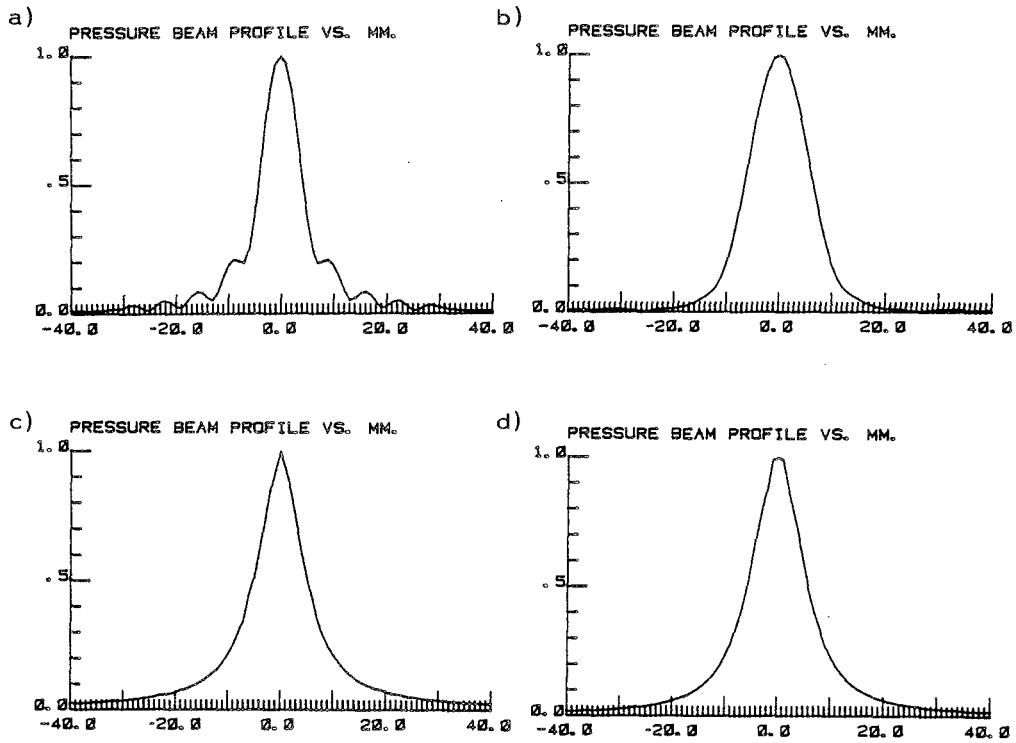

Fig. 4.15. Beam profiles at distance 150 mm from the aperture. The aperture diameter is 12.7 mm, the focal length is 75. mm and the centre frequency is 3 MHz.

a) Continuous wave without apodization
b) Continuous wave with apodization
c) Transient pulse without apodization
d) Transient pulse with apodization.

As expected, the sidelobes are significantly reduced and the beam diameter increased. The interesting point is, however, the influence of apodization on transient fields. Fig. 4.15 c and d show the beam profiles for the case where the aperture excites the medium with a half period pulse with and without apodization. We can see that the influence of the apodization is less here, even if the skirts are reduced and the beam diameter is increased when apodization is used.

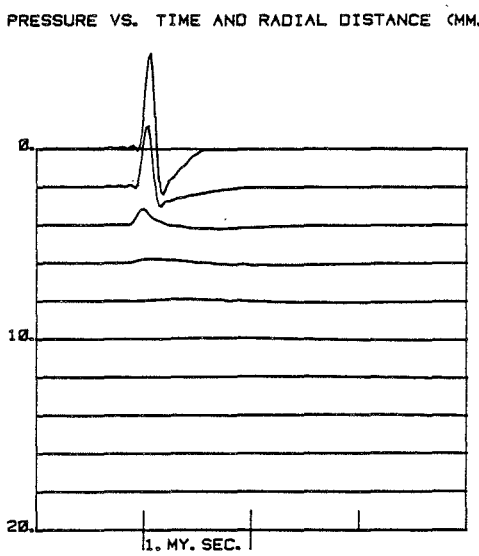

Fig. 4.16. Pressure as a function of time and distance from the axis in mm at distance 20 mm from the apodized aperture which excites the medium with a half period pulse. The aperture diameter is 12.7 mm, the focal length is 75.mm and the centre frequency is 3 MHz.

Figure 4.16 shows the pulse as a function of time and distance from the axis at a distance 20 mm from the apodized aperture in the transient case. Relative to Fig. 4.14 d we can see that the apodization has primarily changed the edge wave. The influence on a peak detected beam profile is therefore small. Thus for transient fields apodization can be used to reduce edge waves more than sidelobes.

4.2.2. The planar disc and the natural focus

One of the most important results of the previous subsection was to find that the beam waist occurs at different distances from the aperture depending on the exciting pulse. For many practical purposes it is natural to define the beam waist as the focal point. We will do so in this subsection and call the actual focal length the geometrical focal length. In the

previous subsection we had 75 mm as the geometrical focal length. For the CW excitation in Fig. 4.12 the beam waist is at 40 mm. For the pulse from a transducer with one matching layer in Fig. 4.13 the beam waist is at 50 mm. And for the half wavelength pulse in Fig. 4.14 the beam waist is at 70 mm. The shortest pulse gives a focal length in agreement with the geometrical focal length, while the CW excitation gives a focal length that is considerably shorter.

To investigate this focusing effect in more detail we will calculate the fields from a planar disc with the three different excitations of the medium. In Fig. 4.17 the beam is shown as a function of distance from the aperture and beam profiles in perspective in space for the CW excitation. The beam waist is at 80 mm. In Fig. 4.18 the excitation pulse comes from a transducer with one matching layer. The beam waist is at 90 mm. In Fig. 4.19 the medium is excited with half a period and this gives hardly any beam waist at all. We also note that the near field is much smoother for the transient excitations than for the CW excitations. This is a consequence of the fact that the transient excitation case can be taken as an average case of a wide frequency range, thus the rapidly changing fields with frequency are smoothed out.

It is easier to give an explanation of the position of the spatial peak rather than the beam waist. However, we can see from Fig. 4.17 that both the spatial peak and the beam waist are at 80 mm. Using the Fresnel zones [26] it is easy to show that the aperture is exactly the first Fresnel zone at the distance

$$z = a^2/\lambda \qquad (4.33)$$

Here a is the aperture radius and λ the wavelength. With a equal to 12.7 mm and a frequency of 3 MHz we get z equal to 81 mm. At this distance on the axis the field will have a maximum. We can see that the result is in good agreement with Fig. 4.17 where the beam waist is at 80 mm. The resolution in the calculation is 10 mm in the z-direction.

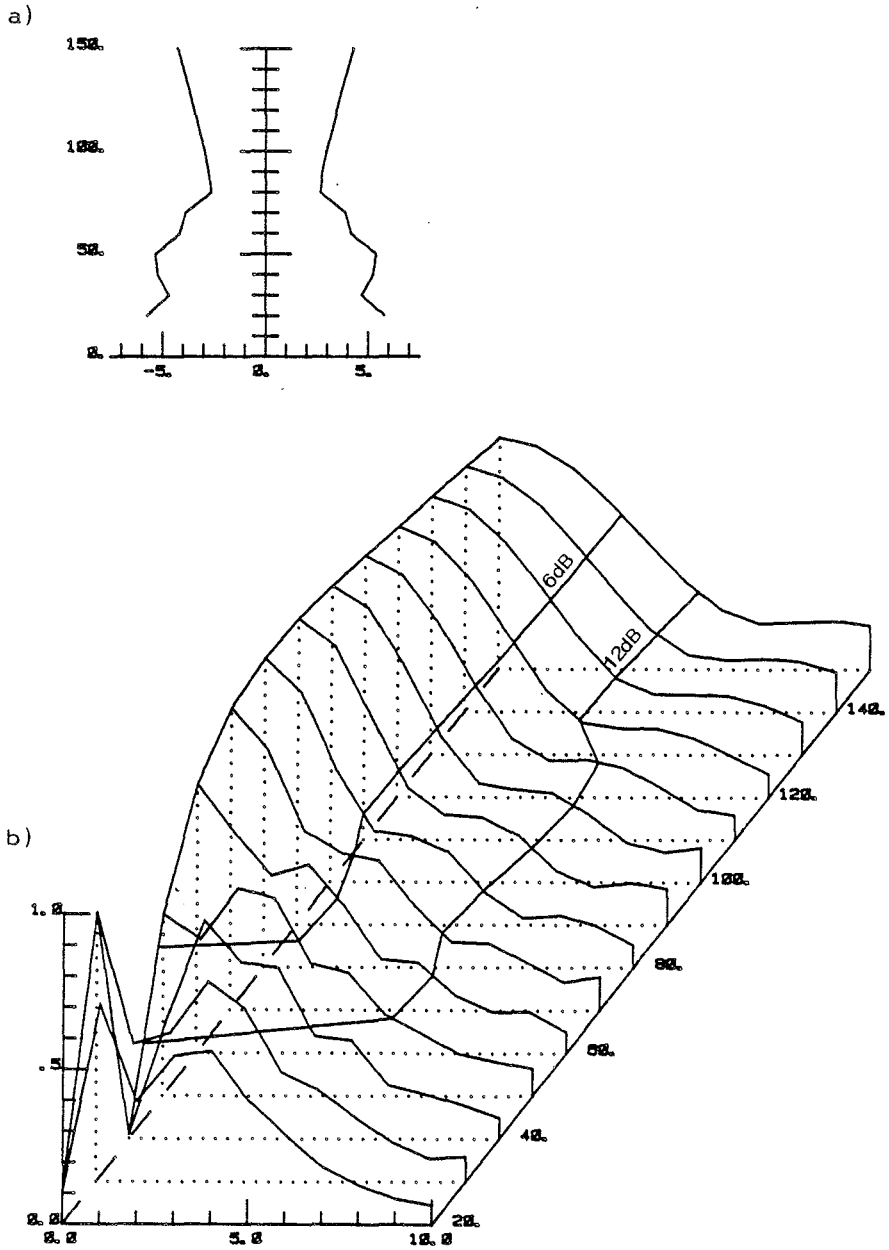

Fig. 4.17. Pressure amplitude with CW excitation from a planar aperture with diameter 12.7 mm and frequency 3 MHz.

a. Beam diameter in mm as a function of depth in mm.

b. Beam profiles in perspective in space in mm.

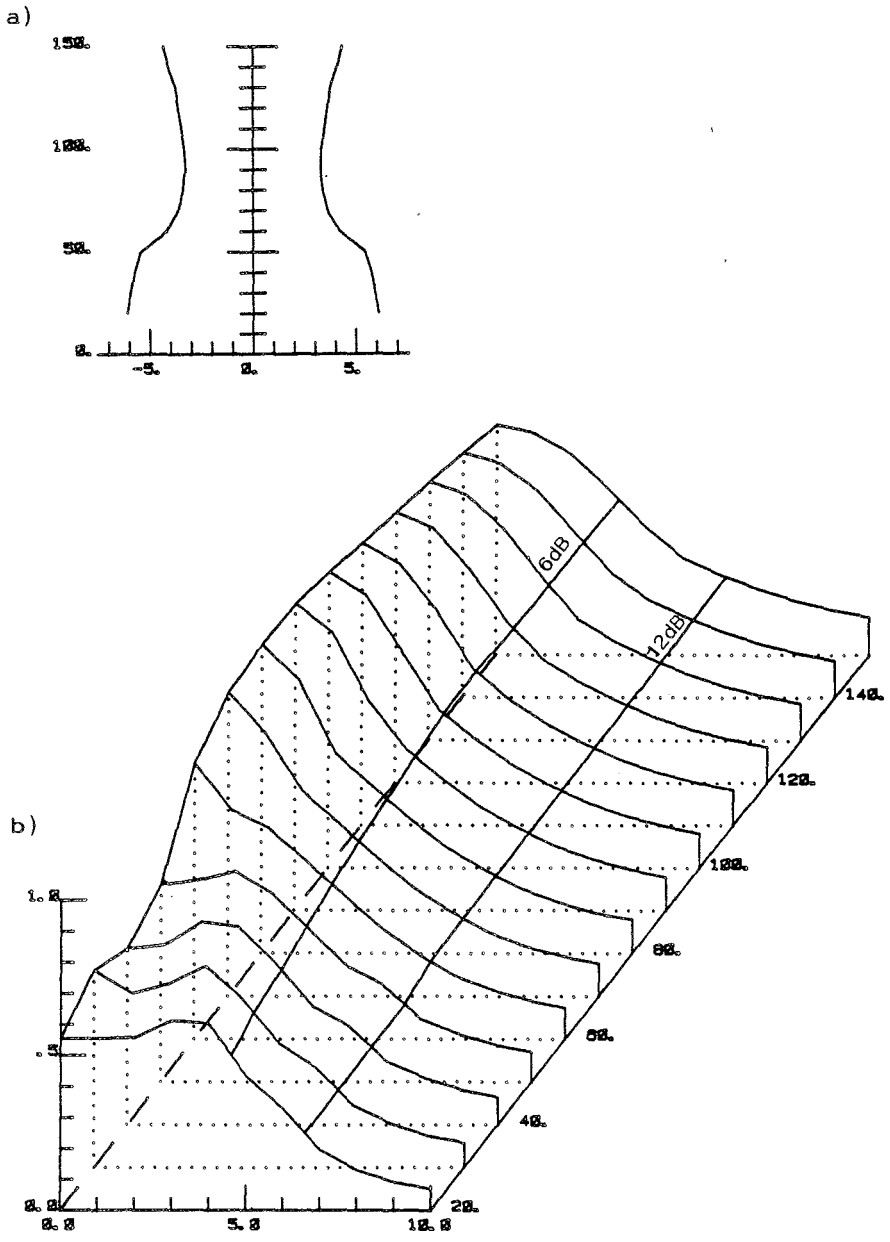

Fig. 4.18. Pressure field with medium pulse excitation from a planar aperture with diameter 12.7 mm and centre frequency 3 MHz.

a. Beam diameter in mm as a function of depth in mm.

b. Beam profiles in perspective in space in mm.

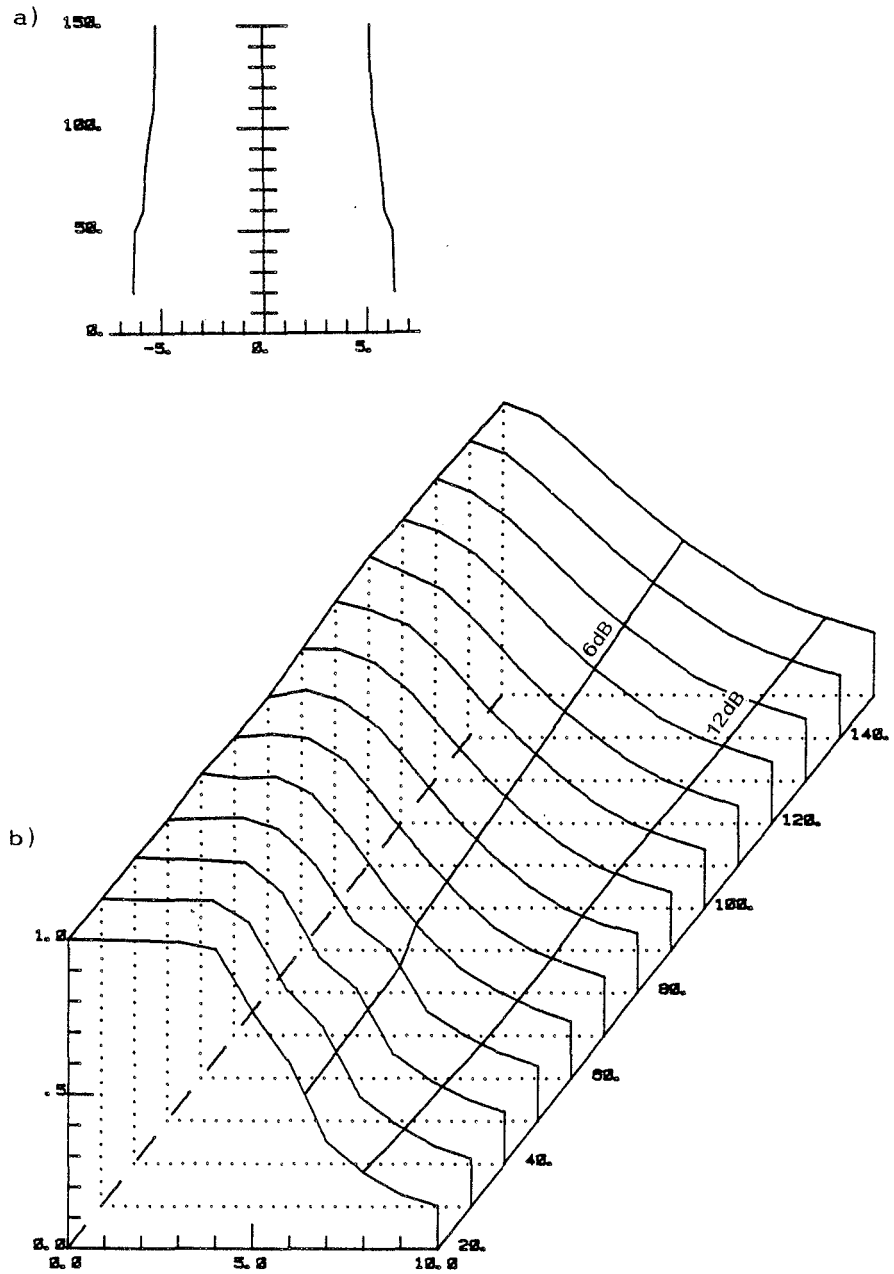

Fig. 4.19. Pressure field with half period excitation from a planar aperture with diameter 12.7 mm and centre frequency 3 MHz.

a. Beam diameter in mm as a function of depth in mm.

b. Beam profiles in perspective in space in mm.

From the theory of the spatial impulse response we know that the on-axis response is a rectangular function. When a continuous wave is convolved with a rectangular function, the result is maximum when the length of the response is an odd number of half periods. From Eq. (4.16) we can find that the spatial impulse response is a half period long at

$$z = a^2/\lambda \tag{4.34}$$

which is the same result as in Eq. (4.33). Thus there are an infinite number of spatial peaks close to the aperture, but the beam profile is single peaked only at the one furthest away from the aperture. It is reasonable to expect the beam waist to be there. We conclude therefore that a natural focusing takes place for CW excitation, and the focal length is

$$f_0 = a^2/\lambda \tag{4.35}$$

For transient excitation the focal length increases as the pulse length decreases.

We know from geometrical optics that two focal lengths in a thin lens can be added inversely [26]:

$$f^{-1} = f_1^{-1} + f_2^{-1} \tag{4.36}$$

Whether this is true or not in this case cannot be proved in a strict sense. This is due to the fact that Eq. (4.36) is based on geometrical theory, while the natural focus is a diffraction phenomenon. But we can verify it for our application. We vary the aperture diameter by 12.7 mm and 15 mm. With a frequency of 3 MHz the natural focal length is 81 mm and 113 mm. We also vary the geometrical focal length by 75 mm and 200 mm. The resulting focal lengths for the four different combinations are found from Eq. (4.36) and are given in Table 4.2.

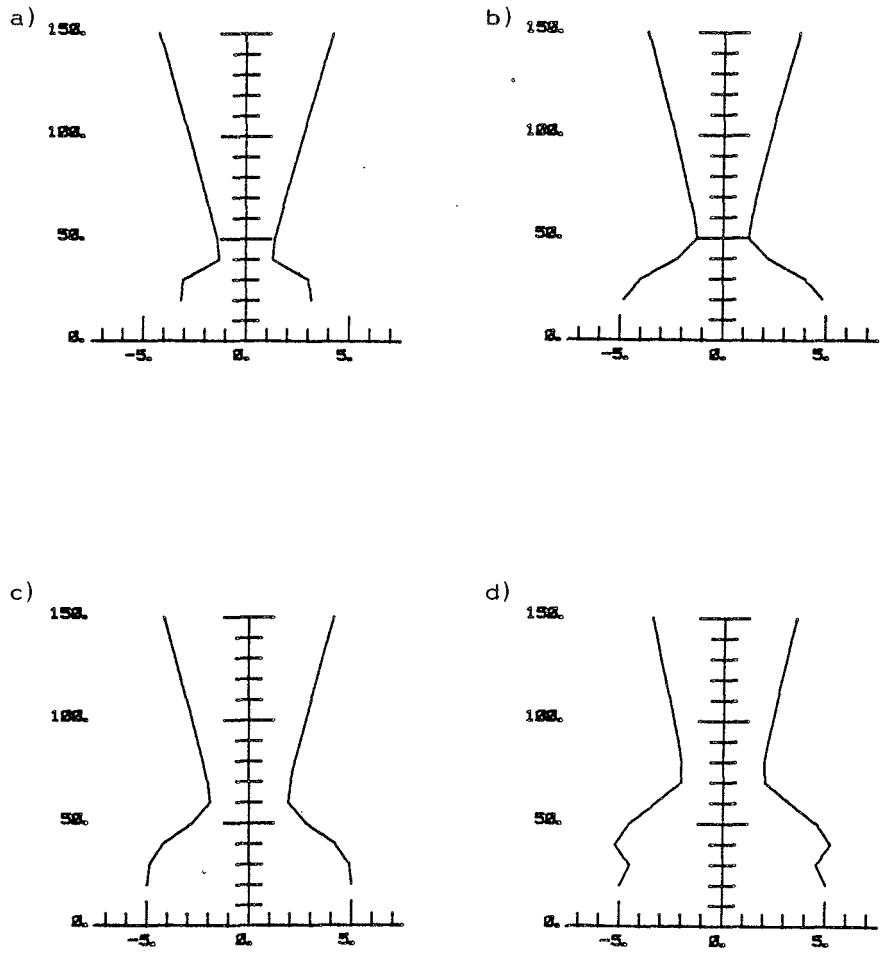

Fig. 4.20. Beam diameter in mm as a function of depth in mm for natural focal length NF and geometrical focal length GF. The aperture diameter is 12.7 mm and the CW excitation has a frequency of 3 MHz.

a. GF = 75 , NF = 81
b. GF = 75 , NF = 113
c. GF = 200, NF = 81
d. GF = 200, NF = 113

Fig.	Geometrical focal length	Natural focal length	Total focal length
a	75	81	39
b	75	113	45
c	200	81	58
d	200	113	72

Table 4.2. Combinations of natural and geometrical focal lengths for Fig. 4.20.

In Fig. 4.20 the calculations are shown for the same four variations of the focal lengths. We can see that the results are in good agreement with Table 4.2 and we conclude that the focal lengths can be added inversely to give a guideline to where the beam waist will be for our transducers.

4.2.3. Annular arrays and dynamic focusing

In this subsection we will analyse the fields of annular arrays. The purpose of annular arrays is to use dynamic focusing in echo imaging. The pulse is transmitted with a fixed focus. During reception the focal length is adjusted so that it equals the depth of the echo at all times. From now on we will use the defination of focal length as it is defined in geometrical optics.

There are two properties that are important to examine in connection with annular arrays. The first is to find out to which extent a finite number of elements is capable of shaping a focus and how many elements that are necessary. The reference is the focus formed by a spherical lens. The second is to find out how much the resolution is improved by using dynamic focusing in reception.

From Eg. (4.30) we estimated the required number of elements to be four. This was based on a simple analysis of the on-axis field and should be regarded as a guideline only. However, we will start with four elements and compare with two and eight elements.

We have seen earlier that the exciting pulse shape influences the field. In this subsection however, we will use the pulse from a transducer with one matching layer.

In Fig. 4.21 are shown plots that are comparable with those of Fig. 4.13. The only difference is that while a lens is used in Fig. 4.13, four elements with a proper time delay are used in Fig. 4.21. The focal length is 75 mm for both. A comparison of the beam diameters as functions of depth gives no significant differences. The skirts of the beam profiles are however different, and the difference is greatest in the near field. The near field pressure varies more across the beam for the four element transducer. But generally speaking the four element transducer performs well. However, it is not a focal length of 75 mm, but rather a focal length of 20 mm that requires four elements according to Eq. (4.30). To decide how many elements that are required, we will use the beam diameter and the beam profile plots.

In Fig. 4.22 the beam diameter is shown as a function of depth for 2, 4 and 8 elements when dynamic focusing is used. The beam is generated by letting the focal length be equal to the depth at all depths. We can see that the beams from 4 and 8 elements are essentially equal. The beam from 2 elements has a larger diameter than the two others in the near field. At a depth of 20 mm the beam diameter for 2 elements is more than twice the beam diameter for 4 and 8 elements.

Fig. 4.23 shows the beam profiles as functions of distance from the axis at the depths z equal to 20 and 30 mm for 2, 4 and 8 elements. The focal length is equal to the depth in all the plots. We can now see more clearly that two elements are

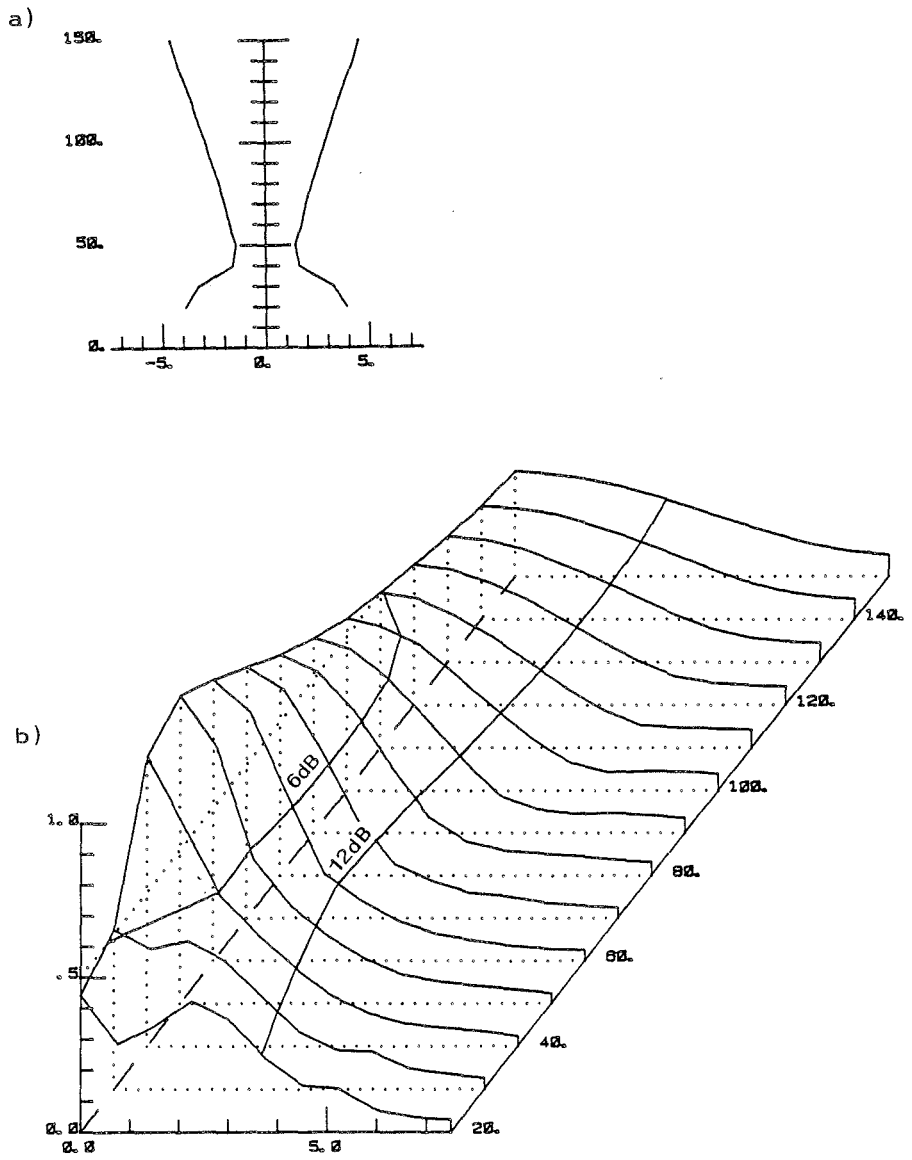

Fig. 4.21. Pressure field with medium pulse excitation from a planar four element annular array with aperture diameter 12.7 mm and centre frequency 3 MHz.

a. Beam diameter in mm as a function of depth in mm.

b. Beam profile in perspective in space in mm.

c)

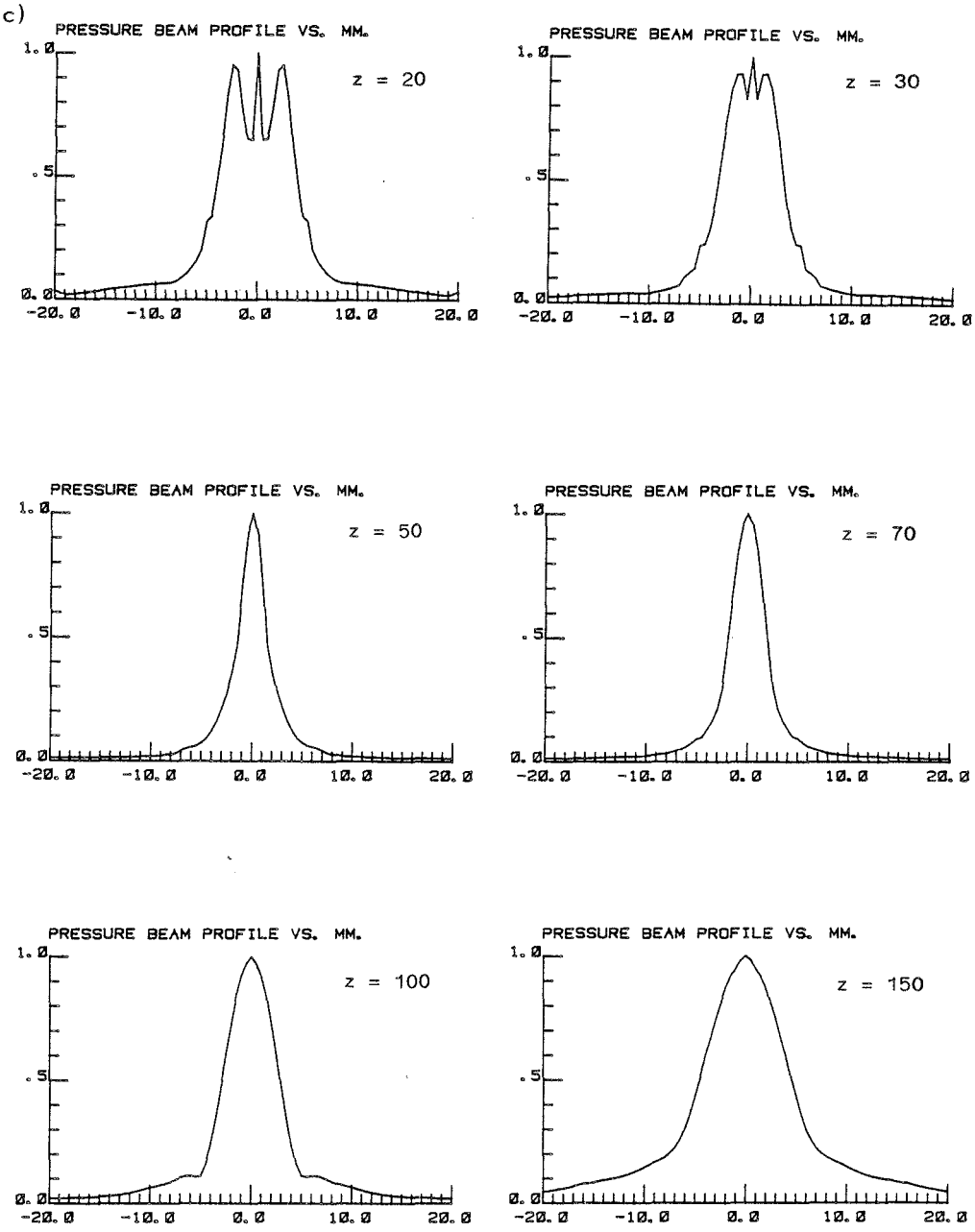

Fig. 4.21.c. Pressure beam profile as a function of distance from the axis at depth z in mm.

too small a number to give a good focus at depths of 20 and 30 mm. Increasing to 4 elements gives a radical improvement of the skirts in addition to the reduction in beam diameter mentioned above. Increasing to 8 elements gives us further improvements relative to 4 elements. However, the important improvements take place when going from 2 to 4 elements. We therefore decide to use 4 elements.

In Fig. 4.24 beam profiles are shown for an annular array with 4 elements when the focal length is set equal to the depth at all the depths. Therefore when 4 elements are used for dynamic focusing, the beam profiles during transmission will be those shown in Fig. 4.21, and during reception those shown in Fig. 4.24.

For comparison of the beam profiles at a given depth we have used a focal length that is equal to the depth. In the previous subsection we have however learned that the beam waist is closer to the aperture than the focal point. It is therefore possible that another choice of focal length can give a better result. This possibility is investigated in Fig. 4.25, where beam diameter plots are shown for a 4 element array with the focal lengths equal to 30, 40, 50 and 75 mm. For f equal to 75 mm we can see that the beam waist is at 50 mm. However, the beam diameter at depth 50 mm is narrower in the case where the focal length is equal to 50 mm. When the focal length is equal to 50 mm, the beam waist is at depth 40 mm. However, the beam diameter at depth 40 mm is narrower in the case where the focal length is equal to 40 mm, and so on. This indicates that the optimum choice of focal length is to let it be equal to the depth where the smallest diameter is desired. This is true in spite of the fact that the beam waist then will be located closer to the aperture.

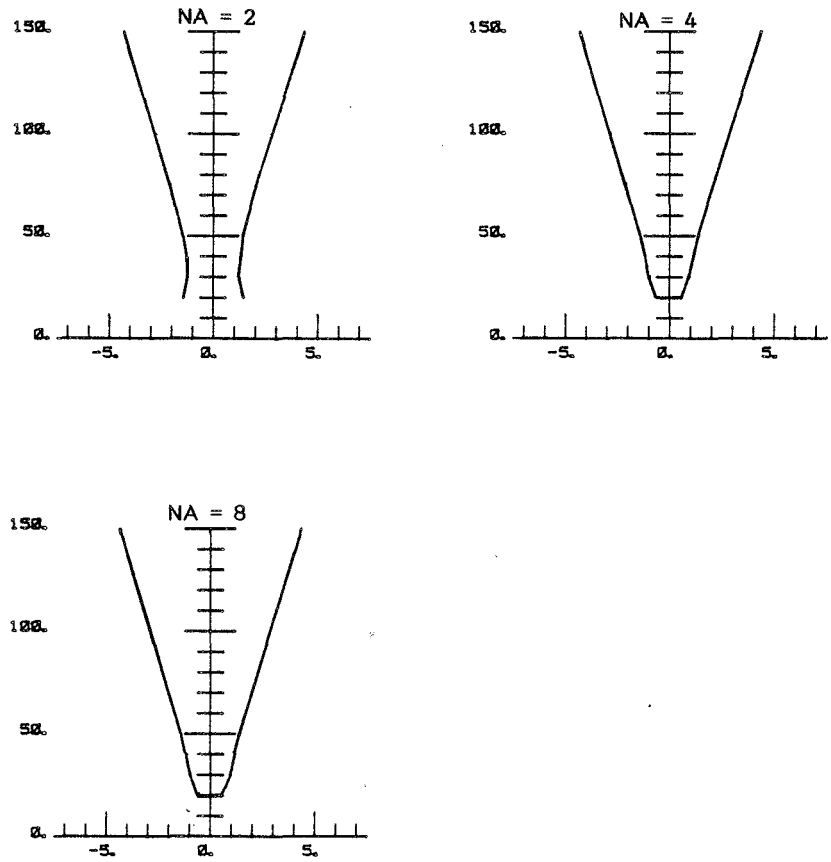

Fig. 4.22. Beam diameter in mm as a function of distance in mm from an aperture with NA elements. The aperture diameter is 12.7 mm. The excitation is the medium pulse with centre frequency 3 MHz.

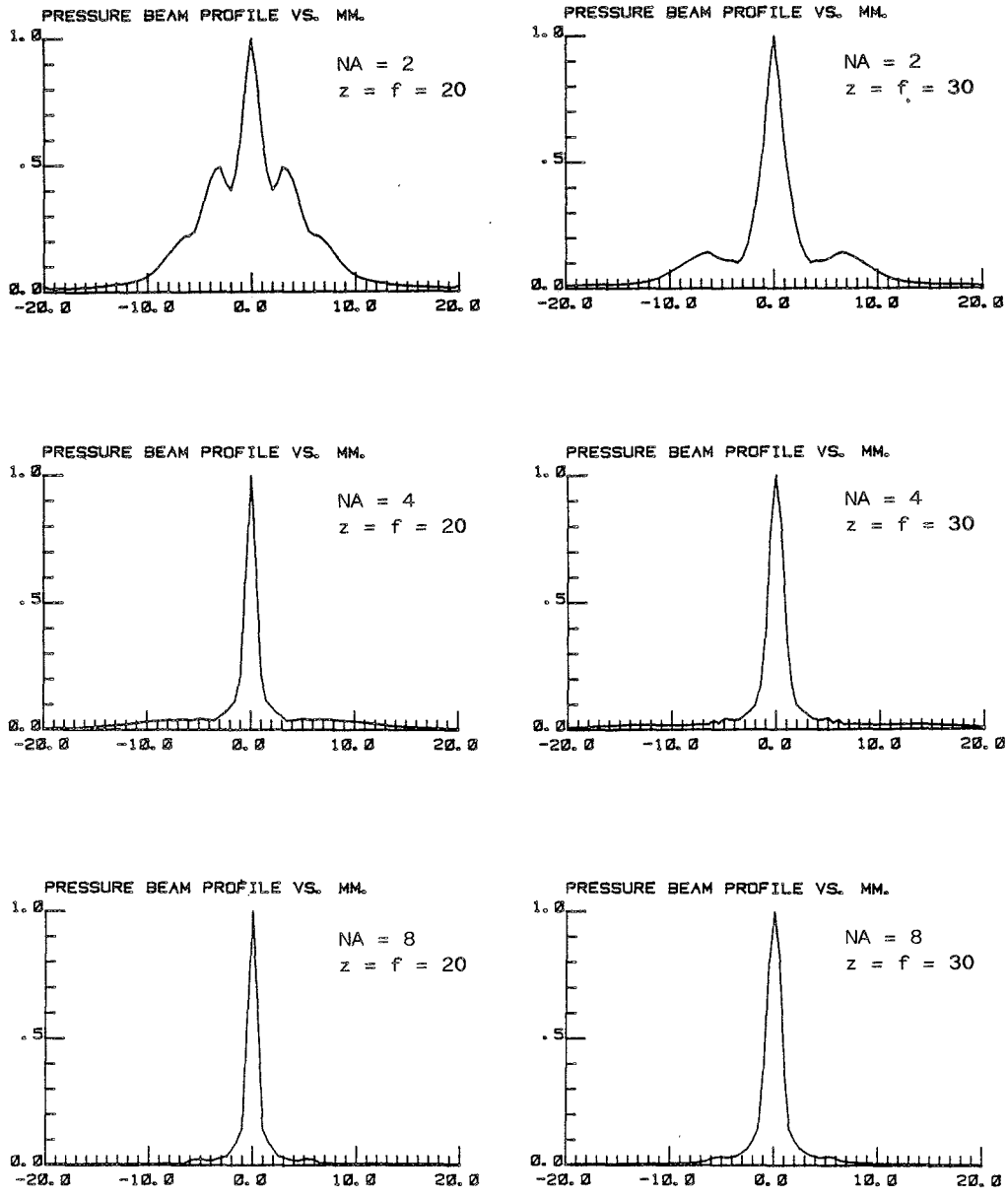

Fig. 4.23. Pressure beam profiles as a function of distance from the axis in mm at depth z in mm which equals the focal length f formed by an annular array with NA elements. The aperture diameter is 12.7 mm. The excitation is the medium pulse with centre frequency 3 MHz.

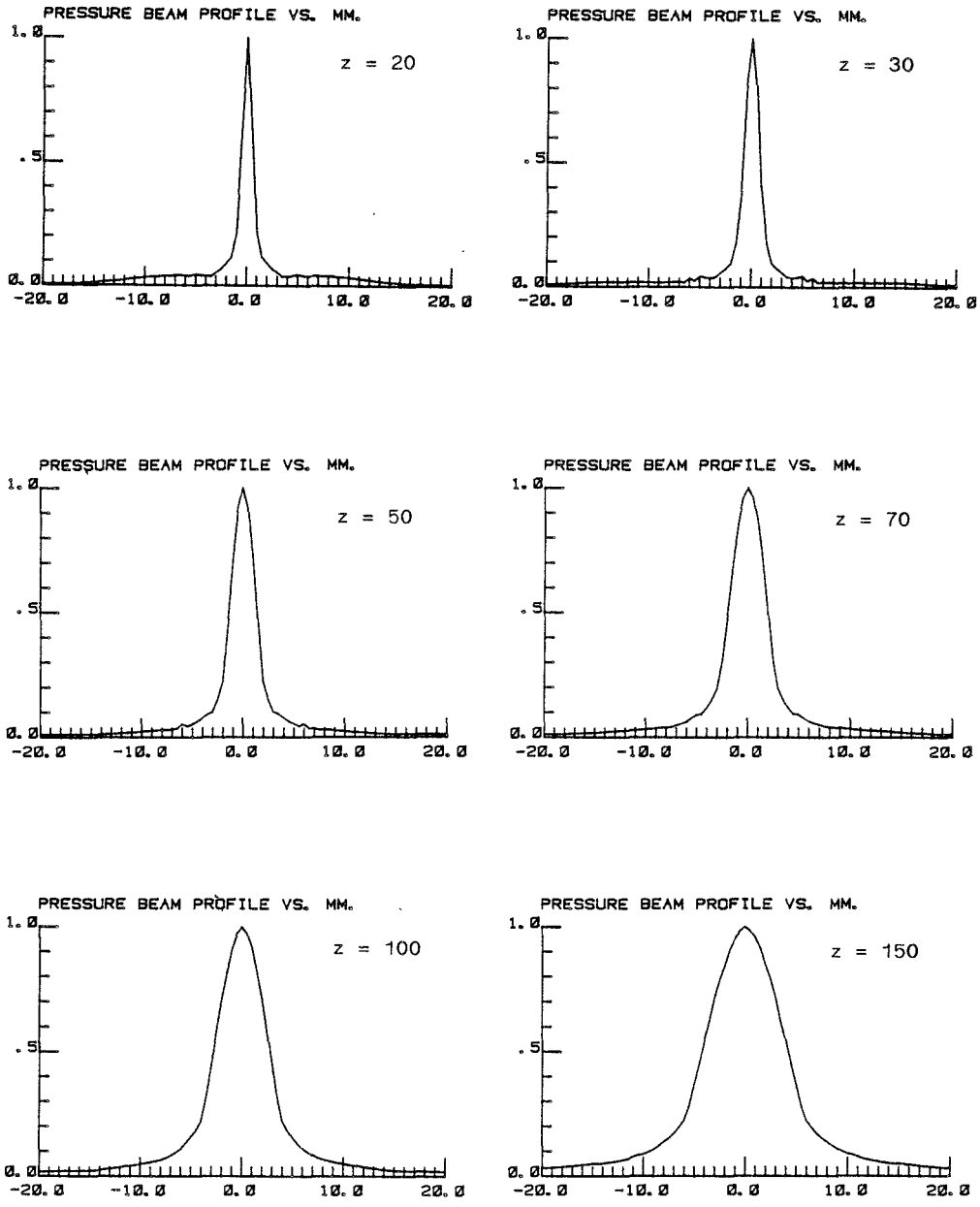

Fig. 4.24. Pressure beam profiles as a function of distance from the axis in mm at depth z in mm which equals the focal length formed by four annular elements. The aperture diameter is 12.7 mm. The excitation is the medium pulse with centre frequency 3 MHz.

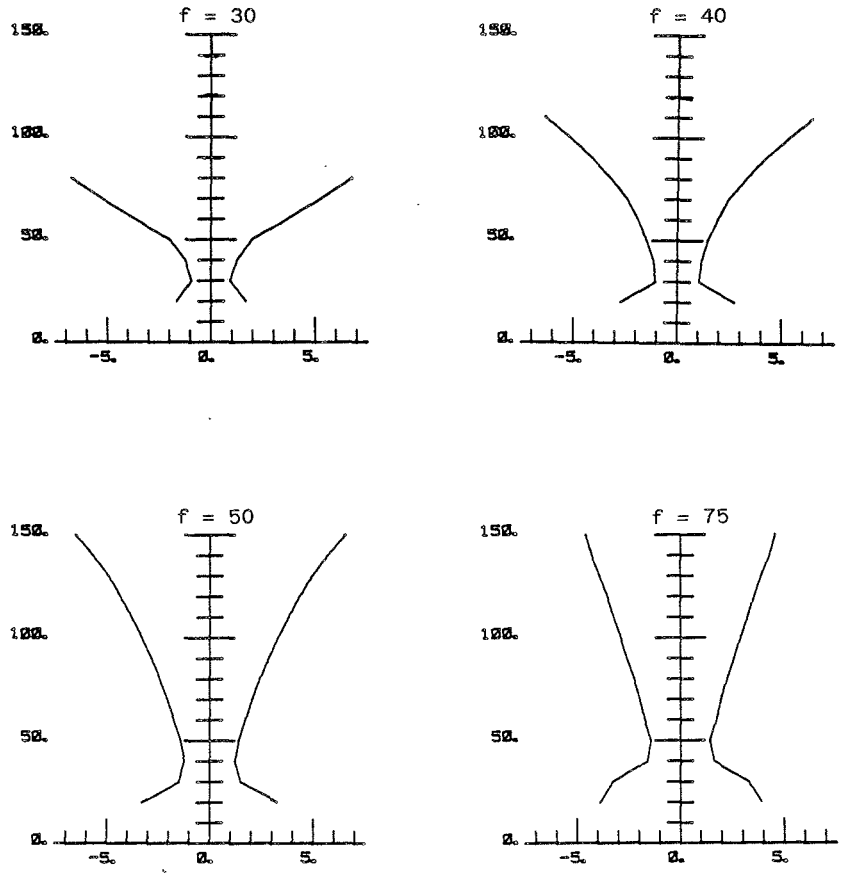

Fig. 4.25. Beam diameters as a function of depth in mm of a four element array with diameter 12.7 mm focused at f. The excitation is the medium pulse with centre frequency 3 MHz.

The above result might seem a bit surprising. We can however find similar results in the literature on gaussian beams [27]. For continuous waves with a gaussian beam profile one can show directly that the minimum beam diameter at a given depth is achieved by choosing the focal length equal to the depth. The beam waist will however be located closer to the aperture. Thus we have seen that our beam from the four element array in this respect behaves similar to a gaussian beam.

Finally, we will see how the pressure is as a function of time and distance from the axis at depths of 20 and 30 mm. This is shown in Fig. 4.26 for the four element array with focal length equal to the depths in both cases. Comparing these plots with the corresponding plots in Fig. 4.13.d we can see, that the beam is narrower in the near field when dynamic focusing is used relative to a fixed focus. But now we can see also that the edge waves are eliminated. On the axis at depth 20 mm we can see that the pressure pulse has the same length as the excitation pulse. This is due to the fact that the spatial impulse response is now only about a half period long. This was also the reason why we in the first place believed that four elements would be enough.

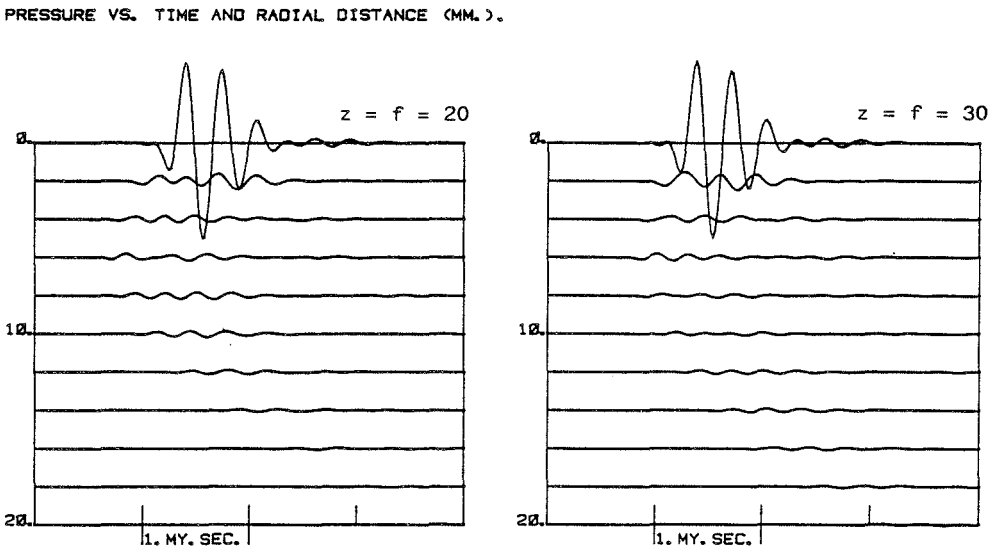

Fig. 4.26. Pressure as a function of time and distance from the axis in mm at depth z in mm from a four element array focused at f. The aperture diameter is 12.7 mm. The excitation is the medium pulse with centre frequency 3 MHz.

4.2.4. A focused annular array

In this subsection we will investigate the combination of a fixed focus formed by a lens or a curved aperture and a dynamic focus formed by an annular array. In the previous subsections we have started out by analyzing the on-axis spatial impulse response. Inspired by the success of this approach, we will proceed in the same way.

Our aim is to be able to focus properly in the depth range 20-150 mm, and we will therefore need an on-axis response that is shorter than half a period in the same depth range. With a focal length equal to 75 mm, the length of the on-axis response is 0.48 μs at depth 20 mm and 0.09 μs at depth 150 mm. To get an on-axis response that is shorter than half a period or 0.17 μs, it is therefore necessary to use four elements at depth 20 mm. At depth 150 mm however, the response is short enough already with one element. Looking at the on-axis response only, it might therefore be better to choose a fixed focus that gives us a response with the same length at depths 20 and 150 mm. With a fixed focal length equal to 35 mm we get an on-axis response with length 0.29 μs at 20 mm and the same at 150 mm. In this case it is sufficient to use two elements to get a response that is shorter than 0.17 μs both at depths 20 and 150 mm.

To check the validity of the above analysis we will run the computer program for a two-element aperture with the fixed focal length equal to 35 mm. The plot in Fig. 4.27.a shows the beam diameter as a function of depth in the case where dynamic focusing is used. That is, we let the total focal length be equal to the depth at all depths. We can see that the beam performs well. Compared with the beam diameter plot for the planar two-element aperture in Fig. 4.22, we can see that the near field is improved by using a fixed focus in addition to the dynamic focus.

Figure 4.27.b shows the beam profiles as a function of distance from the axis for the depths z equal to 20, 30, 50, 70, 100 and 150 mm, and with the total focal length equal to the depth for each plot. Comparing these plots with the results for the four-element aperture in Fig. 4.24, we can see that the sidelobes or skirts in general are increased. In the near field the beam profiles perform well, but in the far field the skirts are large and might be damaging to the image.

These results might suggest that the value of the fixed focal length of 35 mm was too short. To improve the far field beam profiles we can therefore increase the fixed focal length. Let us choose 55 mm. The beam diameter as a function of depth is shown in Fig. 4.28.a for the case where dynamic focusing is used. Again, the beam diameter performs well at all depths. The beam profiles are shown in Fig. 4.28.b. Comparing these with the plots in Fig. 4.27.b, we can see that the skirts in the far field have decreased and the skirts in the near field have increased as we expected. Fig. 4.28.c shows the pressure as a function of time and distance from the axis at the depths

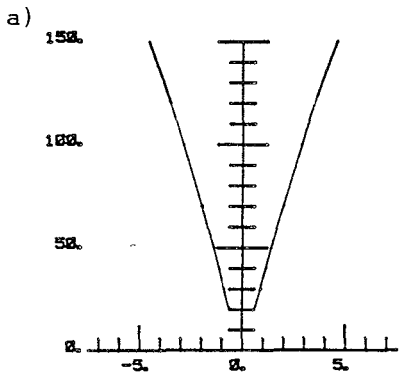

Fig. 4.27. Pressure from a two-element aperture with a fixed focal length of 35 mm when dynamic focusing is used. The aperture diameter is 12.7 mm and the excitation is the medium pulse with centre frequency 3 MHz.

a. Beam diameter in mm as a function of depth in mm.

b)

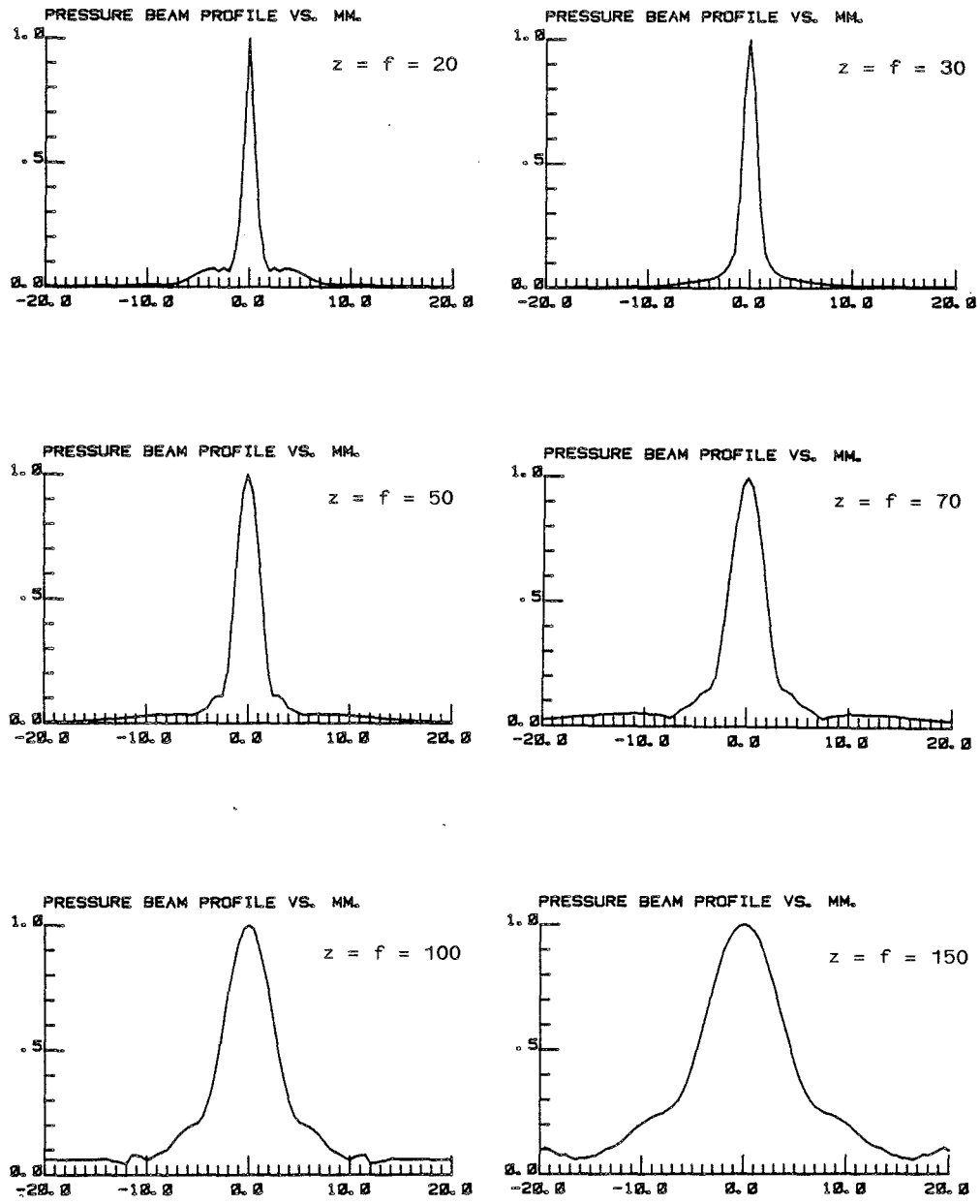

Fig. 4.27.b. Beam profiles as a function of distance from the axis in mm at depth z in mm and total focal length f.

z equal to 20, 30, 70 and 150 mm. Also here the total focal length f equals the depth at all depths. We can see that the pressure pulse is short as a function of time. It is of the same length as the velocity pulse generated from the transducer, and the influence on the length of the spatial impulse response is small.

To complete the calculations for the two-element transducer with a fixed focus of 55 mm, we have in Fig. 4.29 shown the transmission pressure field from this transducer. That is, the pressure field when the total focal length is 75 mm. This transducer will therefore have a pressure field as shown in Fig. 4.29 when transmitting, and as shown in Fig. 4.28 when receiving.

We have in this chapter shown the pressure fields of many different transducers. The problem is then to decide whether one particular design is good enough or not. The most important values for the resolution in the image are the beam

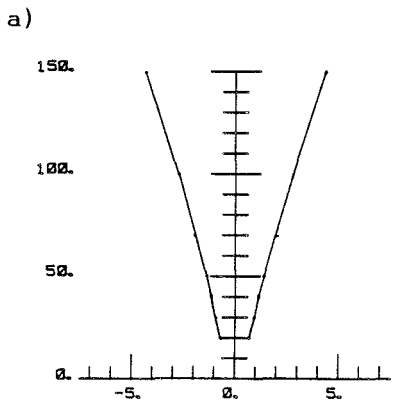

Fig. 4.28. Pressure from a two-element aperture with a fixed focal length of 55 mm when dynamic focusing is used. The aperture diameter is 12.7 mm and the excitation is the medium pulse with centre frequency 3 MHz.

a. Beam diameter in mm as a function of depth in mm.

b)

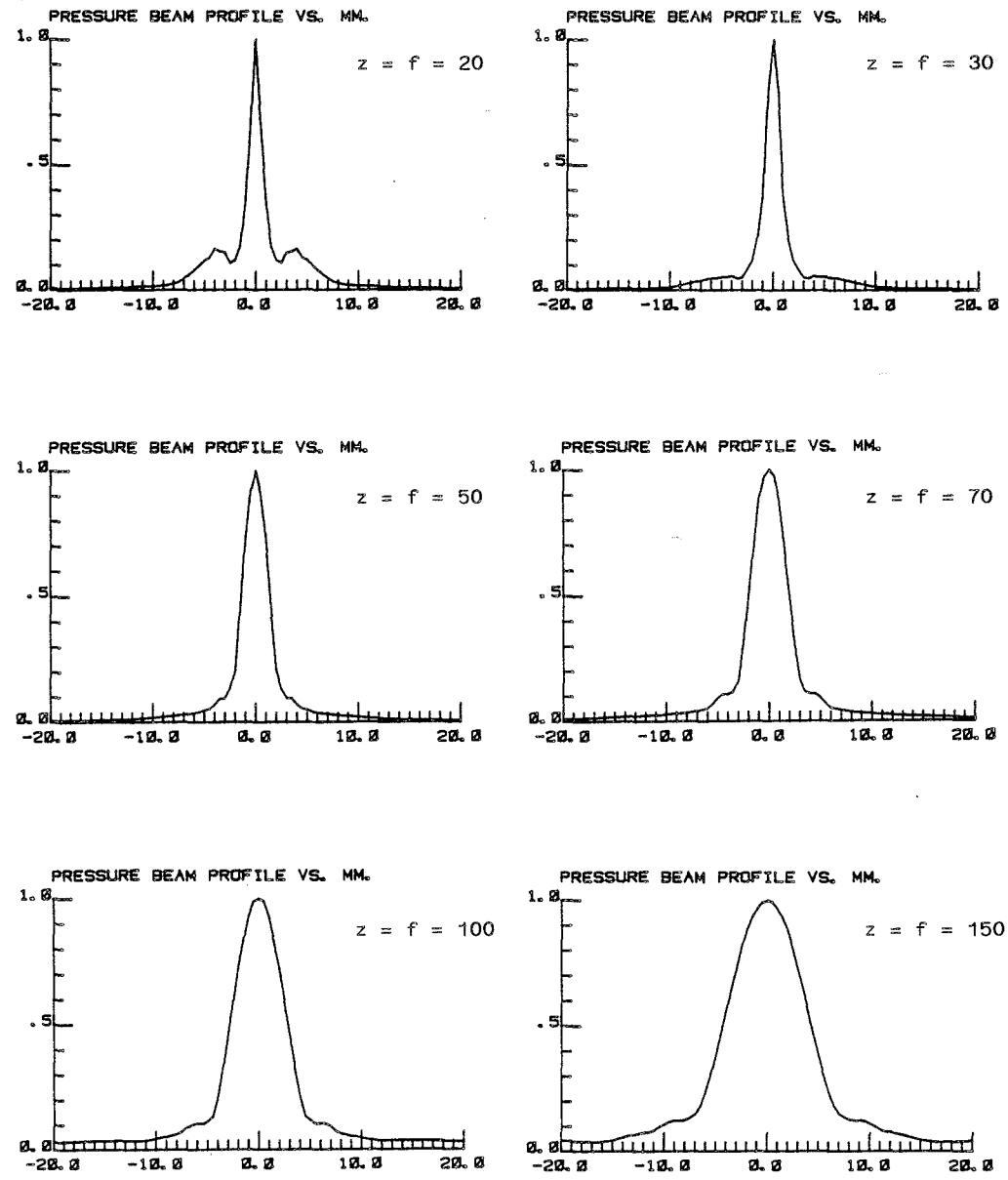

Fig. 4.28.b. Beam profiles as a function of distance from the axis in mm at depth z in mm and total focal length f.

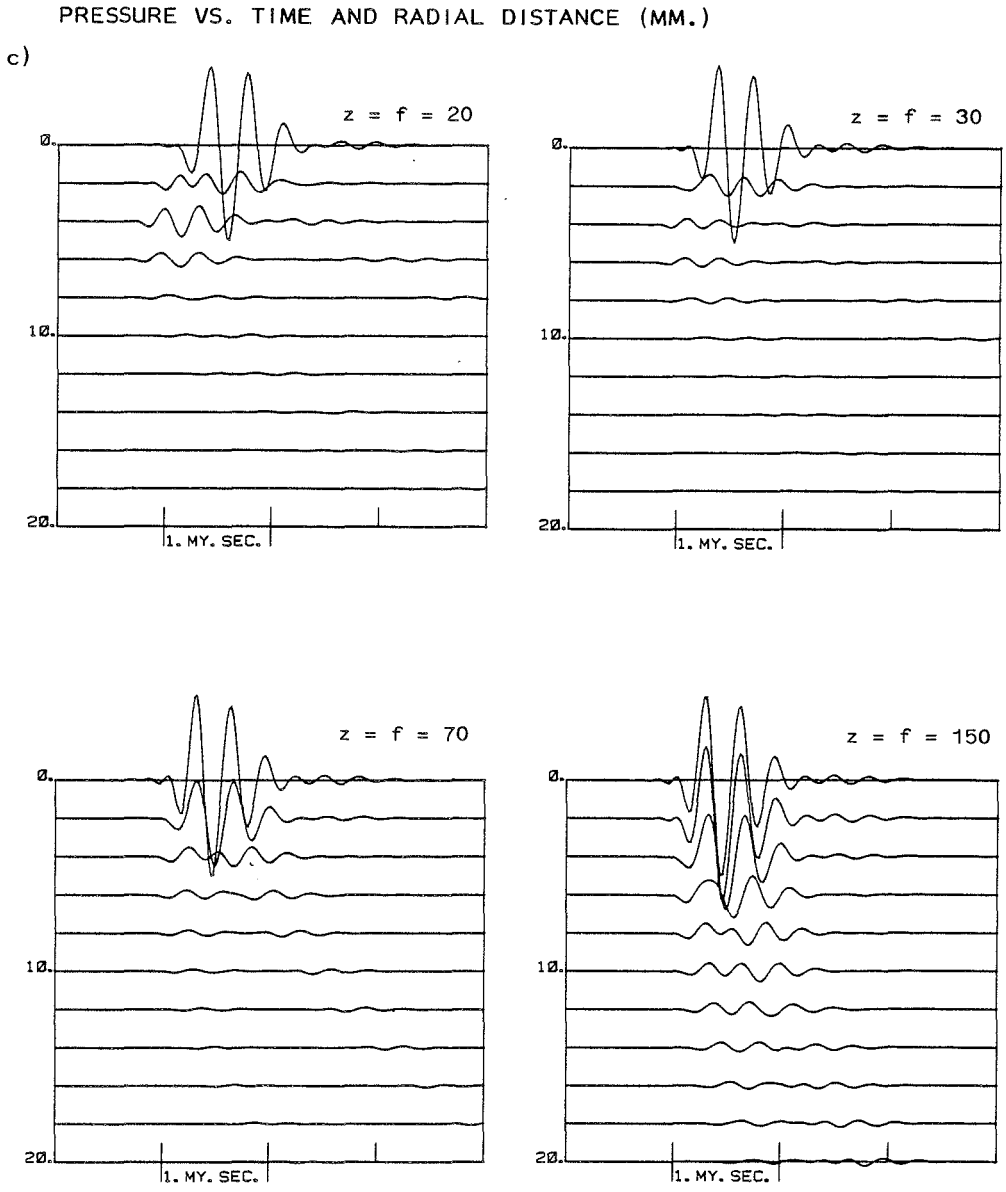

Fig. 4.28.c. Pressure as a function of time and distance from the axis in mm at depth z in mm and total focal length f.

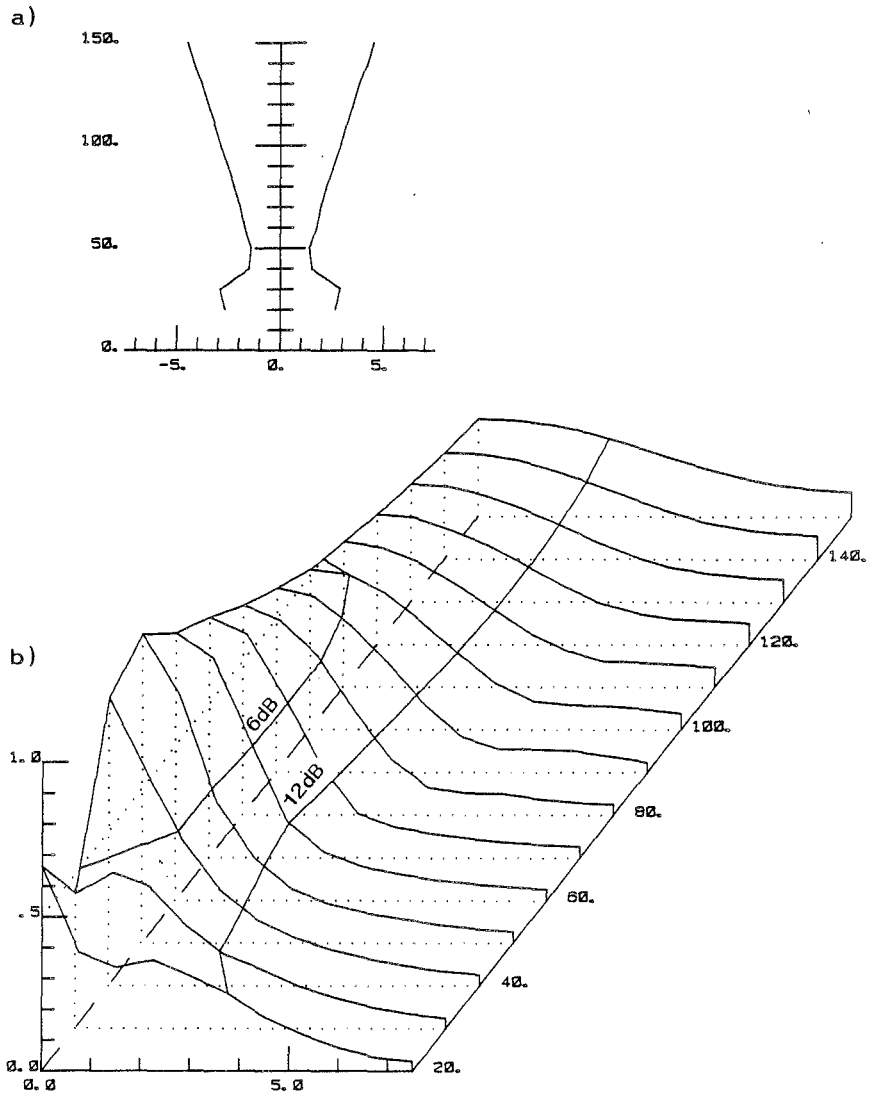

Fig. 4.29. Pressure from a two-element aperture with a fixed focal length of 55 mm and a total focal length of 75 mm. The aperture diameter is 12.7 mm and the excitation is the medium pulse with centre frequency 3 MHz.

a. Beam diameter in mm as a function of depth in mm.

b. Beam profile in perspective plot in space in mm.

c)

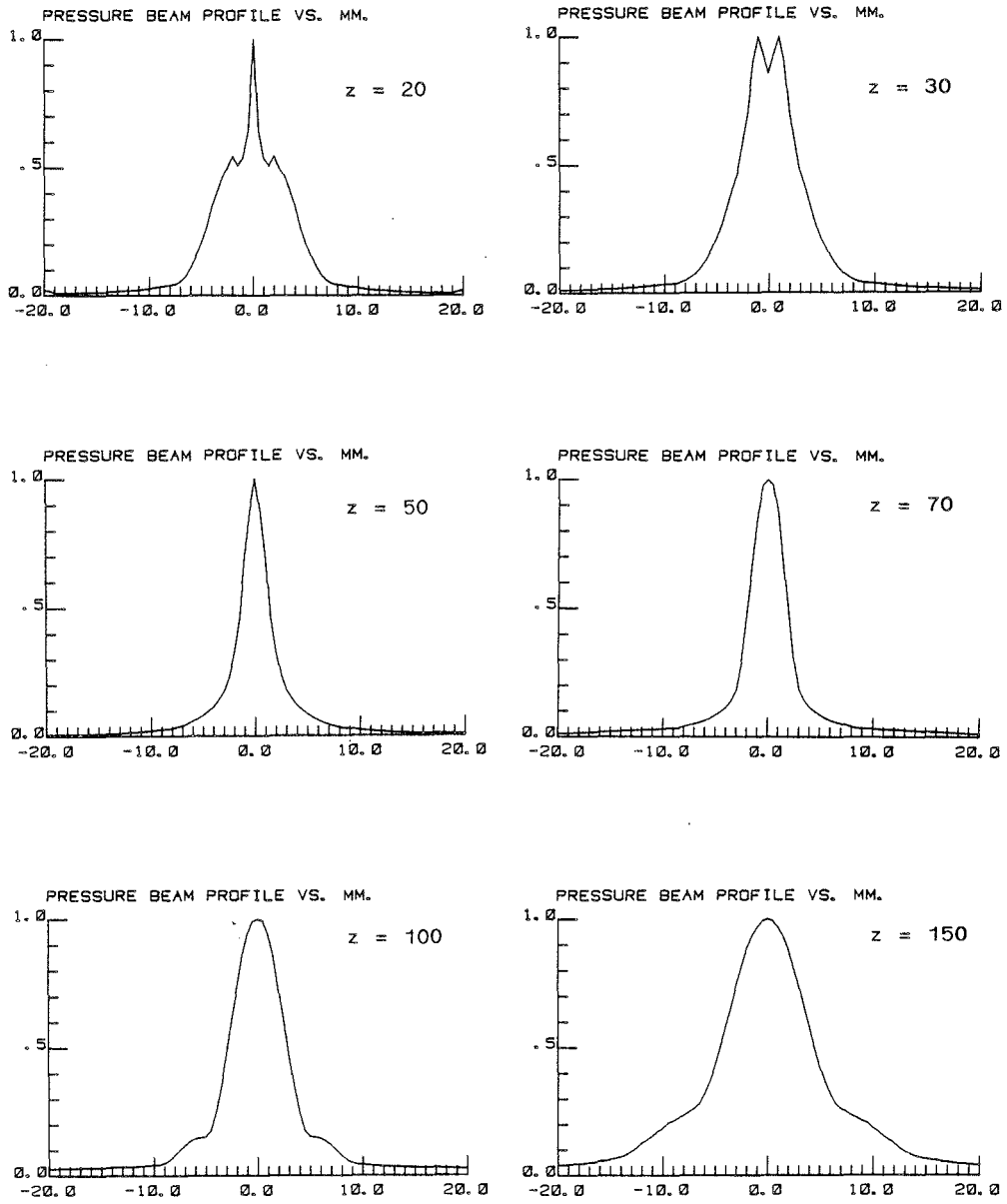

Fig. 4.29.c. Beam profiles as a function of distance from the axis in mm at depth z in mm.

diameter and the pulse length. The sidelobes, skirts and tails of the pulse will generate signal dependent noise. There is no algorithm to find the best aperture design. The decision must therefore be a judgement based on experience.

5. TRANSDUCER DESIGN AND MEASUREMENTS

In this chapter we will demonstrate the design and the measurements of the transducers. In particular, we will look at the design of quarter wave matching layers. Critical design parameters will be discussed.

The measurements presented in this chapter are the electric input impedance, the impulse response, the transfer function and the efficiency of the transducer. The transient diffraction fields will be presented in the next chapter.

The most important measurements will be the impulse response and the efficiency of the transducer. The impulse response tells us how good the depth resolution will be. The efficiency is important for the transducer sensitivity.

The measurements are done also to evaluate the transducer calculation model. The measurements of the electric input impedance of the transducer will be used to find the different modes of vibration. The transfer function can be used to find the modes that are coupled to the medium.

5.1. Transducer design

The only way to learn transducer design is through trial and error. Thus practical experience is a necessity. Some of the experience will, be mentioned, and in particular the fabrication of the quarter wave matching layer.

At a frequency of 3 MHz a half wavelength resonator of PZT will be about 0.7 mm thick. A typical thickness of a quarter wave matching layer is 0.2 mm. It is self-evident that the thickness of the electrodes and of the glue layers can be critical; also the homogeneity of the materials, parallelity of the layers and the size of the solder points. This has to be considered in all operations involved in the transducer fabrication.

The PZT elements used in the experiments are delivered from Ferroperm and the material data are given in [21]. A silver electrode of thickness 10 μm is deposited on each side of the element. The acoustic impedance of a typical PZT material is between 30 and 40 Mrayl (= 10^6 kg/m^2s). The impedance in silver is 38 Mrayl. The influence of the electrodes is therefore in essence that 3% of the thickness of the resonator is non-piezoelectric.

We want a high efficiency and therefore airbacking of the transducer. However, to get mechanical support we will use a porous material called divinycell. This is a stiff material with low density and the acoustic impedance is in the range 0.1 to 0.4 Mrayl. The acoustic impedance looking forward from the ceramic through one matching layer is, according to Table 3.2, 12 Mrayl at resonance. The result is that almost all the power is emitted in the forward direction.

With this light backing we can also tolerate a glue layer of thickness 0.1 mm between the element and the backing.

A glue layer between the element and the matching layer is a greater problem. A special high pressure method has been developed to get the glue layer as thin as a few micrometers [19]. If, however, a filled epoxy is used as the material in the matching layer, the whole problem can be eliminated by molding the epoxy straight onto the element. This requires a fill that will not sink to the bottom before the epoxy hardens. We have therefore chosen to use dolomit powder instead of a metal powder as fill in the epoxy. This unables us to make composites with as high impedances as if metal powder had been used, but we will only need an impedance of 4.25 Mrayl anyway. The dolomit powder, called microdol, that is used here has a grain size of 1-8 μm and the composite will therefore be homogeneous at a frequency of 3 MHz. The epoxy used is Chiba Geigy XW 396-397. The density, velocity and impedance were measured as a function of weight percent microdol and the results are shown in Fig. 5.1. The

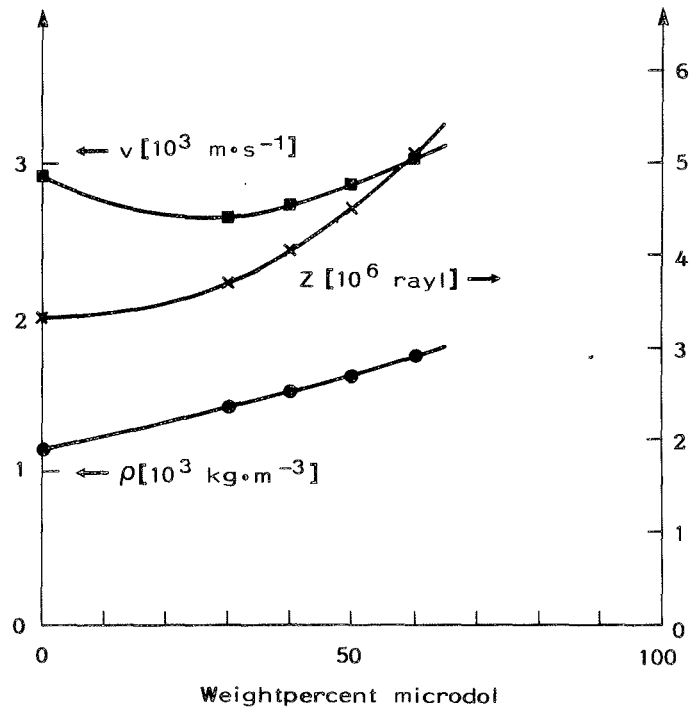

Fig. 5.1. Density, velocity and impedance of the filled epoxy as a function of weight percent microdol.

uncertainty in the velocity is about ± 50 m/s and in the impedance ± 0.1 Mrayl.

From the plot we can read that the desired impedance of 4.25 Mrayl is achieved with 45% microdol. The velocity is then 2800 m/s and the desired thickness of a quarter wave matching layer at 3 MHz is therefore 0.23 mm.

Thus, the fabrication of the quarter wave matching layer is done by mixing the epoxy and microdol. This mixture is evacuated to avoid gass bubbles and molded directly onto the element. After hardening the filled epoxy is ground down to the proper thickness. The accuracy in the grinding process is ± 5 µm.

In Fig. 5.2 are shown calculated impulse responses and module of the corresponding transfer functions for some parameter

settings. Figure 5.2.a shows the ideal parameter setting and is the same as in Figure 3.5.a. Figure 5.2.b shows the effect of adding 10 μm silver electrodes. Figure 5.2.c shows the effect of the backing with impedance 0.4 Mrayl and a glue layer of 0.1 mm thickness between the backing and the element. The transfer function here is reduced with 2% only relative to the ideal case. Figure 5.2.d shows the effect of reducing the impedance of the matching layer to 4.0 Mrayl. Figure 5.2.e shows the effect of increasing the thickness of the matching layer to 0.25 mm. For all the plots in Fig. 5.2 the changes are acceptable and indicate the tolerable inaccuracies in the fabrication of the transducers.

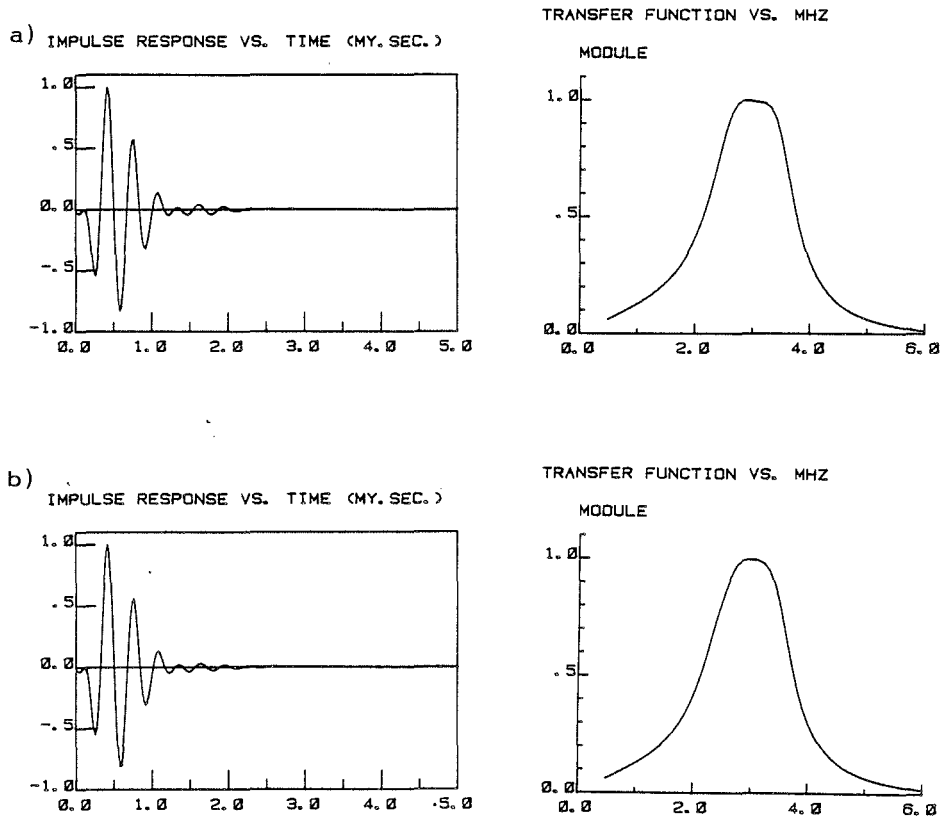

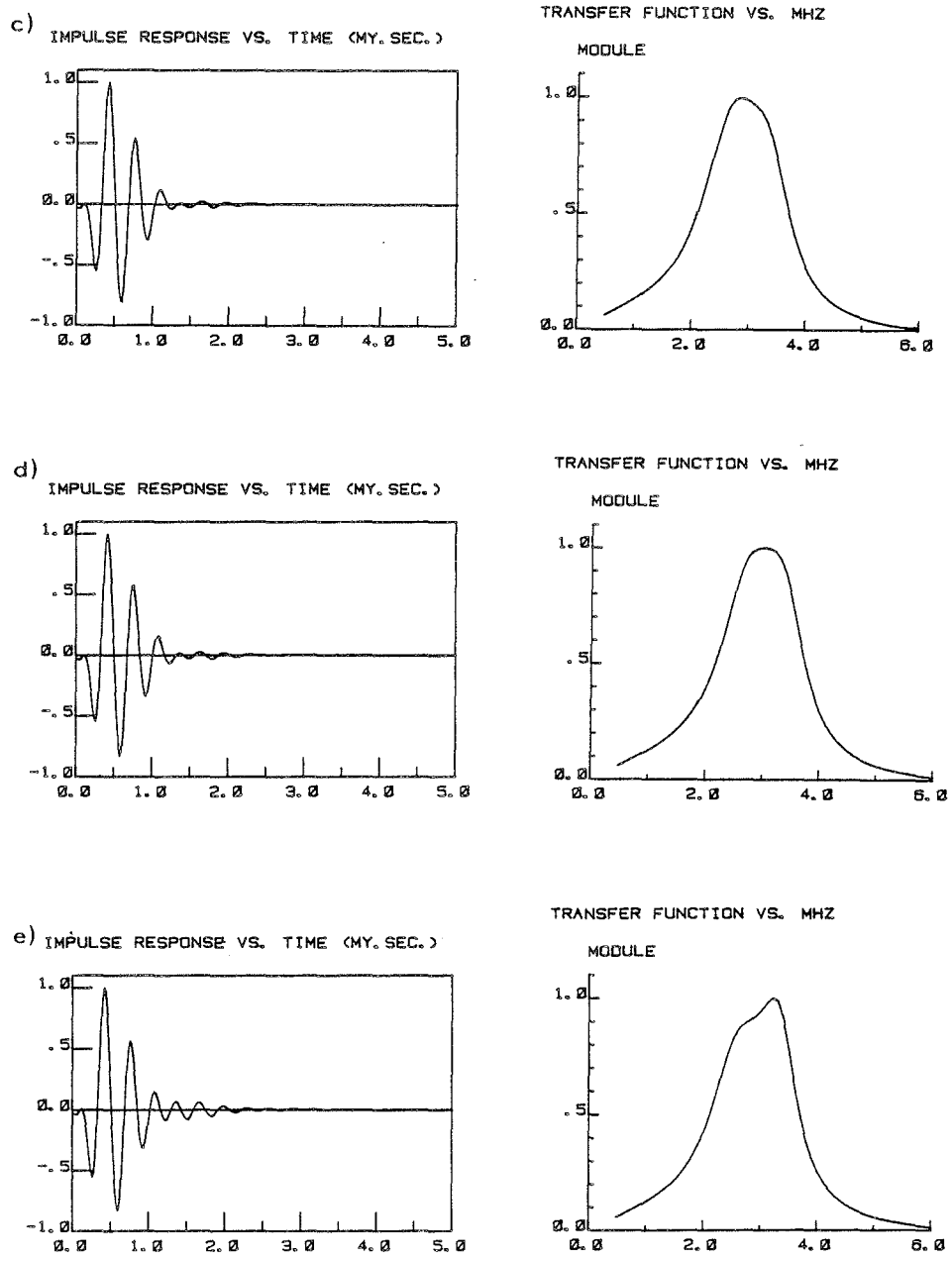

Fig. 5.2. Acceptable changes in parameters for fabrication of transducers. The disc diameter is 12.7 mm and the centre frequency is 3 MHz.

a. Ideals
b. 10 µm silver electrodes included
c. Backing and glue layer included
d. Matching layer with impedance 4.0 Mrayl instead of 4.25 Mrayl
e. Matching layer with thickness 0.25 mm instead of 0.23 mm.

5.2. Transducer measurements

For measurement purposes the transducers are placed in a measurement tank from Medisonics, England. This is supplied with a micropositioning manipulator which has a resolution of 0.1 mm in the transversal direction and 1.0 mm in the longitudinal direction. The hydrophone is a 1 mm PVDF probe from the Danish Institute of Biomedical Engineering. The diameter of the aperture is 1.0 mm and the sensitivity is -264 dB relative to V/μPa in the frequency range 1-10 MHz when it is connected to a 1 MΩ load impedance.

The input signal to the transducer is generated from a Pulsetek pulse generator 233 which has two channels. This is capable of producing pulses as short as 10 ns. When a continuous burst is required, the pulse generator and a switch are used to modulate a continuous signal from a Hewlett Packard 3312 A Function Generator. The signal is amplified by a EIN 503 L Power Amplifier which has a frequency range from 1 to 500 MHz. The output impedances of the generators are 50 Ω.

The signal from the hydrophone is amplified in a Tektronix Type 127-1A5 Preamplifier with a 1 MΩ input. The signal is read from a Tektronix 2213 oscilloscope. The configuration is shown in Fig. 5.3.

The electric input impedance of the transducer is measured with a Hewlett Packard 4815 A RF Vector Impedance meter. This can measure the module and phase in the frequency range 0.5 - 500 MHz.

The impulse response of the transducer is measured by exciting the transducer with a pulse that is shorter than 100 ns. The hydrophone is placed in the focal point or in the far field for an unfocused transducer where the spatial impulse response is a δ-pulse.

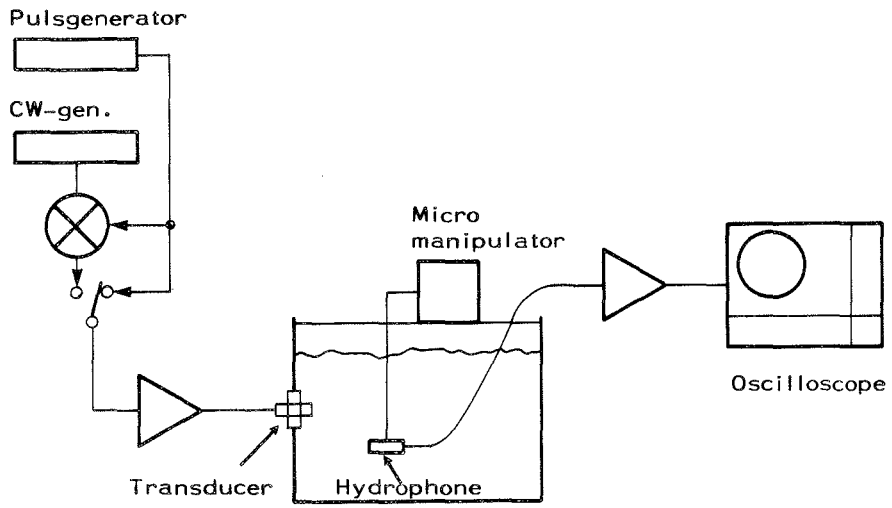

Fig. 5.3. The measuring configuration.

The measurement of the transfer function is done with the hydrophone in the same position. A CW-burst is used as an input to the transducer and the burst centre frequency is varied from 0.5 to 6 MHz.

The efficiency of the transducer has been measured by measuring the output acoustic power with a power meter designed by Engan [28]. The transducer is excited with a 3 MHz continuous voltage of known amplitude and the input electric power can be calculated when we have measured the electric input impedance. The efficiency is then found as the ratio between the output acoustic power and the input electric power.

5.2.1. The single element transducer

A single element circular disc transducer with one quarter wave matching layer has been fabricated as described in the previous section. The diameter of the disc is 12.7 mm and the centre frequency is 3 MHz.

In Fig. 5.4.a is shown the calculated time derivative of the impulse response. Thus, it can be compared directly with the measured acoustic pressure. The 12 dB pulse length is 0.7 μs. Figure 5.4.b shows the measured impulse response. Here the 12 dB pulse length is also 0.7 μs. The main pulse is very close to the calculated one. The tail of the pulses are however somewhat different in the two cases.

In Fig. 5.4.c is shown the calculated generator voltage to pressure transfer function for the transducer. The 6 dB bandwidth is 1.7 MHz. Fig. 5.4.d shows the measured transfer function. Also here the 6 dB bandwidth is 1.7 MHz. While the calculated transfer function has a flat top, the measured one has a peak at 3.5 MHz. This is in agreement with what we predicted in Chapter 3, a peaked transfer function gives an impulse response with a bigger tail.

The efficiency of the transducer was measured to be 89% at 3 MHz. With the divinycell backing and the loss model developed in chapter 3, we get a theoretical efficiency of 92%. This agreement is excellent.

Fig. 5.5.a shows the calculated electric input impedance of the transducer and Fig. 5.5.b shows the measured electric input impedance. The differences between the calculated and the measured results are more vital here than for the impulse response and the transfer function. In the measured results we can see a resonance at 0.6 MHz and another at 0.9 MHz, which are not present in the calculated results. At 3 MHz the calculated module is 36 Ω and the phase is -43^0. The measurements at 3 MHz show a module equal to 30 Ω and a phase equal to -35^0. The shape of the plots around resonance is also somewhat different in the two cases.

There are two principal reasons for the disagreement between the calculated and measured results. The first is that the parameter input to the calculation model may be different from the actual parameters. The second is that the model is too

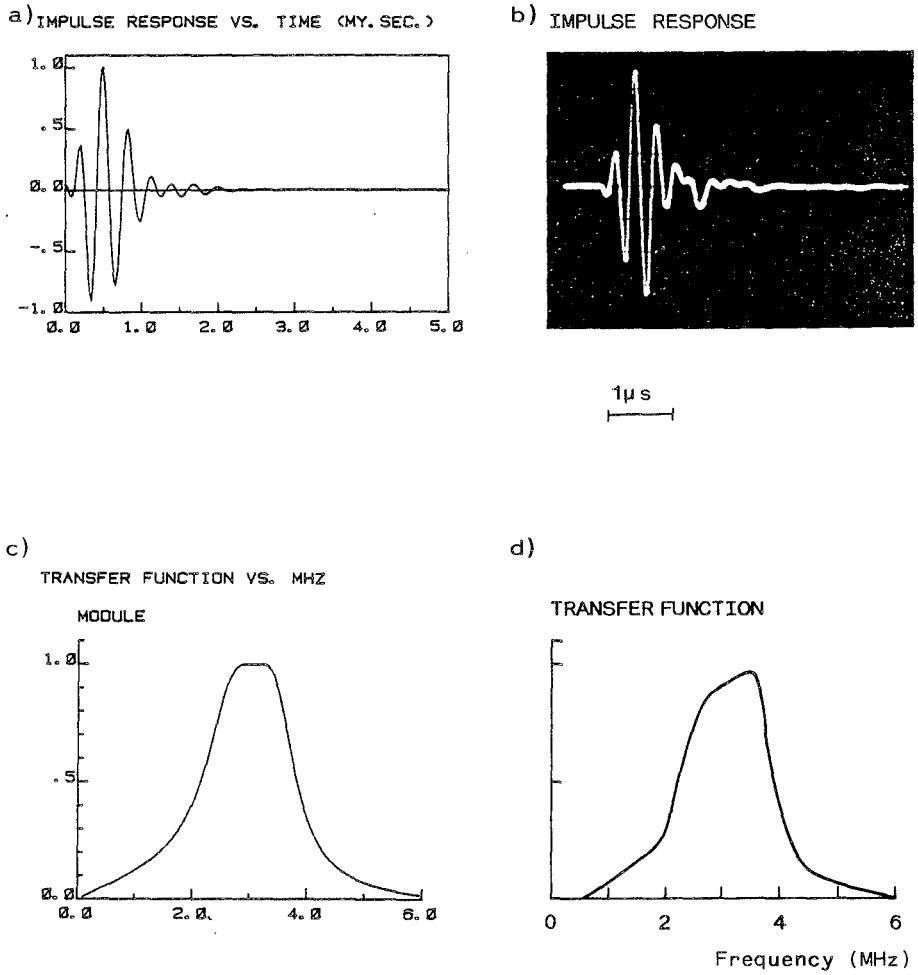

Fig. 5.4. The single element transducer with one matching layer. The disc diameter is 12.7 mm and the centre frequency is 3 MHz.

a. Calculated impulse response
b. Measured impulse response
c. Calculated transfer function
d. Measured transfer function

simple. Changes in a parameter that is believed to be important were examined in the previous section. The results indicate that even if errors in the parameters may explain some disagreement between the calculated and measured results, this can not explain it all.

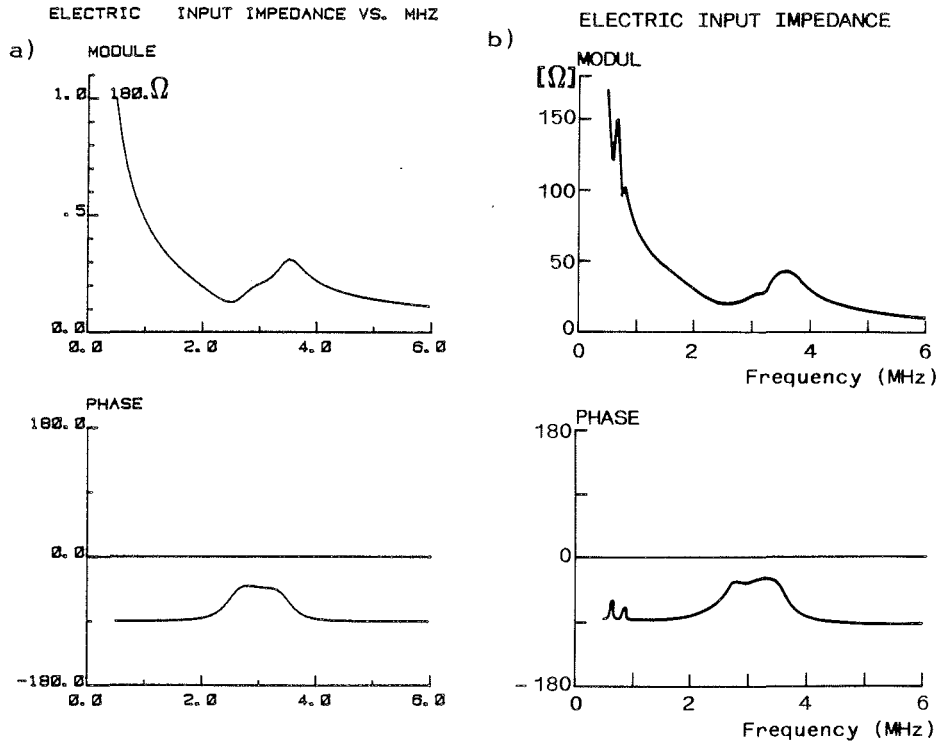

Fig. 5.5. Electric input impedance of the single element transducer with one matching layer. The disc diameter is 12.7 mm and centre frequency is 3 MHz.

a. Calculated
b. Measured

The model is too simple, as already stated in Chapter 3. While the wave equation has nine independent solutions in a solid medium, our model only takes one of them into account. It is obvious that this is the explanation for the two measured resonances at 0.6 and 0.9 MHz in the input impedance. The model has no possibility of finding those modes. It might also be that other modes of vibration influence the shape of the impedance around 3 MHz.

The agreement between the calculations and the measurements is much better for the impulse response and the transfer function than it is for the input impedance. This can be understood

when recalling that the impulse response and the transfer function are measured with the hydrophone in the focal point. The reason for this placement is that the spatial impulse response is a δ-pulse of time in the focal point, and therefore the pressure will be the time derivative of the normal velocity on the transducer surface. The mode of vibration that is included in the transducer model, namely the longitudinal pressure wave, only gives a normal velocity on the surface. However, all the other modes of vibration may have velocity fields that are quite different and therefore radiate in other directions, or hardly radiate at all. This favours the suggestion that most of the disagreements between the calculated and measured input impedance are due to other modes of vibration rather than errors in the input parameters.

5.2.2. The two-element transducer

A two-element annular array has also been fabricated. It consists of a centre disc of diameter 9.7 mm and an outer ring with inner diameter 10.2 mm and outer diameter 13.7 mm. Also for this transducer the thickness resonance frequency is 3 MHz. The PZT-elements were glued to the divinycell backing which has an acoustic impedance of 0.4 Mrayl. Afterwards the filled epoxy was molded on the front and ground down to the proper thickness. This method of producing the matching layer gave an uncertainty in the thickness of the matching layer of ± 10 μm.

The calculated impulse response is shown in Fig. 5.6.a. It has a 12 dB pulse length of 0.7 μs. The measured impulse response of the inner element is shown in Fig. 5.6.b. This has a 12 dB pulse length of 0.7 μs. The measured impulse response of the outer element is shown in Fig. 5.6.c. This has a 12 dB pulse length of 0.7 μs. Finally, in Fig. 5.6.d is shown the impulse response for both the elements excited in parallel. The impulse responses for the inner and outer element were excited with the same generator voltage over the

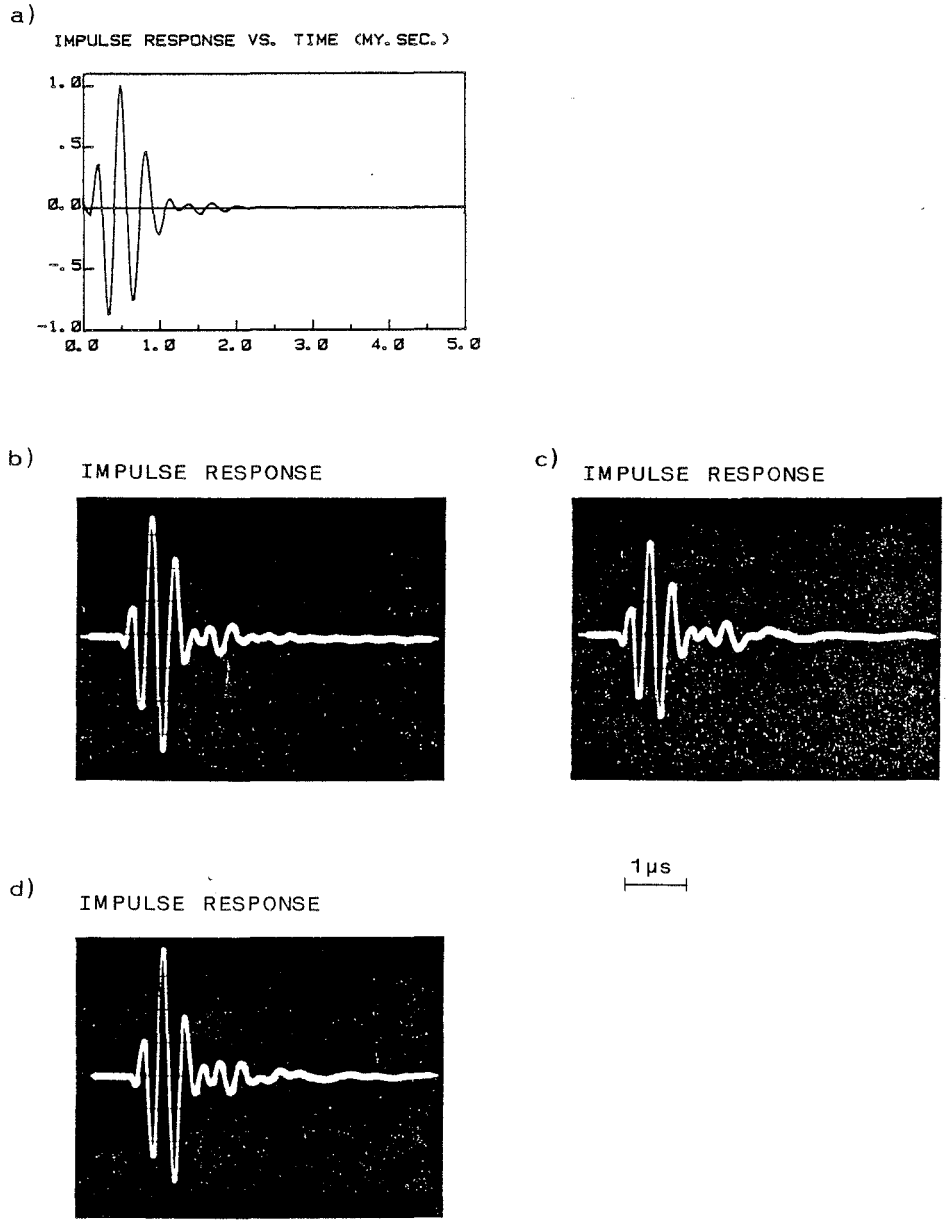

Fig. 5.6. Impulse responses for the two-element transducer with one matching layer. The aperture diameter is 13.7 mm and the centre frequency is 3 MHz.

a. Calculated
b. Measurement for inner element
c. Measurement for outer element
d. Measurement for both elements in parallel

50 Ω line, but still the response from the outer element is 2.5 dB lower than the inner element. Also for the outer element we can observe a 1 MHz period tail of the pulse.

The calculated generator voltage to pressure transfer function is shown in Fig. 5.7.a. The 6 dB bandwidth is 1.7 MHz. The measured transfer function for the inner element is shown in Fig. 5.7.b. The 6 dB bandwidth is 1.6 MHz. The measured transfer function for the outer element is shown in Fig. 5.7.c. The 6 dB bandwidth is 1.6 MHz. For the inner element the result is very much the same as for the single element transducer. The transfer function has a peak at 3.3 MHz and this is in agreement with a bigger tail in the impulse response. For the outer element the transfer function has peaks at 3.4, 2.7 and 1.0 MHz. The peaks around 3 MHz can not be separated in the impulse response, but as mentioned above, we observe a weak 1 MHz period signal in the impulse response.

The measured efficiency of the inner element is 88% and 57% of the outer element. As for the single element transducer the calculated efficiency is 92%. The calculated and measured efficiency are in good agreement for the inner element but in poor agreement for the outer element.

The calculated electric input impedance is shown in Fig. 5.8.a. At 3 MHz the module is 62 Ω and the phase is -43^{0}. The measured impedance for the inner element is shown in Fig. 5.8.b. At 3 MHz the module is 36 Ω and the phase is -44^{0}. We can see also that there is a resonance at 0.5 MHz and another at 0.75 MHz. The shape of the plots around 3 MHz is different from the calculated ones for both the module and the phase. The measured impedance for the outer element is shown in Fig. 5.8.c. The module at 3 MHz is 56 Ω and the phase is -58^{0}. There is a strong resonance at 1.0 MHz and a weaker at 2.0 MHz. The shape of the module and phase around 3 MHz is also here different from the calculated one.

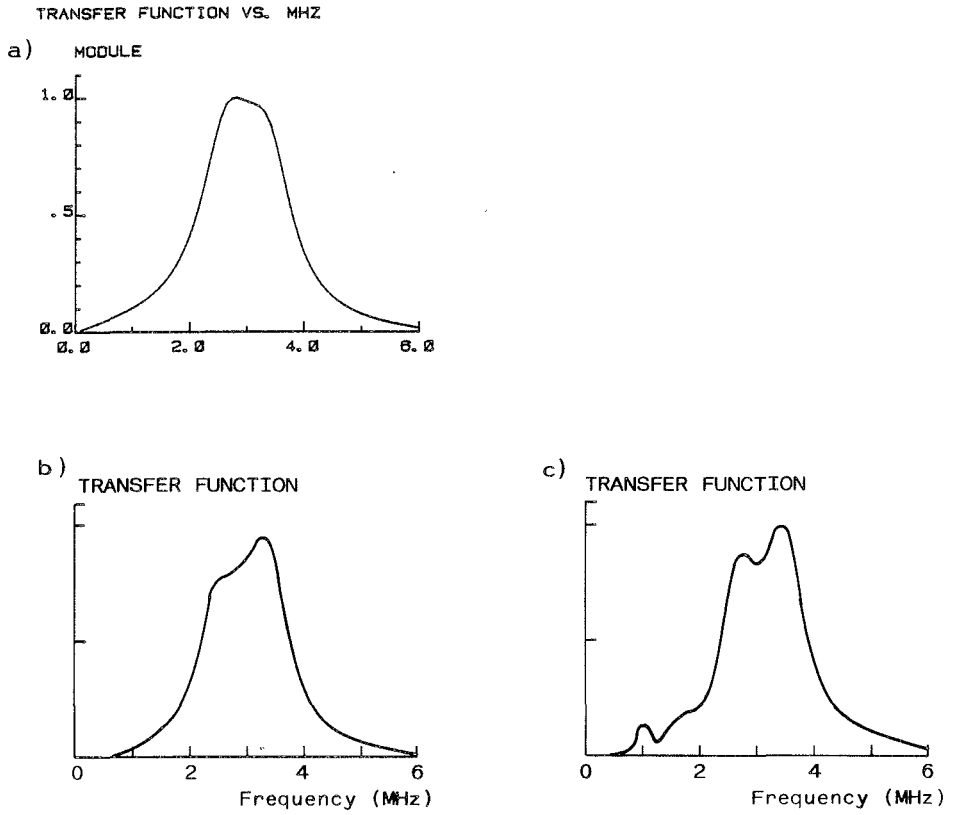

Fig. 5.7. Module of the transfer functions for the two-element transducer with one matching layer. The aperture diameter is 13.7 mm and the centre frequency is 3 MHz.

a. Calculated
b. Measurement for the inner element
c. Measurement for the outer element

The discussion of the results for the single element transducer is valid also for the two-element transducer. The disagreements between the calculations and the measurements are however greater for the outer element in the two-element transducer. This is due to the fact that the transversal dimension of the outer element is of the same order as the thickness of the element. The thickness is 0.69 mm and the width is 1.75 mm. The piezoelectric ceramic that is used, PZ

27, have a coupling factor in the transversal direction equal to 0.36 while the longitudinal coupling factor is 0.69. This indicates that the 1 MHz resonance might be the fundamental resonance of the transversal pressure wave. If so, the wavelength should be 3.5 mm and the effective velocity 3500 m/s. The bulk velocity for a pressure wave in PZ 27 is 4350 m/s, but piezoelectric coupling and transversal contraction will reduce the effective velocity. The 1 MHz resonance is therefore most likely the transversal vibration mode.

If we take into account the nine independent solutions of the wave equation and their harmonics and all the linear combinations of these, and also the uncertainty due to mechanical and electric coupling, we can fit almost any resonance frequency. This is highly speculative and we will therefore not do so. We just have to admit that we can not account for all the measured resonances.

The measured efficiency of the inner and outer element differs with 1.9 dB. The lower efficiency of the outer element may be due to the fact that it is more in contact with the filled epoxy which fills up the space in between the elements and around the outer element. Also spurious modes of vibration close to 3 MHz may absorb energy.

However, the impulse responses are satisfactory. Most important for an annular array is the fact that the impulse responses are equal. We have noticed that the impulse response from the outer element is 2.5 dB lower than the one from the inner element when driven with the same generator voltage. The lower efficiency of the outer element accounts for 1.9 dB and the higher real part of the electric input impedance of outer element accounts for 0.2 dB. Finally all the other modes of vibration in the outer element will absorb energy due to the transient excitation. This difference in the magnitude of the two responses can however easily be compensated for.

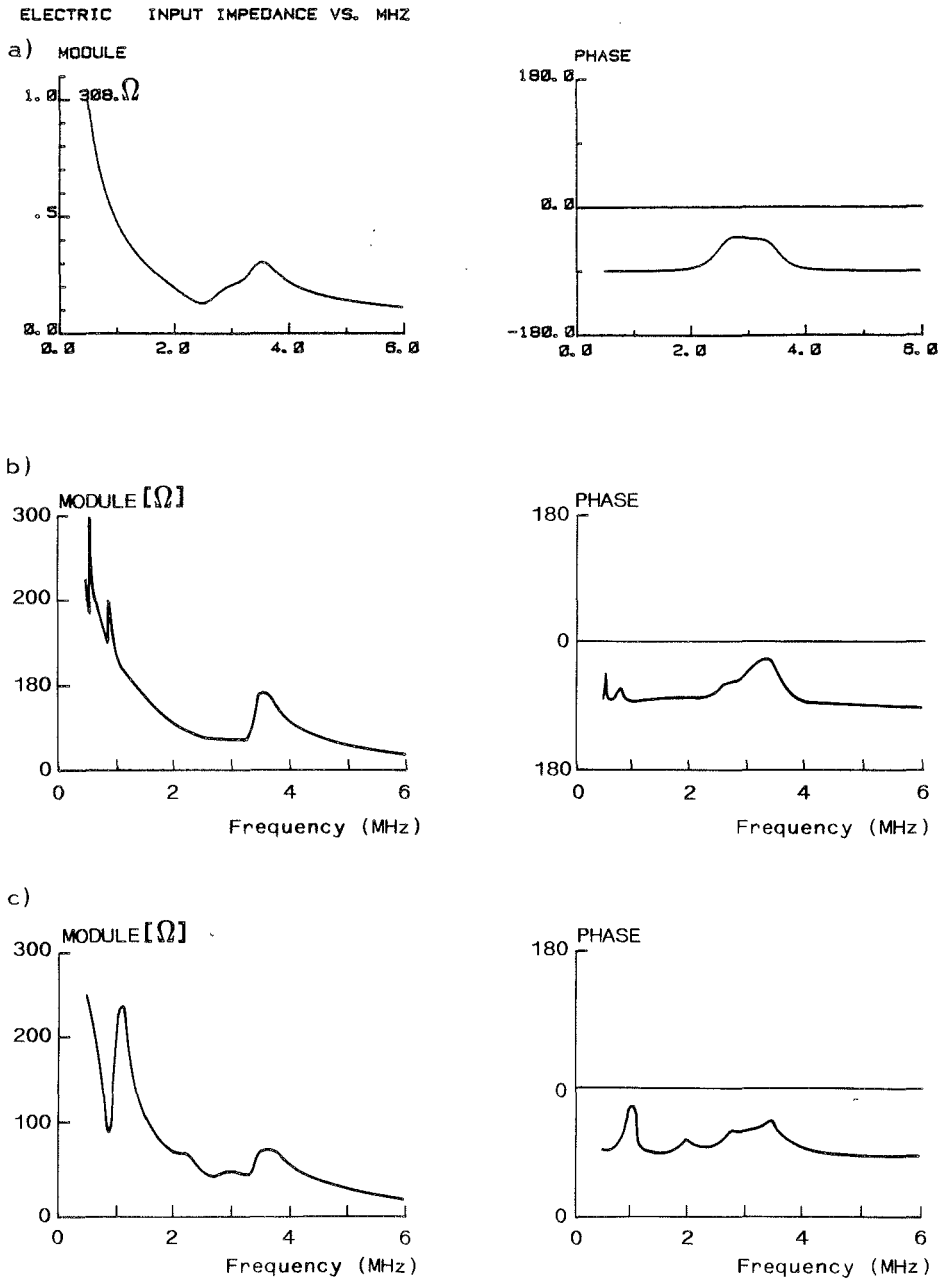

Fig. 5.8. Electric input impedance for the two-element transducer with one matching layer. The aperture diameter is 13.7 mm and the centre frequency is 3 MHz.

a. Calculated
b. Measured for the inner element
c. Measured for the outer element

6. MEASUREMENTS OF TRANSIENT DIFFRACTION PATTERNS

The beam observation tank is used for measurements of the fields from the transducers. The tank and the rest of the measuring equipment were described in the previous chapter. An important parameter for the field measurements is the hydrophone diameter which is 1.0 mm. We also recall that the resolution of the micro manipulator is 0.1 mm in the transversal direction and 1.0 mm in the longitudinal direction.

The lenses used in the experiments are made of a high density silicone called Sylgard 170 from Dow Corning. The velocity in the silicone is 1010 m/s, which gives a refraction index of 1.49 relative to water. Thus we can make thin lenses, which give low second order aberrations [29]. The acoustic impedance in the silicone is 1.4 Mrayl which gives low reflection at the water-silicone interface.

6.1. The single element transducer

Calculations of the fields from a single element transducer are shown in Chapters 4.2.1 and 4.2.2. In Chapter 4.2.1 we calculated the pressure fields for a disc with focal length equal to 75 mm. The medium was excited with a continuous wave, a half wavelength pulse and the pulse coming from a transducer with one matching layer. The half wavelength pulse is not available and can not be used in the measurements. The calculations of pressure field for the planar disc are shown in Chapter 4.2.2. The excitations mentioned above were used in this case as well.

In Fig. 6.1 are shown measurements of the half value beam diameter as a function of depth for both a planar and a focused disc with both pulse and CW excitation.

The measurements of the planar CW excited disc in Fig. 6.1.a correspond to the calculations in Fig. 4.17.a. The measurements show a beam waist at 75 mm where the beam diameter is 5.1 mm. The calculation gave us 5.0 mm at depth 80 mm. At depth 150 mm the measurements give a diameter of 8.8 mm, while the calculated result is 8.3 mm. This is the largest disagreement between the measured and the calculated diameter outside the beam waist. At depth 20 mm the measurements show a diameter of 10.4 mm, while the calculation gave us 11.6 mm. The largest disagreement between the measurement and the calculation inside the beam waist is found at depth 50 mm, where the diameter is measured to be 7.6 mm and calculated to be 10.7 mm.

Figure 6.1.b shows the measured beam diameter for the pulse excited planar disc, and corresponds to the calculations in Figure 4.18.a. The measurements show a beam waist at depth 90 mm where the diameter is 6.1 mm. The calculation shows also a beam waist at 90 mm, but the diameter is 6.6 mm. At depth 150 mm the measured diameter is 8.8 mm, while the calculated is 8.6 mm. At depth 20 mm the measured diameter is 11.5 mm, while the calculated is 12.2 mm. The difference between the measured and calculated results is within 0.3 mm outside the beam waist and 1.0 mm inside the beam waist.

Figure 6.1.c shows the measured beam diameter for the CW excited disc with focal length 75 mm, and this corresponds to the calculations in Fig. 4.12.a. The measurements show a beam waist at depth 40 mm with diameter 2.9 mm. The calculations show a beam waist at 40 mm with diameter 2.7 mm. At depth 150 mm the measurements show a diameter of 8.2 mm, while the calculation gives 8.4 mm. At 20 mm the measured diameter is 8.2 mm and the calculated is 6.3 mm. Again the difference between the measured and calculated diameter is within 0.3 mm outside the beam waist and 1.0 mm inside the beam waist.

Finally, Fig. 6.1.d shows the measured beam diameter for the pulse excited disc with focal length 75 mm. This corresponds

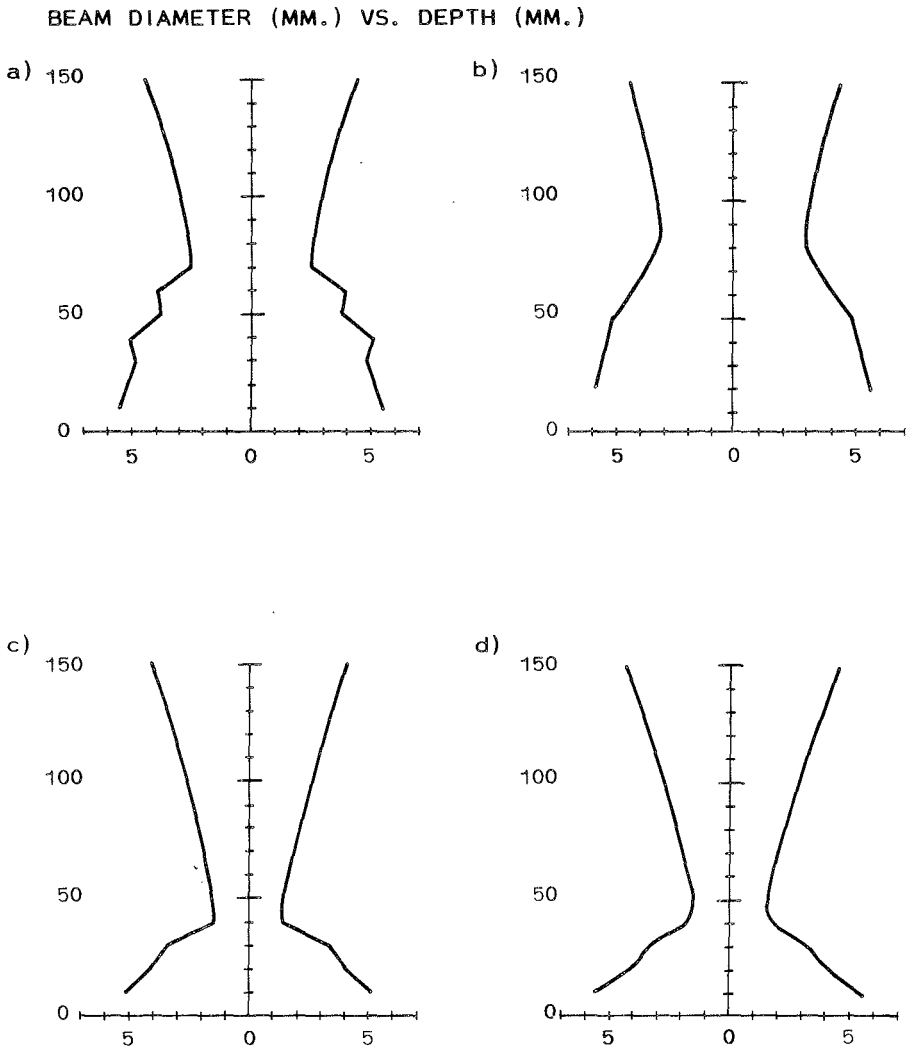

Fig. 6.1. Measurements of the beam diameter in mm as a function of depth in mm for the single element transducer with one matching layer. The aperture diameter is 12.7 mm and the centre frequency is 3 MHz.

a. Planar disc, CW excitation
b. Planar disc, pulse excitation
c. Focused disc, CW excitation
d. Focused disc, pulse excitation

to the calculations in Fig. 4.13.a. The measurement shows a beam waist at depth 50 mm with diameter 3.1 mm. Also the calculations give a beam waist at 50 mm, but with diameter 2.9 mm. At depth 150 mm the measured diameter is 8.9 mm, while the calculated is 8.8 mm. At depth 20 mm the measured diameter is 8.3 mm, while the calculated is 7.9 mm. In the latter case the difference between measured and calculated diameter is within 0.5 mm inside the beam waist.

The disagreements between measured and calculated diameters less than 0.5 mm are easy to account for. The hydrophone diameter is 1 mm and uncertainty in the position is 0.1 mm on each side of the beam. The calculations of diameter are based on a linear interpolation between the sampling points, and they are separated by 0.75 mm in the direction perpendicular to the axis.

Inside the beam waist the disagreements between measured and calculated diameter are larger than outside the beam waist. In general the measured diameters are larger than the calculated. Also the disagreements are larger for CW excitation than for pulse excitation. The reason is that the local peaks in the beam are not resolved with a 1 mm hydrophone and the measured peak values are too low. This gives too low a half value estimate and a larger half value diameter. The CW fields are more peaked than the pulsed fields and therefore show larger disagreements.

The latter statement is easier to discuss after showing the measured beam profiles. In Fig. 6.2 are shown the measured beam profiles for the CW excited disc with focal length 75 mm. The measurements are done as a function of distance from the axis in depths z equal to 20, 30, 50, 70, 100 and 150 mm. The corresponding calculations are shown in Fig. 4.12.c. The resolution in the calculations is 0.5 mm.

The generator voltage was kept constant during the measurements of the beam profiles at the different depths. We

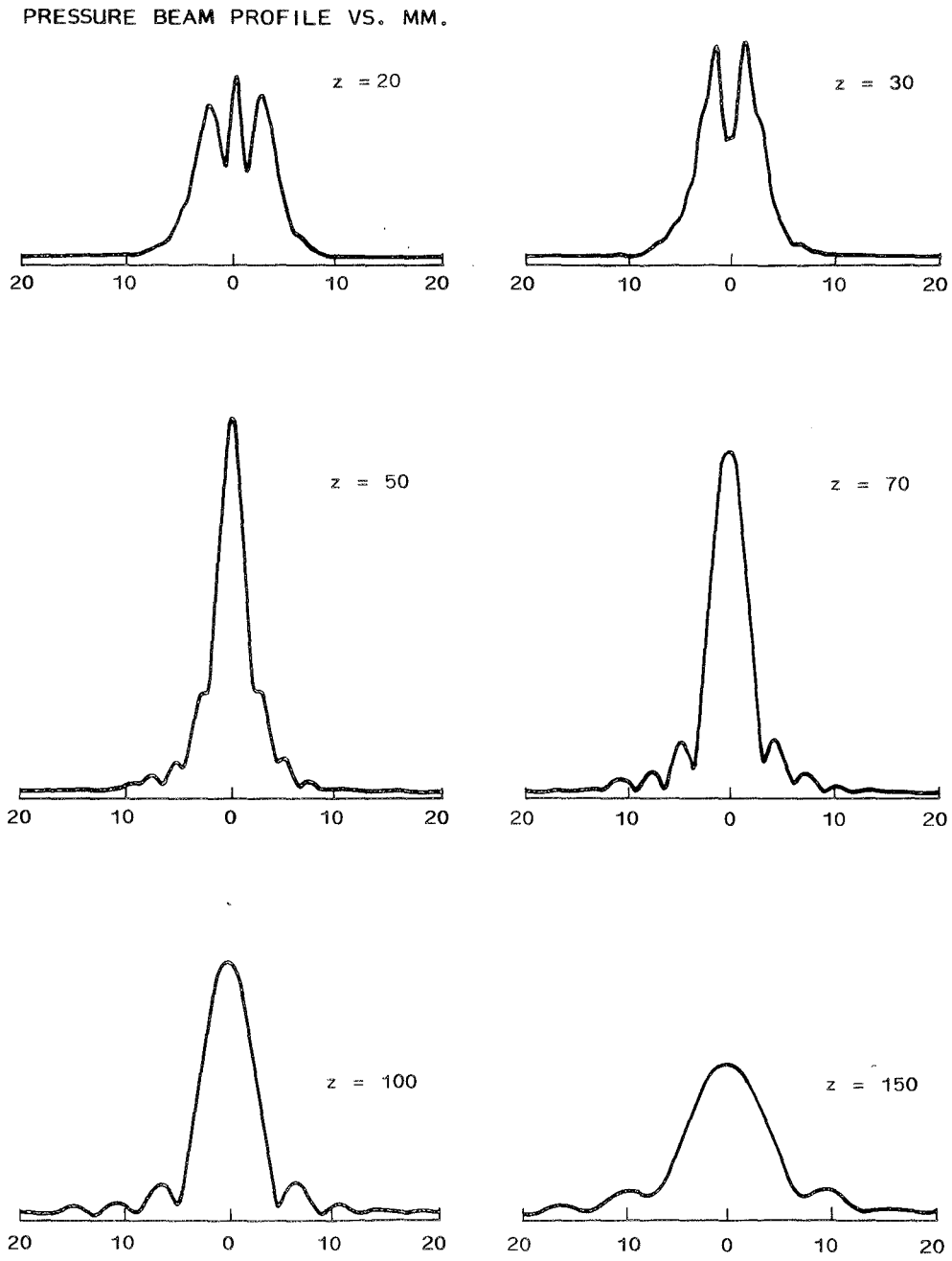

Fig. 6.2. Measured beam profiles as a function of distance from the axis in mm at distance z in mm from the aperture of diameter 12.7 mm and focal length of 75 mm. The excitation is a 3 MHz continuous signal.

can see that the spatial peak is at 50 mm which also is in agreement with the plot in Fig. 4.12.b.

All in all the agreement between the measured and the calculated beam profiles is very good. The differences occur at the peaks and at the dips and zeros. This can be due to the size of the hydrophone and the resolution in the calculations. The on-axis peak at depth 20 mm is about 50% higher in the calculated plot than in the measured plot. We can see however, that this is narrower than 1 mm and will therefore be unresolved by the finite hydrophone aperture. As discussed above, this will give too low a measurement of the peak value. It is easy to see when comparing the measured and calculated beam profile in this case, that the measured half value diameter will be too large. If the on-axis peak in the calculated beam profile is cut down to match the measured profile, we can read out that the half value diameter will become about 8 mm the measured value was 8.3 mm. This shows that the size of the hydrophone can explain the disagreement.

At depth 30 mm the calculation also shows an on-axis peak. This is not present in the measurements. However, the calculated peak is narrower than 1 mm and will therefore not be present in the measured beam profile. The same can be said about all the peaks in the profiles - they are not resolved by the hydrophone.

At depth 70 mm the dips in the calculated beam profile are deeper than in the corresponding measurement. Again, we can blame the size of the hydrophone.

It is very tempting to state that the hydrophone size is due to the non-resolved peaks and dips. However, we do not know if they really are present, so all we can say is that if the peaks and dips are there we would not be able to measure them anyway.

The agreement between the calculation and measurement is good, and by measuring the continuous fields we have achieved two things. First, we have gained confidence in our calculation model. Second, we have seen that a thin disc transducer vibrates like a piston when excited with a continuous signal.

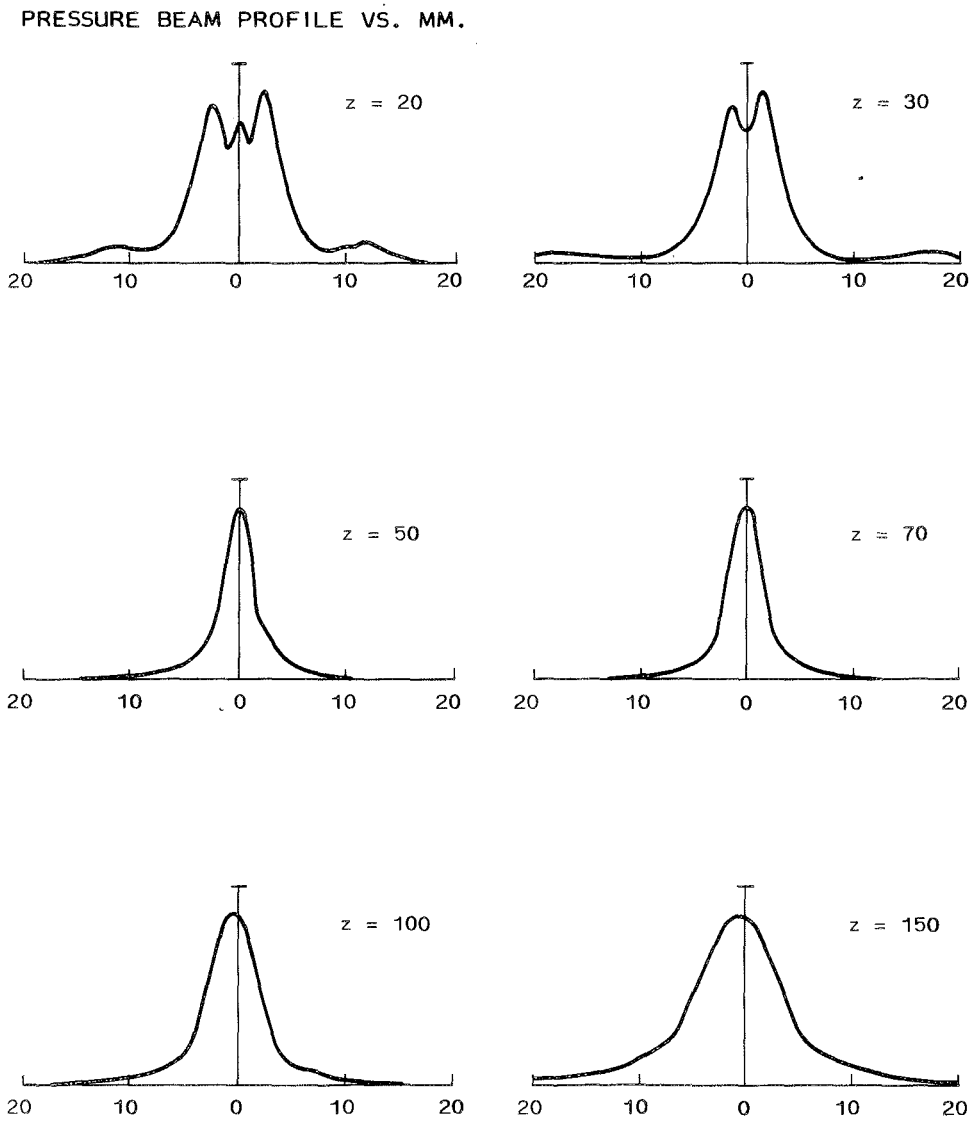

Fig. 6.3. Measured beam profiles as a function of distance from the axis in mm at distance z from the aperture in mm from a focused disc excited with a pulse. The aperture diameter is 12.7 mm, the focal length is 75 mm and the centre frequency is 3 MHz.

For echo imaging the transient field propagation is more important. In Fig. 6.3 are shown the measured beam profiles for the pulse excited disc with focal length 75 mm. By pulse excitation we now mean that the transducer is excited with a δ-pulse and the medium is excited with the pulse coming from a transducer with one matching layer. In Ch. 5 we saw that the measured and calculated transducer impulse responses were quite equal, and the calculated beam profiles in Fig. 4.13.c will therefore correspond to the measurements in Fig. 6.3.

At depth z equal to 20 mm both the calculated and measured beam profiles have three peaks. In the measurements, the on-axis peak is unresolved by the hydrophone. The off-axis peaks are higher in the measurements than in the calculation. At a distance 12 mm from the axis, the measurement shows a sidelobe which is not present in the calculation.

At depth 30 mm both the calculated and measured beam profiles have two peaks. The peaks in the measurements are higher than in the calculation. A sidelobe can be observed in the measurements at distance 18 mm from the axis, which is not present in the calculation.

From depth 50 mm and outwards, the beam profiles are single-peaked and decrease monotonically with distance from the axis. When the level of signal in the measurement is lower than about 3% of the on-axis level, it disappears in the noise and can not be measured.

The most obvious disagreement between the calculations and the measurements is the sidelobes at depths 20 mm and 30 mm. A more thorough investigation of the field shows that this sidelobe is due to a 1 MHz pulse radiating in a cone from the transducer. This radiation pattern is typical for a plate vibration [14], and is often called a Lamb wave [30]. We can see from the measured beam profiles that it radiates in an angle of 30 degrees relative to the axis. This indicates a propagation velocity along the disc equal to two times the

velocity in water or 3000 m/s. This mode of vibration may correspond to the resonance at 0.9 MHz in the measured electric input impedance of the transducer shown in Fig. 5.5.b. This resonance could not be seen in the transfer function in Fig. 5.4.d, which was measured with the hydrophone in the focal point. The radiation pattern of this mode explains why.

Other disagreements between the calculated and measured beam profiles may also be due to radiations from other modes of vibration. But only the above-mentioned plate mode has been detected separately. We know, however, that the pulse excitation of the transducer will excite all the modes in the transducer, and they may influence the radiation pattern.

6.2. The two-element transducer

In the calculations in Chapter 4 we used a total diameter of 12.7 mm for all the apertures. The diameter was kept constant so that we could easily compare the fields from the apertures. The fabricated two-element transducer which is described in Chapter 5 has a total aperture diameter of 13.7 mm, and for practical reasons it also has a distance of 0.25 mm between the inner disc and outer ring. The calculations of this particular aperture will therefore have to be presented here. We will concentrate on the echo imaging application and therefore use pulse excitation only.

The transducer is supplied with a silicone lens with focal length 55 mm. In Chapter 4 this was found to be the best fixed focal length for a two-element array.

There are two modes in which the transducer will be used. The first is the transmit mode, where the focal length is set to 75 mm. The second is the receive mode where the focal length is adjusted to match the depth of the incoming echo. The receive mode is called dynamic focusing. We will analyse these two modes separately.

In Fig. 6.4.a is shown the calculated beam diameter as a function of depth for the transmit mode. In Fig. 6.4.b is shown the measured beam diameter as a function of depth for the transmit mode. In both cases the beam waist is found at depth 50 mm, where both the calculation and the measurement gives a diameter of 2.8 mm. Outside the beam waist the difference between the calculated and measured diameter is less than 0.3 mm. The largest difference is found at depth 40 mm, where the measured diameter is 5.5 mm while the calculated diameter is 3.3 mm. At depth 20 mm the measured diameter is 1.5 mm while the calculated diameter is 2.0 mm. We also note that this is much less than the corresponding diameter in Fig. 4.29.a, where we had 5.3 mm at depth 20 mm. In that case the diameter was 12.7 mm and there was no space in between the elements.

In Fig. 6.5 are shown the calculated beam profiles for the two-element transducer in transmit mode for depths z equal to 20, 30, 50, 70, 100 and 150 mm. The corresponding measurements are shown in Fig. 6.6. At depth 20 mm the calculation shows a sidelobe which is about 40% of the on-axis peak value, while the measurements show a sidelobe which is about 30% of the on-axis peak value. At depth 30 mm we can see that the calculated profile is single peaked and has a indentation in the flank. The measurement at 30 mm has a double peak and shows no sign of the indentation. From depth 50 mm and outwards the agreement between the calculations and the measurements is much better. No important differences can be seen outside the beam waist, but inside the beam waist the differences are obvious.

The measurements of the electric input impedance of the two-element transducer in Chapter 5 showed many resonances in the structure. These modes of vibration may radiate into the medium and in particular influence the near field.

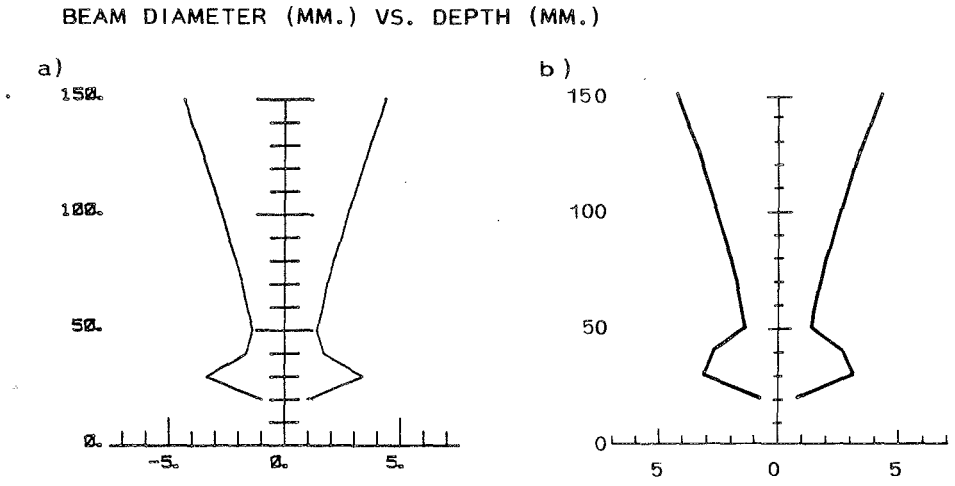

Fig. 6.4. Beam diameter in mm as a function of depth in mm for the two-element transducer with one matching layer in transmit mode. The aperture diameter is 13.7 mm, the total focal length is 75 mm and the fixed focal length is 55 mm. The centre frequency is 3 MHz.

a. Calculation
b. Measurement

In the previous section we identified a plate mode that radiated in a cone from the single element transducer. No similar mode has been detected for the two-element transducer. This may be due to the discontinuity represented by the space between the elements. No other modes can be seen separately in the field either. It is most likely that there are other modes present in the field anyway, but just obscuring the field as we have seen in the measurements.

In the calculations of the field from the two-element aperture, it is assumed that the area in between the centre disc and the outer ring does not vibrate at all. The filled epoxy that forms the matching layer is, however, connected and also fills up the space between the two piezoelectric elements. This causes a more continuous change in the vibration pattern between the two elements for the measured transducer. The indentation in the flank of the calculated

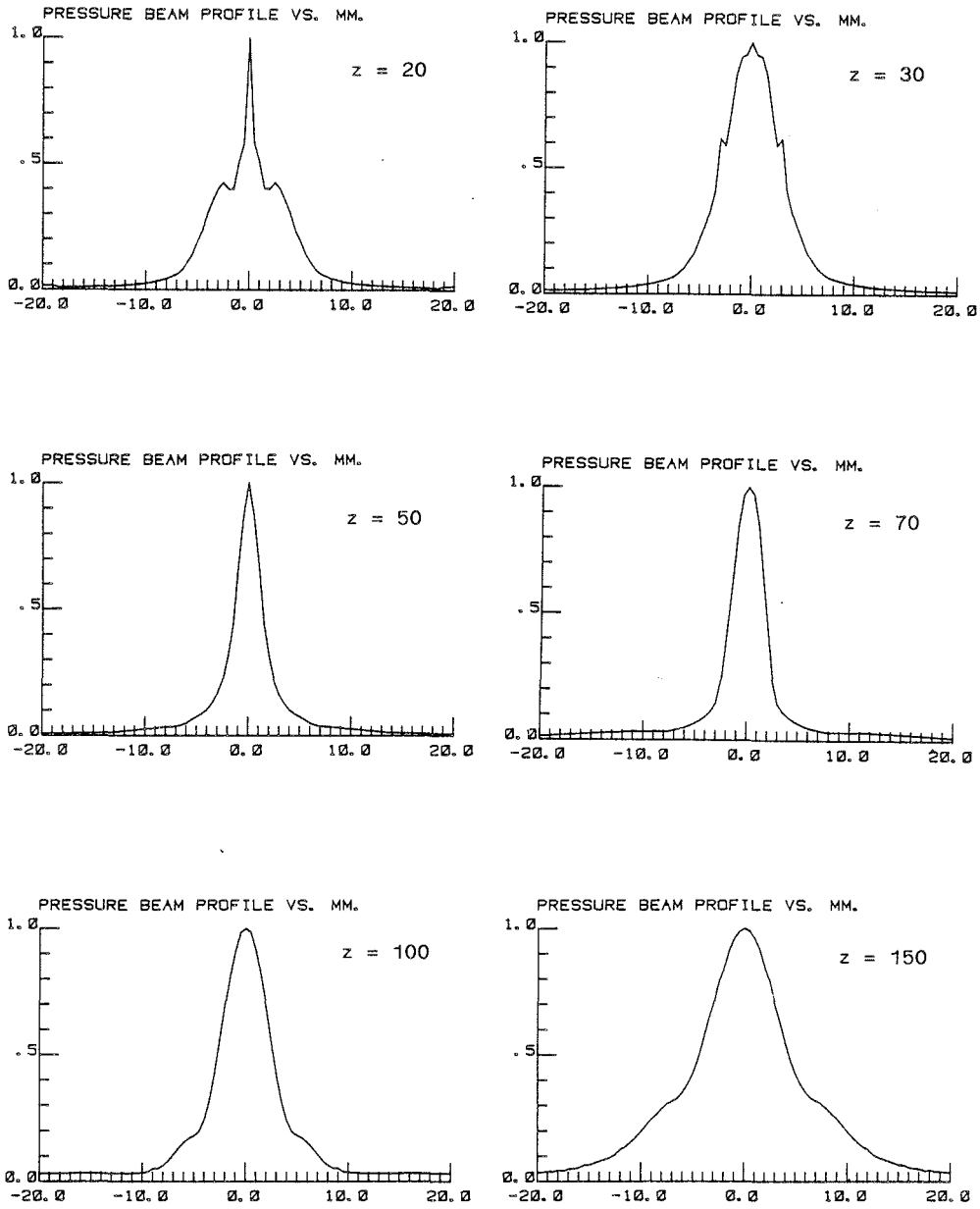

Fig. 6.5. Calculated beam profiles as a function of distance from the axis in mm depth z in mm the two-element transducer with one matching layer in the transmit mode. The aperture diameter is 13.7 mm, the total focal length is 75 mm and the fixed focal length is 55 mm. The centre frequency is 3 MHz.

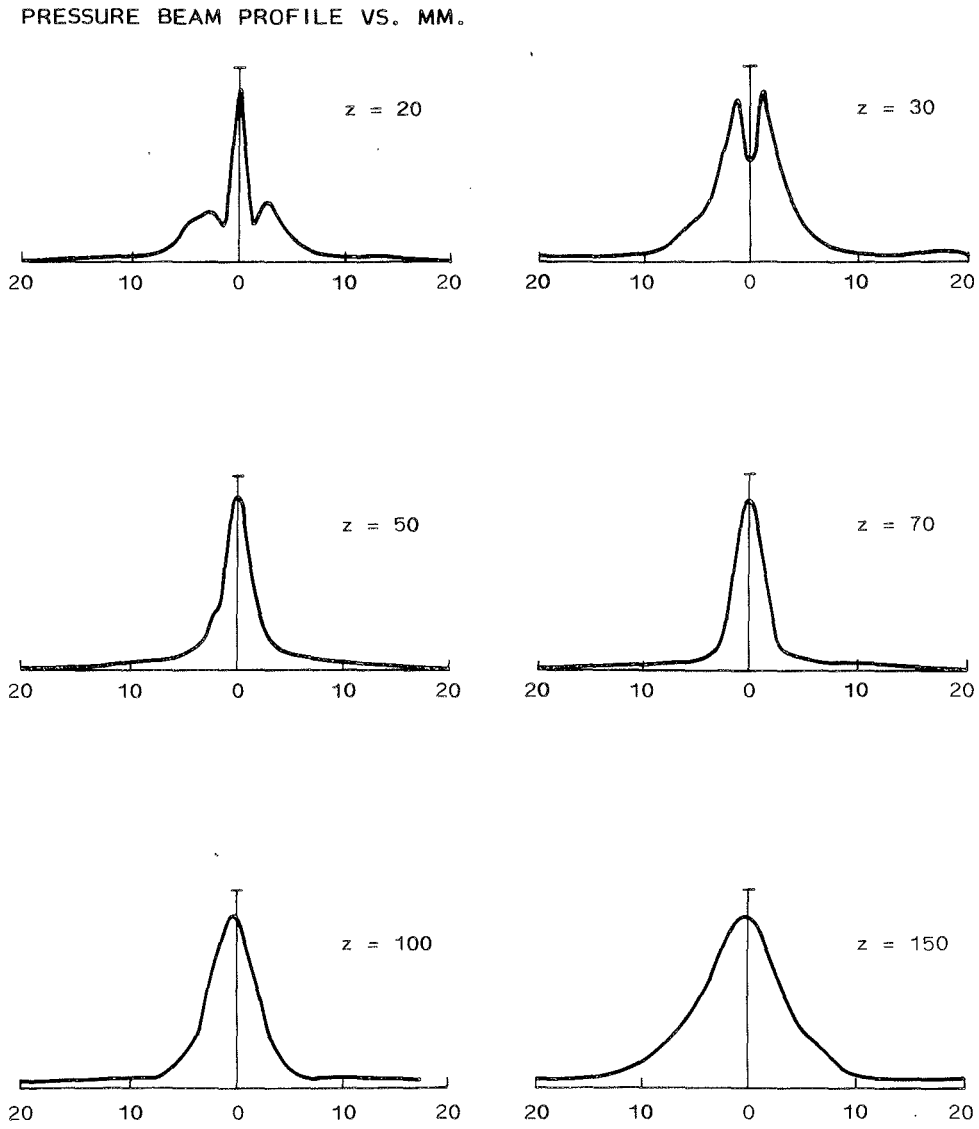

Fig. 6.6. Measured beam profiles as a function of distance from the axis in mm at depth z in mm for the two-element transducer with one matching layer in the transmit mode. The aperture diameter is 13.7 mm, the total focal length is 75 mm and the fixed focal length is 55 mm. The centre frequency is 3 MHz.

beam profile at depth 30 mm can be traced back to the discontinuity in the aperture. If we look back to Fig. 4.29.c we can see that the calculated beam profile at depth 30 mm has a double peak and no indentation. There the calculations were done without taking any space between the elements into account. This calculation is in better agreement with the measurement in Fig. 6.6 at depth 30 mm than was the case for the calculation in Fig. 6.5. However, at depth 20 mm the calculation in Fig. 4.29.c shows a sidelobe which is over 50% of the on-axis value. This is in worse agreement with the measurement in Fig. 6.6 than was the case for the calculation in Fig. 6.5. This shows that our simplified model of the vibration pattern on the aperture is the reason for some of the errors in the near field.

Dynamic focusing is used to find the field for the two-element transducer in the receive mode. This means that the total focal length always is equal to the depth. Actually both the calculations and the measurements are done with a transmitting transducer, but due to reciprocity this makes no difference.

In Fig. 6.7.a is shown the calculated beam diameter as a function of depth for the two-element transducer in the receive mode. In Fig. 6.7.b is shown the corresponding measurement. The difference between the calculated and measured beam diameter is less than 0.3 mm for all depths except at 20 mm. At depth 20 mm the measured diameter is 1.5 mm while the calculated diameter is 1.8 mm. We also note that the calculated diameter is larger at 20 mm than it is at 30 mm where it is 1.6 mm.

In Fig. 6.8 are shown the calculated beam profiles for the two-element transducer in the receive mode for depths z equal to 20, 30, 50, 70, 100 and 150 mm. The time delay to the elements is controlled so that the focal length is equal to the depth in all the plots. Fig. 6.9 shows the corresponding measurements. At depths 20 and 30 mm the shape of the calculated skirts and the measured skirts are different. The

level is, however, about the same size. At depths 50 and 70 mm both the calculated and measured beam profiles decrease monotonically with distance from the axis. But the level of the skirts in the measurements is about twice of that in the calculations. At depths 100 and 150 mm the skirts are somewhat different in shape for the calculations and the measurements, but more important is the fact that the level of the skirts is about 50% higher in the measurements than in the calculations. We also note that the measured beam profiles are slightly asymmetric.

The same beam profiles as in Fig. 6.5 and Fig. 6.6 are shown in dB-scale in Fig. 6.10. Here the measurements and the calculations are plotted together. The information is of course the same, but here it is easier to see the skirts. The beam profiles from Fig. 6.8 and Fig. 6.9 are also repeated in dB-scale in Fig. 6.11.

The discussion following the presentation of the transmit field is valid also for the receive field. In addition to this we also have the influence of the cross-coupling between the elements and the errors caused by the differences between the pulses from the two elements.

Successful dynamic focusing requires that the elements radiate independently and that the pulses from the elements are identical. This will never be absolutely true in practice. A large cross-coupling between the elements will damage the possibility of controlling the focal length. The measurements show, however, that the focal length is under control. But even a weak cross-coupling can influence the pulse from an element due to the excitation it gets when the neighbour element is excited.

The idea of dynamic focusing is that the fields from the different elements will interfere constructively in some regions of space and destructively in others. If, however, the pulses coming from the different elements are different in some way, a total cancellation is not possible. A difference

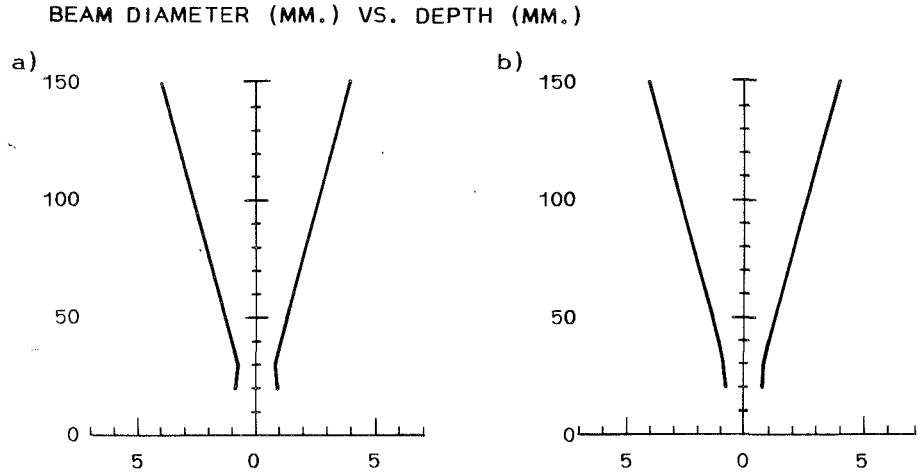

Fig. 6.7. Beam diameter in mm as a function of depth in mm for the two-element transducer with one matching layer in recieve mode. The aperture diameter is 13.7 mm, the fixed focal length is 55 mm and the centre frequency is 3 MHz.

a. Calculations
b. Measurement

in the two pulses from our transducer will therefore be seen as an increased level of the skirts. This is just what we have observed. It is therefore necessary for a successful array design that the impulse responses are equal for all the elements and that the cross-coupling is low.

In Fig. 6.12 are shown both calculations and measurements of the pressure along the acoustic axis for the transmit and the recieve mode. We can see that the spatial peak is at 50 mm in the transmit mode, which is in agreement with earlier calculations and measurements. For the recieve mode we can see that the on-axis pressure increases towards the aperture until 30 mm. Ideally the on-axis pressure should have followed a hyperbolic function when dynamic focusing is used. This breaks down at about 30 mm, but still the pressure at 20 mm is much higher in recieve mode than in transmit mode.

The curves in Fig. 6.12 are set equal at depth 75 mm. Comparing the calculations and measurements we can observe some disagreement in the near field. For the transmit mode the measured values are lower than the calculated values. This is in agreement with the unresolved on-axis peaks due to the hydrophone aperture as mentioned earlier. However, for the recieve mode the measurements are larger than the calculations. At the depth 20 mm in recieve mode we have observed earlier in Fig. 6.7 that the beam diameter is narrower in the measurements than in the calculations. These two observations are in agreement with each other. The reason for this effect might be other modes of vibration apart from the piston mode which obscures the near field.

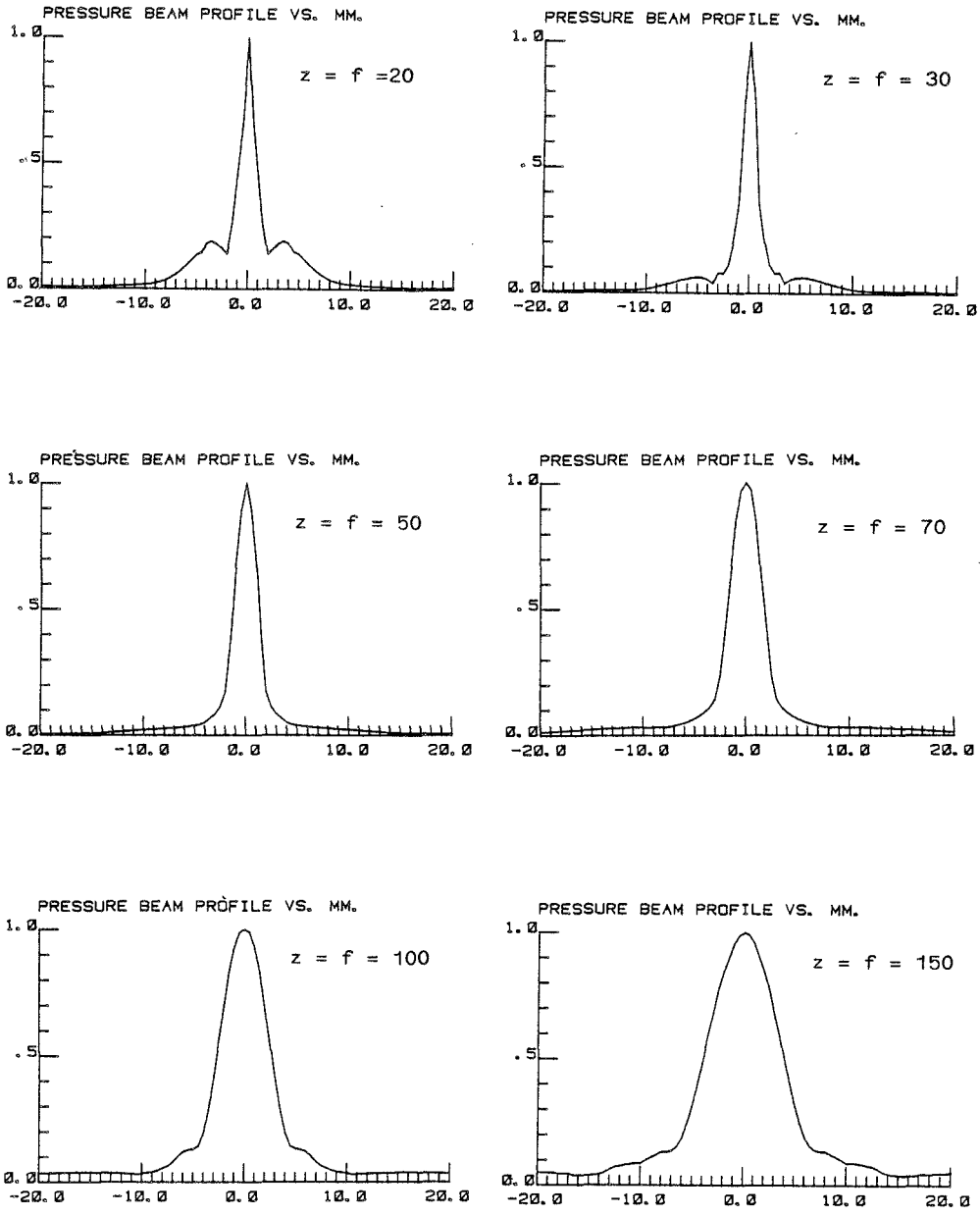

Fig. 6.8. Calculated beam profiles as a function of distance from the axis in mm at depth z in mm for the two-element transducer with one matching layer in receive mode with focal length f. The aperture diameter is 13.7 mm, the fixed focal length is 55 mm and the centre frequency is 3 MHz.

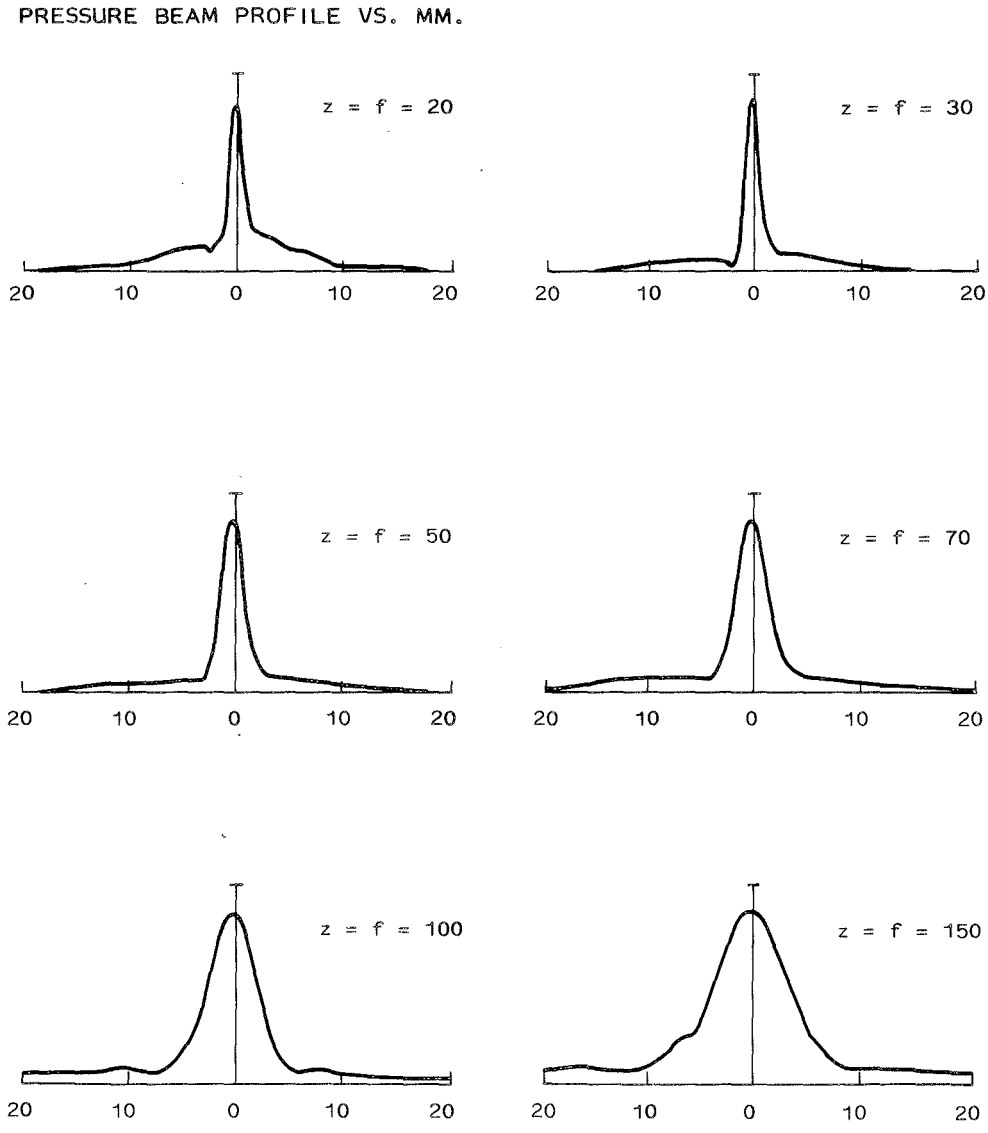

Fig. 6.9. Measured beam profiles as a function of distance from the axis in mm at depth z in mm for the two-element transducer with one matching layer in receive mode with focal length f. The aperture diameter is 13.7 mm, the fixed focal length is 55 mm and the centre frequency is 3 MHz.

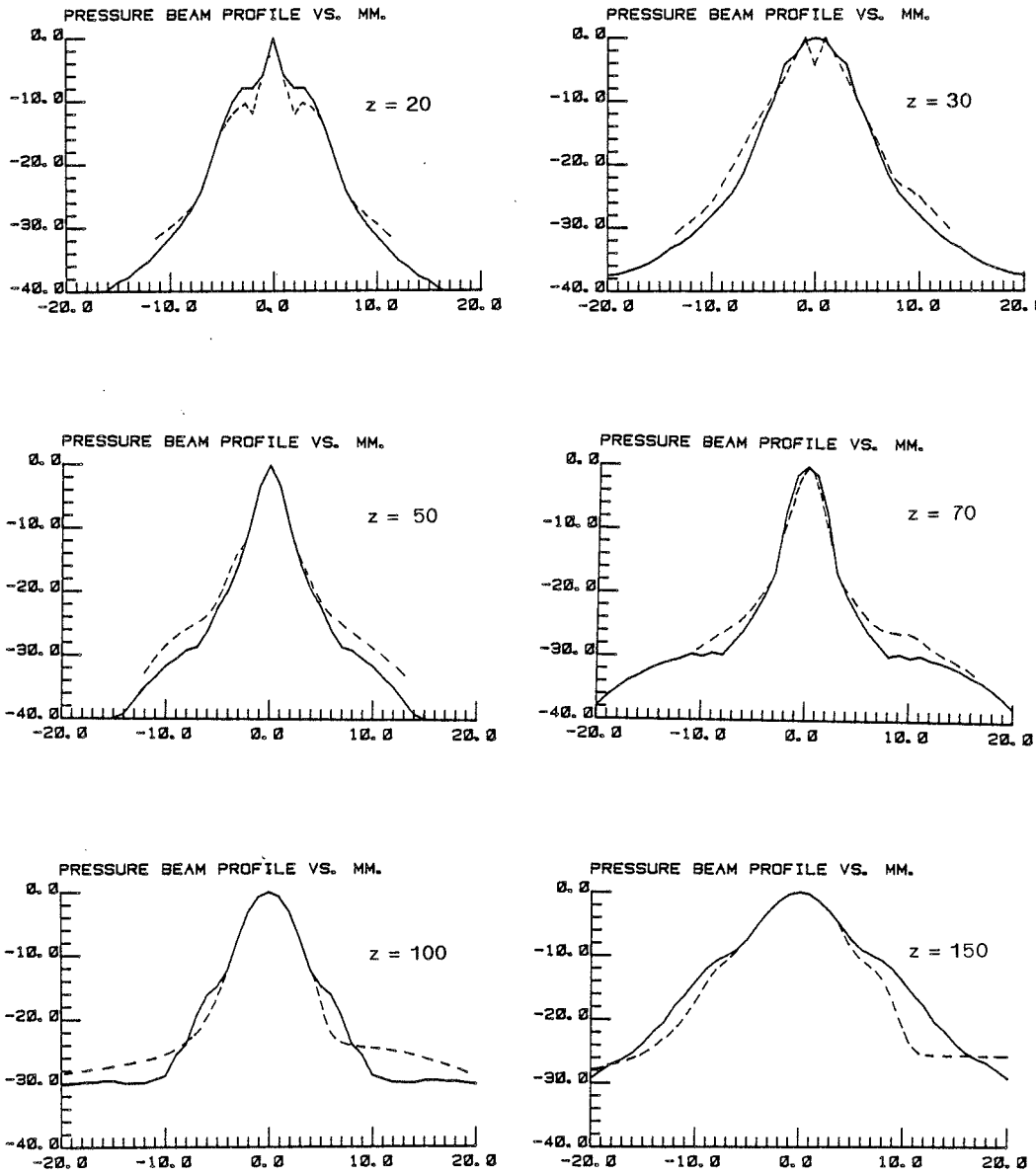

Fig. 6.10. Measured (-----) and calculated (————) beam profiles in dB-scale as a function of distance from the axis in mm at depth z in mm for the two-element transducer with one matching layer in the transmit mode. The aperture diameter is 13.7 mm, the total focal length is 75 mm and the fixed focal length is 55 mm. The centre frequency is 3 MHz.

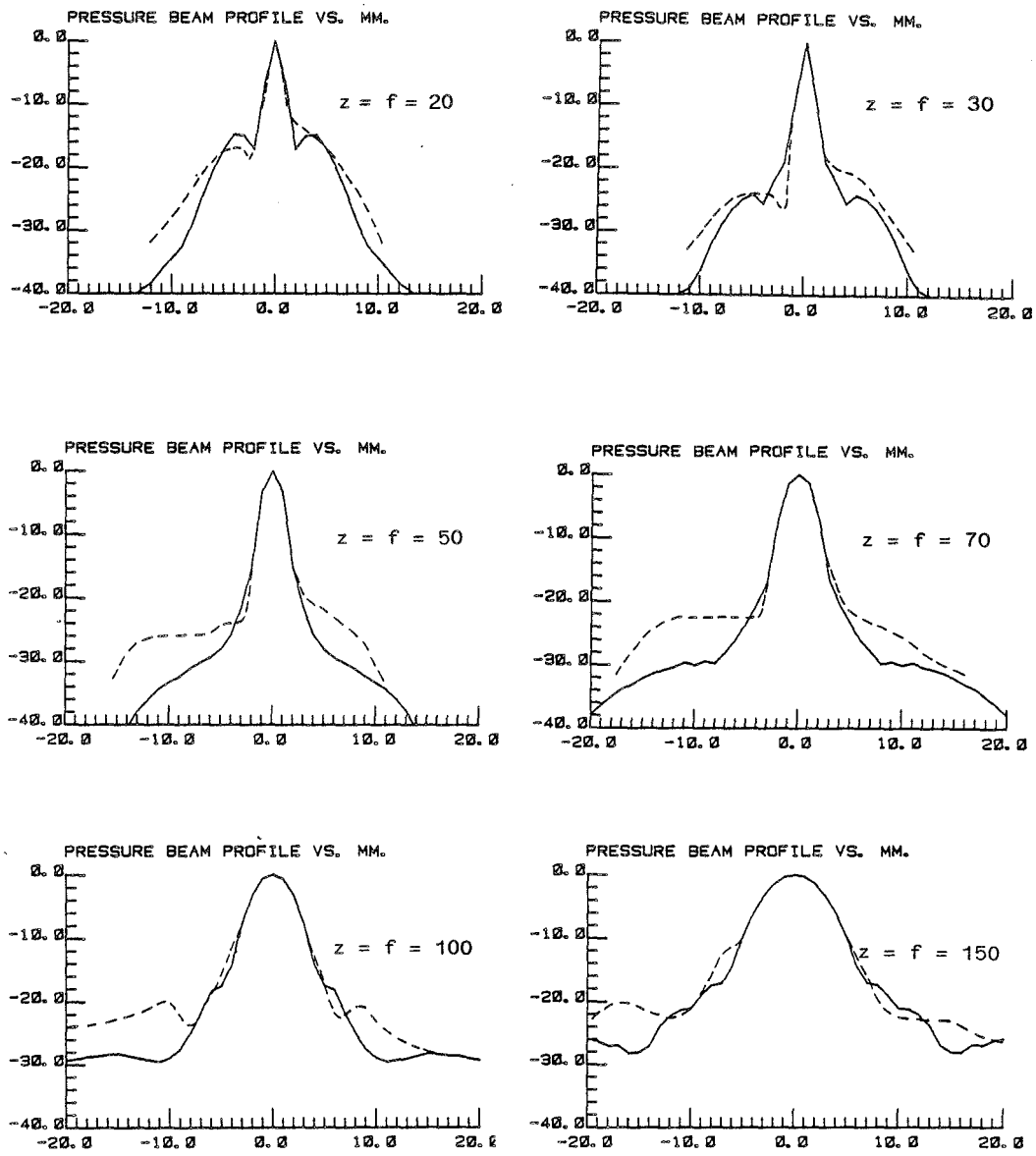

Fig. 6.11. Measured (-----) and calculated (————) beam profiles in dB-scale as a function of distance from the axis in mm at depth z in mm for the two-element transducer with one matching layer in the receive mode with total focal length f. The aperture diameter is 13.7 mm and the fixed focal length is 55 mm. The centre frequency is 3 MHz.

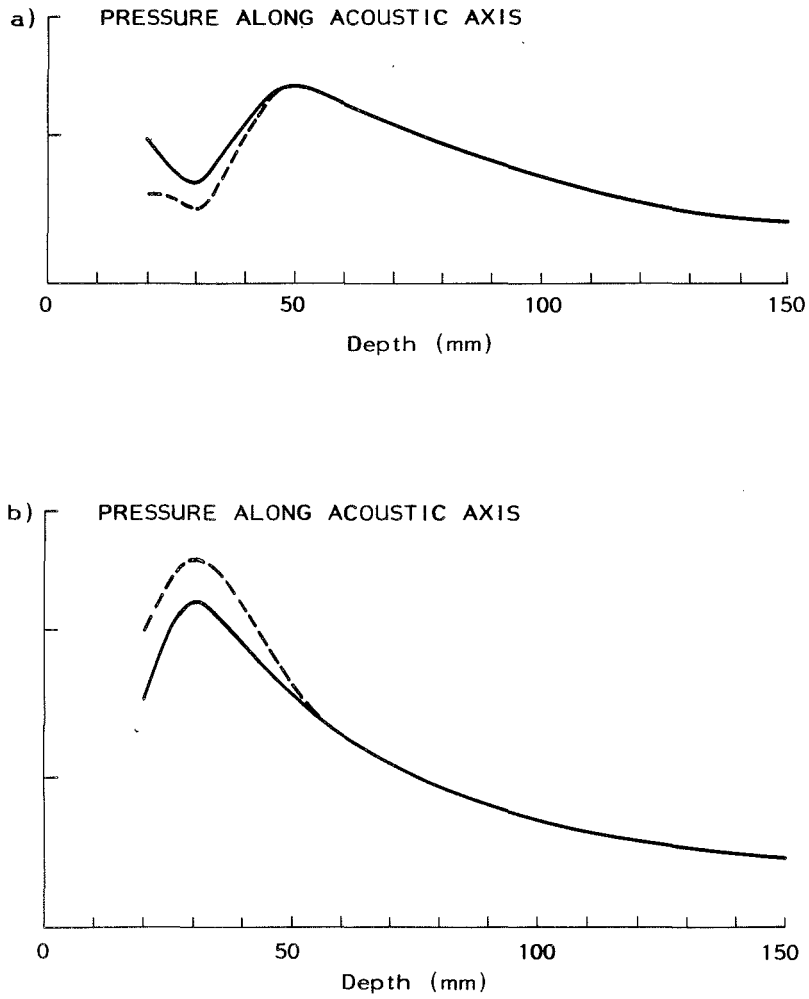

Fig. 6.12. Measured (- - - - -) and calculated (————) pressure along acustic axis for the two-element transducer with one matching layer. The aperture diameter is 13.7 mm and the fixed focal length is 55 mm. The centre frequency is 3 MHz.

a) Transmit mode
b) Recieve mode

7. CALCULATIONS AND MEASUREMENTS OF THE ECHO RESPONSE

In Section 2.3 we developed the expression for the echo response. This is found in Eq. (2.34)

$$i(t) = A\varrho^2 \frac{\partial^2}{\partial t^2} u(t)*h(t)*h(t)*g(t)*g(t)*s(t) \qquad (7.1)$$

Where i(t) is the current in the electric load impedance during reception. If the load impedance during reception is different from the generator impedance during transmission, we must remember that this also gives us different transducer transfer functions. This is no limitation, it only implies that the transducer transfer function has to be calculated twice. We will in the calculations and the measurements use a 50 Ω line connected to the transducer for both transmission and reception. The calculated and measured quantity will be the output voltage, e(t), found from

$$e(t) = R\, i(t) \qquad (7.2)$$

where R is the transducer load.

The expression for the echo response includes the object function, s(t). To get an expression for this object function, we had to introduce two simplifications. The first was to assume that the waves are planar. The second was that the object is planar. This gives us the possibility of using the formulas from plane wave theory to find the reflection coefficient, C(ω). And the connection was found in Eq. (2.37):

$$s(t) = \frac{1}{\varrho c} \frac{1}{2\pi} \int_{-\infty}^{\infty} C(\omega) e^{j\omega t}\, d\omega \qquad (7.3)$$

The first assumption is questionable for an object in the near field, but the second assumption can be accounted for by choosing test objects that are planar. For such objects we recall that the total echo response could be found by summing

the response from small elements of the object. This is also what we will do in the calculations.

Our aim here is not to make good models for the real objects, but to make a good model of the echo imaging system. We will therefore need models of objects that can reveal the essential features of the echo imaging system. Two such objects have been selected. The first is a planar interface between water and teflon perpendicular to the acoustic axis. This gives us a single reflection which can be regarded as the system echo response. The second object is a thin sheet of PVC-plastic. This object will be used to test the depth resolution.

In this chapter we will use only the focused single element transducer. This is due to the fact that the electronics for dynamic focusing in real time are not available at the present time. The use of the single element transducer will, however, give us a good test of the echo response model. And also, the dynamic focusing will primarily improve the transversal resolution, and this can only be tested when the whole imaging system is working. This is not the case at the present time.

The calculations of the output voltage from the transducer or the echo response when the object is a planar impedance interface, are shown in Fig. 7.1

With a planar impedance interface we mean an object that fills up the entire half space behind a certain depth and that the interface is perpendicular to the acoustic axis. The chosen depths are z equal to 20, 30, 50, 70, 100 and 150 mm.

We can see from the plots in Fig. 7.1 that the echo responses are quite equal at all depths, and they are mainly an autoconvolution of the transducer impulse response. The most obvious difference is that the echo responses at 20 and 30 mm are stretched out in the beginning of the pulse. The distance from the very first positive peak to the peak value is 0.9 μs at depth 20 mm, while the same distance is 0.7 μs at depth 150 mm. This must be due to the influence of the spatial impulse response.

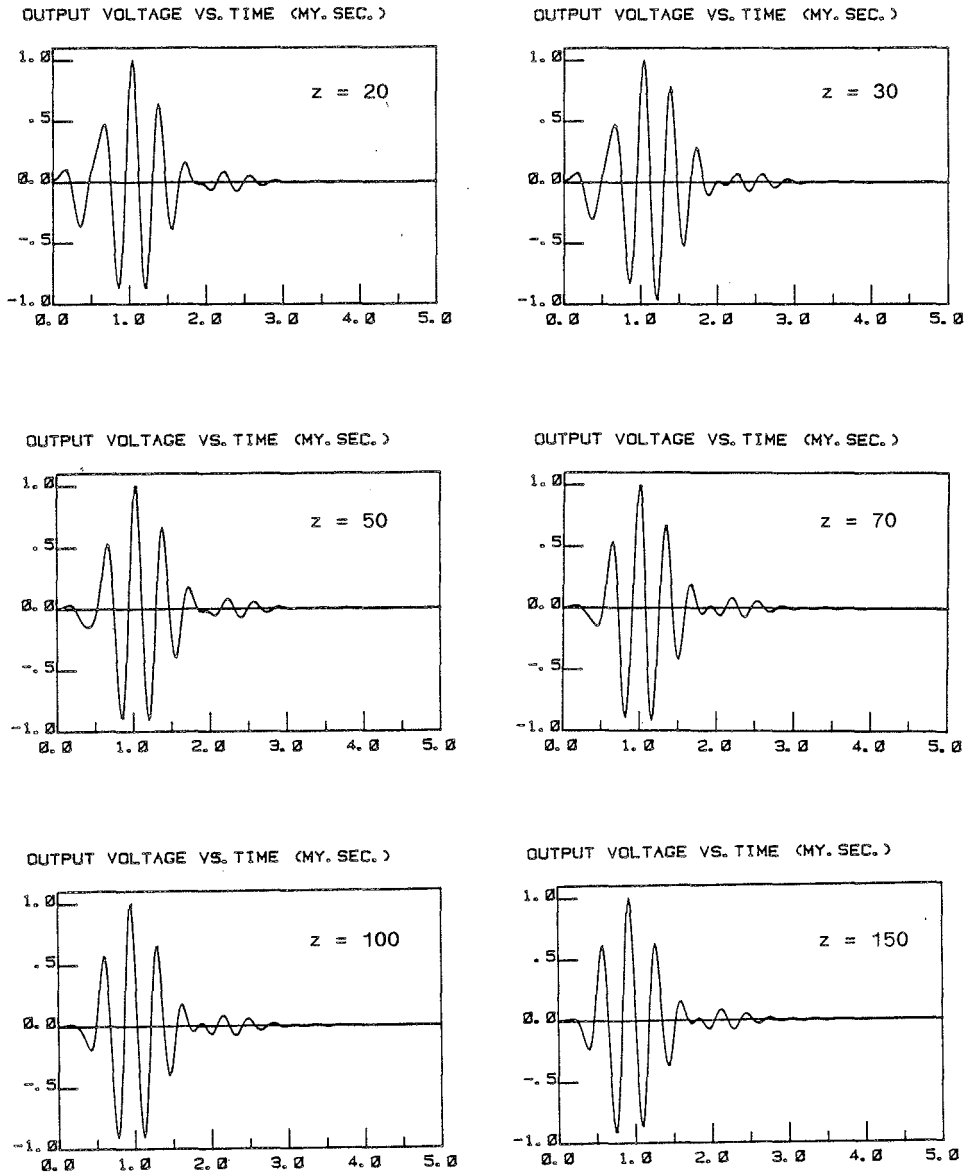

Fig. 7.1. Calculations of the output voltage from the single element transducer as a function of time when the object is a planar impedance interface perpendicular to the acoustic axis at depth z in mm. The aperture diameter is 12.7 mm, the focal length is 75 mm and the centre frequency is 3 MHz.

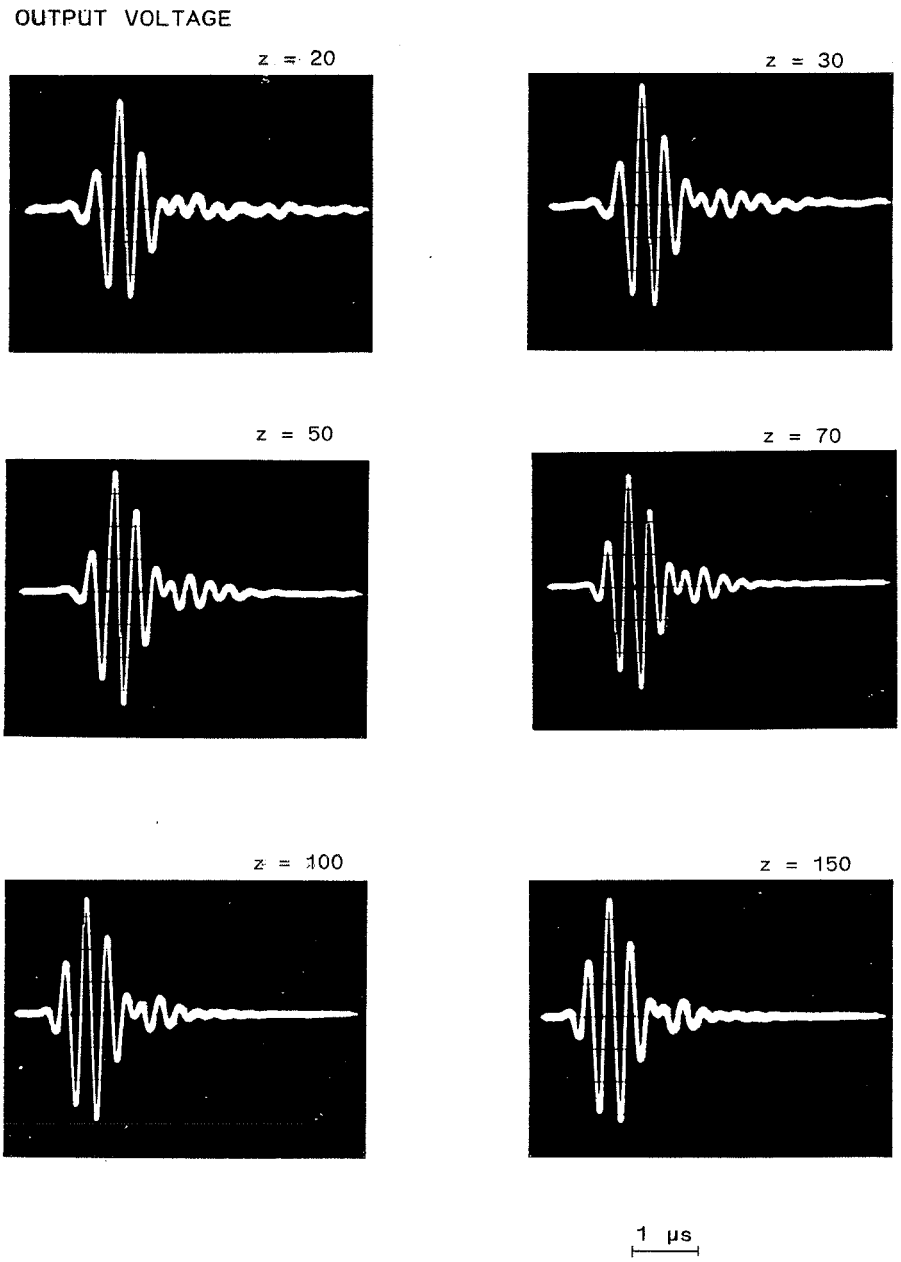

Fig. 7.2. Measurements of the output voltage from the single element transducer as a function of time when the object is a planar impedance interface perpendicular to the acoustic axis at depth z in mm. The aperture diameter is 12.7 mm, the focal length is 75 mm and the centre frequency is 3 MHz.

The echo response is a convolution of the autoconvolution of the transducer impulse response and the autoconvolution of the summation of spatial impulse responses.

The summation of the spatial impulse responses in a certain depth will in general have a peak value due to the on-axis response and a decay due to the off-axis responses. Around focus and in the far field the spatial response will be a sharp peak compared to the transducer response. The echo response will therefore be close to the autoconvolution of the transducer response which of course is the same at all depths.

In the near field the length of the spatial response will be of the same order as the length of the transducer response. The convolution will therefore give a more stretched echo response, just as we have observed.

The 12 dB pulse length of the calculated echo response is 1.3 μs at 20 mm and 1.1 μs at 150 mm. The increase of the pulse length by 0.2 μs at depth 20 mm is all due to the stretching in the beginning of the pulse.

We also observe a distinct tail on the calculated echo response at 1.3 μs behind the main peak. This tail is -22 dB relative to the peak and the same at all depths. The distinct tail must be due to the tail of the transducer response.

The measurements of the echo response from a single impedance interface are shown in Fig. 7.2. The object is a cylinder of teflon with diameter and length equal to 50 mm. The front end of the cylinder is used as the echo object. The reflection from the rear end of the cylinder is attenuated with more than 100 dB in the 100 mm teflon path. The object is also large enough to cover all of the focused beam.

We can see in Fig. 7.2 that the measured echo responses are quite equal to the calculated ones. The stretching of the pulse in the near field can be observed here too. The

distance from the very first positive peak to the main peak is 0.9 μs at depth 20 mm, and 0.7 μs at 150 mm. This is in good agreement with the calculated results.

The 12 dB echo pulse length at 150 mm is measured to be 1.1 μs which equals the calculated result. At depth 20 mm the measurement shows a 12 dB pulse length of 1.0 μs, while the corresponding calculation gave us 1.3 μs. A closer inspection of the pulses shows that the first negative peak of the pulse is much smaller in the measurement than in the calculation. In the measurement this peak is lower than 12 dB and therefore reduces the 12 dB pulse length. This large first negative peak can be seen in the calculations at 20 and 30 mm and is not in agreement with the corresponding measurements. This error may be due to our assumption of a plane wave in the calculations of the echo response. In the near field of a focused transducer, this assumption may be too simple.

In the measurements we can see that the tail of the pulse is about -19 dB relative to the main peak. This is 3 dB higher than calculated. The tail is a consequence of the tail in the transducer impulse response. This was measured in Chapter 5 and also there the tail was found to be higher than calculated. A higher tail in the measurements than in the calculations of the echo response could therefore have been expected.

Also it should be mentioned that the measurements of the echo response at 20 and 30 mm are disturbed by electric ringing. Details in the pulse should therefore not be taken into account.

To test the depth resolution of the imaging system we will use a 1.6 mm thick sheet of PVC. PVC has a velocity of 2500 m/s and this thickness will therefore correspond to 1 mm biological tissue which has a velocity of 1500 to 1600 m/s. Our requirement for the depth resolution was 1 mm in biological tissue.

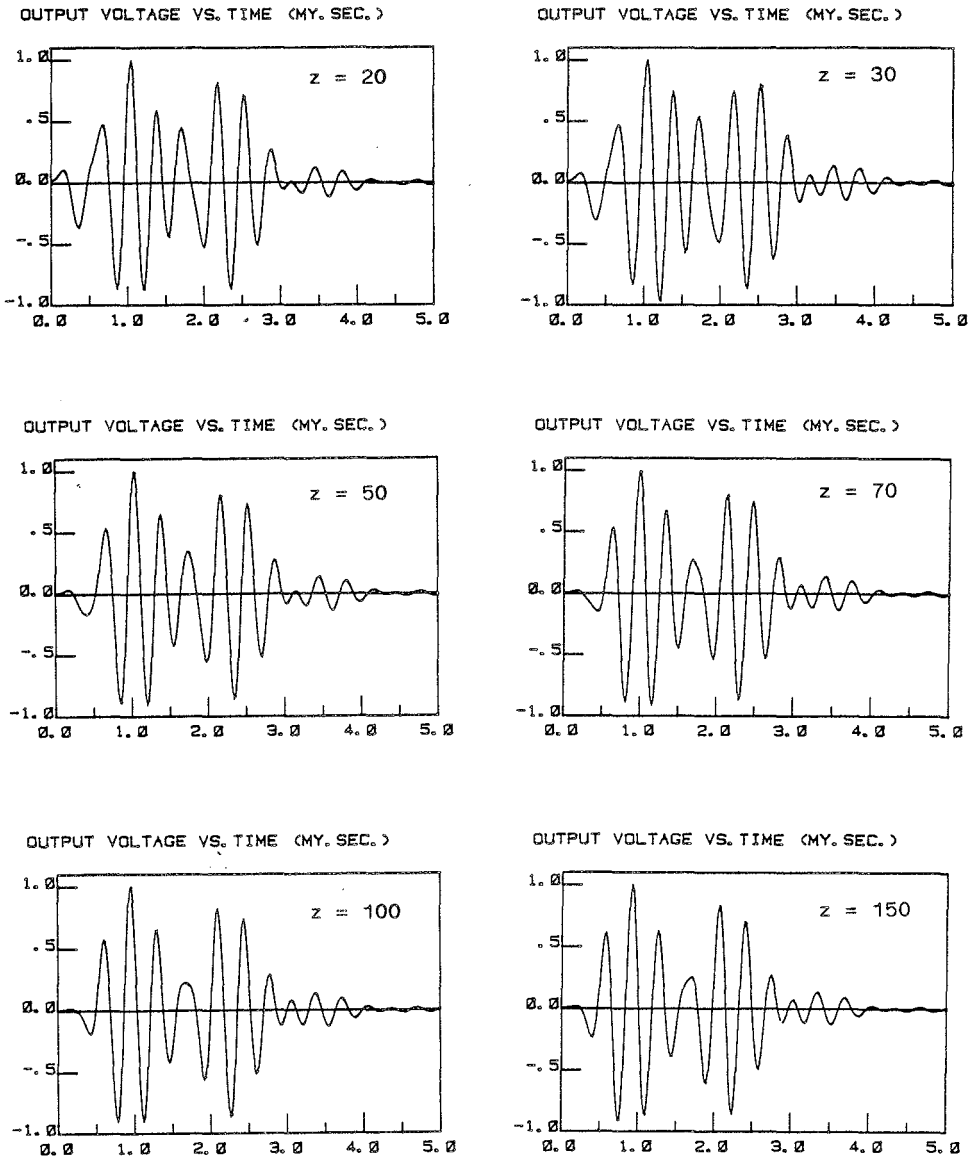

Fig. 7.3. Calculations of the output voltage from the single element transducer as a function of time when the object is a planar double impedance interface perpendicular to the acoustic axis at depth z in mm. The aperture diameter is 12.7 mm, the focal length is 75 mm and the centre frequency is 3 MHz.

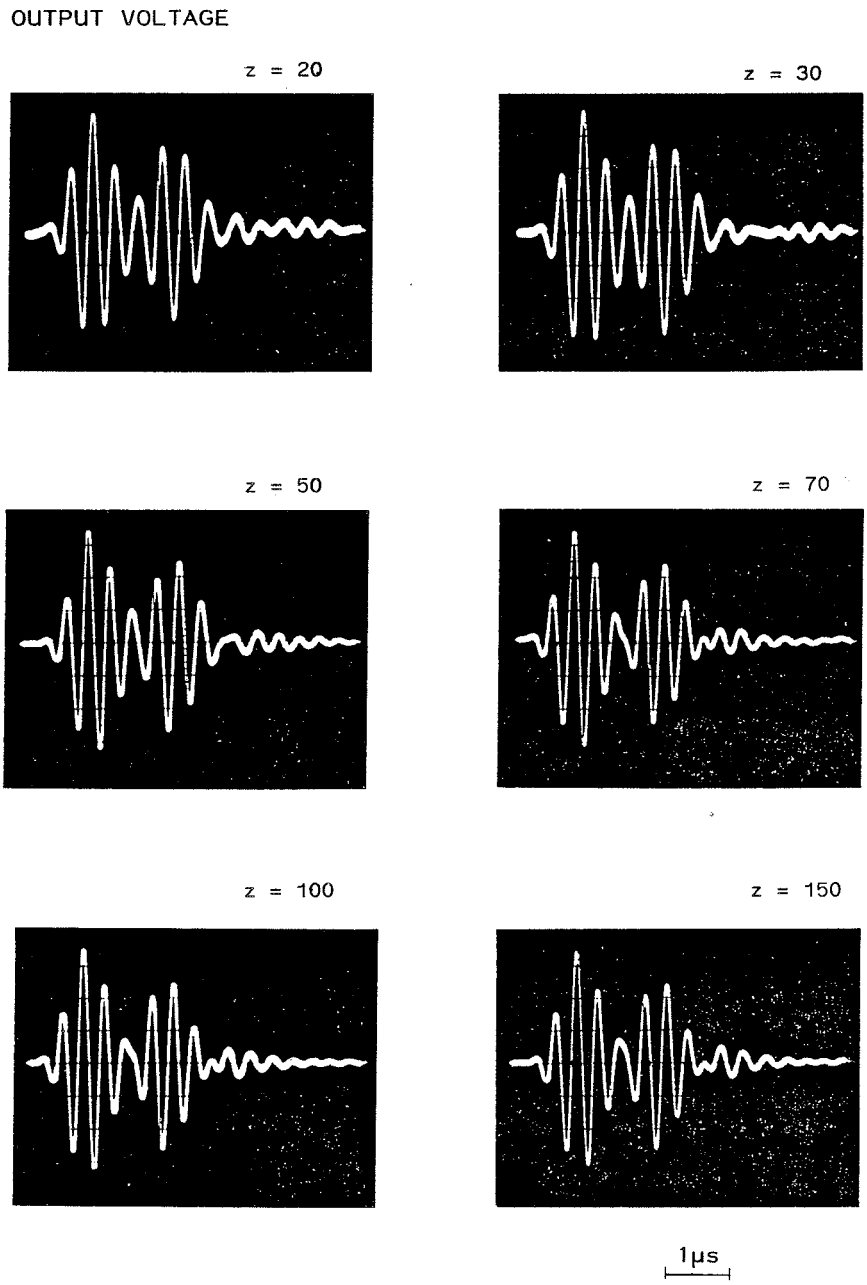

Fig. 7.4. Measurements of the output voltage from the single element transducer as a function of time when the object is a planar double impedance interface perpendicular to the acoustic axis at depth z in mm. The aperture diameter is 12.7 mm, the focal length is 75 mm and the centre frequency is 3 MHz.

Hva med off-axis måling?

The calculations of the output voltage or the echo response for the double interface object, are shown in Fig. 7.3. The object is 1.6 mm thick, has a velocity of 2500 m/s and an impedance of 3.6 Mrayl. It is placed perpendicular to the acoustic axis at depth z equal to 20, 30, 50, 70, 100 and 150 mm.

We find that the echo response from the sheet in general consists of two pulses separated in time by 1.3 μs. The second pulse is the negative of the first pulse. The first pulse comes from the first impedance interface with a positive reflection coefficient and the second pulse comes from the second interface with a negative reflection coefficient. The double pulse is mainly a superposition of these two pulses, but also multiple reflections are involved.

Whether the two pulses are resolved or not, depends on the detector. Let us assume a simple envelope detector and that the resolution criterium is that the envelope should fall below 50% of the peak value between the pulses. In this case we can see that the two pulses are not resolved at 20 and 30 mm, but are resolved at 50, 70, 100 and 150 mm.

The measurements of the echo responses from the PVC sheet are shown in Fig. 7.4. The general impression is the same as for the calculations. The echo response consists of two pulses, the second pulse is the negative of the first pulse. The distance between the pulses is 1.3 μs in agreement with the calculations. The measurements show that the response is mainly a superposition of the response from the front and the back of the sheet. In the measurement we can see that the second pulse is more attenuated relative to the first pulse compared with the calculations. This is due to the losses in PVC, which are not included in the calculation model.

Using the same criterion for resolution as in the calculations, we can see that the two pulses are resolved at all depths. In the calculations this was not true for depths

20 and 30 mm. The reason for this is that the measured pulses are shorter than the calculated pulses, as we saw for the single interface object.

With an envelope detector and the chosen resolution criterion, it is possible to resolve two impedance interfaces separated by 1 mm in biological tissue.

The envelope detector is however not very sophisticated. We have seen from both the calculations and the measurements that the echo response from a planar impedance interface is mainly an autoconvolution of the transducer impulse response. We are therefore faced with the problem of detecting a known signal in noise. To detect the impedance interface, which is the goal in echo imaging, we can deconvolve the incoming signal with the autoconvolution of the transducer impulse response. This can improve the depth resolution.

Deconvolution or inverse filtering can also be used in the transversal direction. The calculations of the transient diffraction patterns in Chapter 4 and the measurements in Chapter 6 show that we have a good model of the wave propagation. This model can be used to design an inverse filter in the transversal direction.

The problem with using a deconvolver or an inverse filter is that the signal to noise ratio will be decreased. Our transducers are however quite efficient compared with many traditional echo imaging transducers. We had to design efficient transducers to meet the requirements for the doppler measurements. In the echo imaging mode this high efficiency gives us the possibility of using a more radical inverse filtering. More extensive studies are, however, required to find the proper design of the inverse filters.

8. CONCLUSIONS

The aim of this work has been to develop a model to analyse transient wave propagation from ultrasonic transducers and to design transducers which can be used both for echo imaging and doppler velocity measurements.

The model for the transient diffraction was based on the method with the spatial impulse response. The good agreement between the calculations and the measurements has proved the validity of this model. The computer programs are available for further analyses of diffraction patterns.

The transmission line model was used to model the transducer. This is a well known model and we found also that it worked well for the vibration mode it is meant to model. Other modes of vibration were however found to be important, especially for the annular array elements. This calls for an improved transducer model which takes all the modes into account.

The natural focusing effect from a piston has been analysed and rules of thumb to predict the location of the beam waist are found. More important is, however, that this natural focusing does not affect the optimum focusing of the transducer. Just as for gaussian beams we found that the optimum focal length for a certain depth is to choose the focal length equal to the depth.

Dynamic focusing with annular arrays has been analysed. The required number of elements for a planar piston of frequency 3 MHz and diameter 12.7 mm was found to be four elements. With a curved aperture in addition to the focusing of the elements this number could be reduced to two elements.

The transducers were designed with one quarter wave matching layer and a very light backing. This design gave us transducers with pulses shorter than 1 μs and power efficiency higher than 50%. The transducers are therefore well suited for both echo imaging and doppler velocity measurements.

A model of the echo response has been developed, based on a simple planar wave object model. The results showed that the depth resolution was 1 mm. Better object models should be developed to study the signature of more realistic objects.

The models for transient wave propagation developed in this work can be used to study and improve the imaging system. It gives the tool to design a signal processor that can improve the resolution in the image.

LIST OF REFERENCES

[1] P.R. Stepanishen, "Transient Radiation from Pistons in an Infinite Planar Baffle", JASA 49, 1627-1638, (1971).

[2] P.R. Stepanishen, "Wide Bandwidth Acoustic Near and Far Field Transients from Baffled Pistons", Proc. 1977 IEEE Ultrason. Symp., 113-118.

[3] P.R. Stepanishen, "Pulsed transmit/receive response of ultrasonic piezoelectric transducers", JASA 69, 1815-1827, (1981).

[4] R. Krimholtz, D. Leedom, G. Matthaei, "New Equivalent Circuits for Elementary Piezoelectric Transducers", Electronics Letters 6, 398-399, (1970).

[5] M. Fink, "Theoretical study of pulsed echographic focusing procedures", Proc. Acoust. Imag. 10, 437-453, (1980).

[6] M. Arditi, F.S. Foster, J.W. Hunt, "Transient fields of concave annular arrays", Ultrason. Imag. 3, 37-61, (1981).

[7] G.R. Harris, "Transient field of a baffled planar piston having an arbitrary vibration amplitude distribution", JASA 70, 186-204, (1981).

[8] G.R. Harris, "Review of transient field theory for a baffled planar piston", JASA 70, 10-20, (1981).

[9] J.W. Strutt (Lord Rayleigh), "Theory of Sound", Vol. 2, Dover, New York, 1945.

[10] M. Devlieger (ed.), "Handbook of clinical ultrasound", J. Wiley, New York, 1978.

[11] A.V. Oppenheim, R.W. Shafer, "Digital signal processing", Prentice-Hall, New Jersey, 1975.

[12] R. Kuc, "Generating a minimum-phase digital filter model for the acoustic attenuation of soft tissue", Proc. 1983 IEEE Ultrason. Symp., 794-796.

[13] I. Johansen, "Elektriske kretser" (Norw.), Tapir, Norway, 1978.

[14] P.M. Morse, K.U. Ingard, "Theoretical Acoustics", McGraw-Hill, USA, 1968.

[15] W.P. Mason, "Electromechanical Transducers and Wave Filters", 2nd ed., Van Nostrand, New York, 1948.

[16] M. Redwood, "Transient performance of a piezoelectric transducer", JASA 33, 527-536, (1961).

[17] M. Redwood, "A study of waveforms in the generation and detection of short ultrasonic pulses", Appl. Mater. Res. 2, 76-84, (1963).

[18] D. Leedom, R. Krimholtz, G. Matthaei, "Equivalent circuits for transducers having even- or odd-symmetry piezoelectric excitation", IEEE SU-18, 128-141, (1971).

[19] J.D. Frazer, "The design of efficient broadband ultrasonic transducers", Ginzton Lab. Report no. 2973, Stanford University, Stanford, CA, 1979.

[20] H. Jaffe, D.A. Berlincourt, "Piezoelectric transducer materials", IEEE Proceedings 53, 1372-1386, (1965).

[21] Ferroperm A.S., Product catalogue: "Piezoceramics", Vedbæk, Denmark, 1983.

[22] C. Desilets, J. Frazer, G.S. Kino, "The design of efficient broadband piezoelectric transducers", IEEE SU-25, 115-125, (1978).

[23] B. Angelsen, E. Bøen, "Optimization of layered multiport ultrasonic transducer structure", SINTEF Report no. STF48 F81004, Trondheim, Norway, 1981.

[24] C.S. Clay, H. Medwin, "Acoustical oceanography", J. Wiley, USA, 1977.

[25] D.R. Dietz, S.J. Norton, M. Linzer, "Wideband annular array response", Proc. 1978 IEEE Ultrason. Symp., 206-211.

[26] E. Hecht, A. Zajac, "Optics", Addison-Wesley, USA, 1979.

[27] J.D. Gaskill, "Linear systems, fourier transforms and optics", J. Wiley, USA, 1978.

[28] H. Engan, "An ultrasound power meter", JASA 72, 1121-1123, (1982).

[29] P.S. Green, G. J. Eilers, "The design of lenses for ultrasonic imaging", Stanford Research Institute, Stanford, USA.

[30] P. Alias. P. Challande, C. Kammoun, "A new technique for realizing annular arrays or complex shaped transducers", Proc. Acoust. Imag. 13, 1983.